Boron Nitride Growth and Electronics

A Dissertation
Presented to the Faculty of the Graduate School of
Cornell University
In Partial Fulfillment of the Requirements for the Degree of
Doctor of Philosophy

By Brian Rene Calderon
May 2018

Boron Nitride Growth and Electronics

Brian Rene Calderon, Ph.D.
Cornell University 2018

With the rise of 2D materials in the past decade there has been an increasing need for an appropriate insulator within the family in order to fabricate well behaved 2D based transistors. Hexagonal Boron Nitride (hBN) has fulfilled that need by providing a substrate free of dangling bonds, low levels of corrugation and excellent thermal and chemical stability. However, hBN itself is quite an intriguing material and has been somewhat neglected within the 2D family. Its wide bandgap allows for DUV emission in the UVC range which is critical for water sanitation and biological and chemical process'. It has also been shown to host photoactive defects which can emit single photons paving the way for the creation of solid state single photon emitters, something that has proven impossible until now. Due to these reasons it's imperative that fundamental research into hBN's synthesis as well as its electronic and optical properties be conducted.

With regards to the growth of hBN our main focus is on the popular CVD method, however, recently other methods are also underway (MBE, LPE, etc…). In this regard, hBN growth has lagged Graphene (Gr) where millimeter (mm) sized single crystals have already been demonstrated. We show that this feat can also be accomplished in hBN through a variety of optimization schemes where single crystals up to 0.3mm where synthesized. We also focus on the proposed growth mechanisms and difficulties of growing thick layered hBN via CVD.

With regards to its electronic properties we report the demonstration of high mobility devices where our CVD grown hBN was used as the conductive channel. This is unprecedented in the scheme of 2D's since hBN has been widely regarded to be insulating. We explore the possible doping mechanisms in our grown films and also give possible reasons why our material is

conductive while the exfoliated films used by the majority of researchers in the field are not.

Finally, we note that our work is only the beginning of what may be an incredibly exciting field of transport in wide band-gap 2D materials since 2D GaN has also recently synthesized which possesses a bandgap similar to hBN. We are also only the first of very few reports of large single crystal hBN films and hope that this will open the doors to studying the high-quality growth of hBN monolayers and multilayers similar to what happened with Gr. The field of 2D materials would greatly benefit from the wide availability of high quality large single crystal hBN, since this would avoid grain boundaries and other defects in hBN that would degrade its use as a substrate.

BIOGRAPHICAL SKETCH

Brian was born in Bronx, NY and raised in southern Ecuador in a small town south of the city of Cuenca called “Gualaceo”. After completing high school in Gualaceo he spent one year studying computer science in the State University of Cuenca before moving to continue his studies in the U.S. He received his Associates in Science degree from Bronx Community College and then went on to finish his Bachelors in Electrical Eng. from Rensselaer Polytechnic Institute. He did a one-year Masters in Engineering program at Cornell University and then went on to pursue his PhD. in Electrical Eng. at the same institution. His work during his graduate studies has mainly focused on the synthesis and properties of 2D materials. Brian will join the Materials Science division of the Naval Research Labs (NRL) in Washington, DC after graduation.

To my Family and Friends

To Clarissa I. Calderon
may my high be your low,
may my goals be your starting point
and may your dreams never be less than unimaginable

ACKNOWLEDGMENTS

First and foremost, I would like to acknowledge Dr. Spencer for giving me the opportunity to study under him at Cornell. Although our lab faced several economic difficulties, each one of them pushed us to be more competent researchers and to step aside from being “pencil and paper” researchers and get our hands dirty. Dr. Spencer’ immense knowledge and experience was invaluable over the years, especially when tackling new problems, such as conduction in hBN, which he could always relate to a similar problem that has already been solved. To this day I have no idea how he can recall so many facts with such clarity. When performing our CVD growths Dr. Spencer’ unique input and imaginative ideas always pushed us in new directions that were the most interesting in the field. The quality of researcher I am today is due to Prof. Spencer’ training and his teachings will accompany me throughout my career. I’ll always be proud to be called “a Spencer”.

My parents and my sister have been my beacon of light that helped me stay on course and finish this journey. Both economically and emotionally my family was always there for me and none of this would’ve been possible without their support. Special thanks to my uncle Luis Centeno who was always willing to be an open ear to my many downfalls and frustrations over the years. To my friends from my youth, Fernando Cuesta, Daniel Ulloa, Carlos Saquicela, Jeff Calle and David Serrano, I thank you for being loyal over the years and always reminding of my roots when I visited Ecuador.

There are likely too many researchers and colleagues to list easily in these few pages, however I would like to specially thank Dr. Debdeep Jena for agreeing to be my special advisor during my last year. I was pushed under him more than I ever was and came out a better researcher

because of it. Dr. Farhan Rana was always an invaluable asset to have as a committee member. Aside from being just shear brilliant, his expertise in many fields was always a welcome blanket of support when it came to hard questions. Finally, I would like to thank Dr. Paul McEuen for not only being the nicest researcher/famous scientist I've ever met, but for taking the time to listen to me when I was going through some turmoil and also for autographing my copy of his novel "Spiral".

To Prof. Gregory Fuchs and his student and good friend of mine Nicholas Jungwirth (Nick) I thank you for the collaboration in studying single photon emitters in hBN. I owe a special debt of gratitude to Nick who was my friend far before he was my collaborator, if not for that one night of too many whiskey's (and perhaps a bit of moonshine) when we started talking about our graduate work, the project on single photon emission in hBN would never have started.

All the members of the Jena/Xing groups have been of support in one way or another, they welcomed me into the group and were never reluctant to share their insights. I would especially like to thank Dr. Valdimir Protasenko for being by far one of the best experimentalists I've ever worked with. I'll always remember his willingness to stay after hours even on a Friday evening, as well as his incredibly humble attitude when it came to getting an experiment to work:

-(Brian) Holly sh&^* you did it Vlad!

-(Vlad) Of course I did…

-(Brian) Your amazing!

-(Vlad) Thank you, I know.

To my colleagues in the Spencer group, I want to say thank you for helping me survive my initial years in graduate school and for being pleasant office mates. Jeonghyun (Jeff) Hwang was an amazing guide and I owe a great deal of gratitude for his mentorship in my initial years, I would

not have survived my initial years if not for him. Yanxin, who took over the hBN growth in the final years, was the most enthusiastic hard-working student I've ever met. I know I will hear great things from him in the years to come and I hope to one-day work with Dr. Xi. Finally, I would like to acknowledge a member of our group who will be greatly missed, Dong Quan Hao, who passed away during my 2nd year as a graduate student. Dong was my TA when I took Prof. Spencer' Nanofabrication course, he was also one of the most pleasant individuals to talk to and was incredibly smart from what I recall. The world is a lesser place without him.

Table of Contents

Table of Figures

I. Introduction

1 Boron Nitride's Role in the 2D Family

2D materials have seen a great deal of intense research since their prospects in electronics were discovered in 2004 [1]. Prior to this it was believed that atomically thin layers of materials were unstable at room temperature [2], however there was great motivation to try to isolate them and make functional devices with these films since extending the field effect to these materials could take advantage of their predicted enhanced electrical properties as compared to bulk semiconductors [3, 4]. Since this was achieved an ever expanding family of layered materials have been discovered including semiconducting dichalcogenides [5], metal organic frameworks [6] as well as the well know semimetal Graphene (Gr) and the only wide band gap semiconductor in the family hexagonal Boron Nitride (hBN) [7]. Figure 1 shows a small subset of the relevant 2D materials and their bandgaps as of this writing.

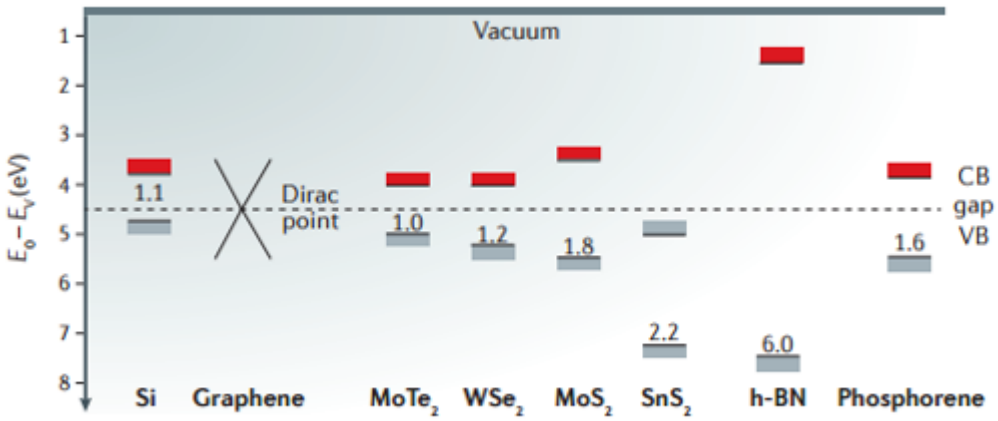

Figure 1 : Bandgaps of common 2D materials (Taken from [8])

Within this family hBN's insulating nature has led it be mainly used as a substrate or encapsulation layer for other 2D materials [9, 10, 11]. It has been proven to be an exceptional

substrate for Gr electronics due to its lack of dangling bonds and charge impurities which prevent unintentional doping [12], its close lattice match to Gr (~1.7% mismatch [13]) reduces thermal stress and its high energy surface optical phonons lead to reduced carrier scattering and better performing devices [14, 15, 16, 17, 18]. hBN has also recently been used as a substrate for growing vertical 2d heterostructures [19, 20, 21, 22] where in some cases it's been shown to be a better growth substrate by yielding less lattice strain, lower doping levels and cleaner interfaces. Lastly hBN was initially also proven to be a valuable release layer for the mechanical transfer of grown stacks of 3D devices [23]. Within all these applications hBN has played somewhat of a secondary role in 2D electronics however it has many interesting properties of its own many of which have only recently been studied.

2 Properties and Unique Aspects of Hexagonal Boron Nitride

hBN has recently proven to be a 2D material with unique properties not offered by other members in this family. Before we get into the unique electrical and opticalr aspects that hBN offers we should understand the crystalline nature of this material.

The crystal structure of hBN is of a layered nature with strong sp2 covalent bonds within the lattice and weak van der-Waals bonds between adjacent planes. Its unit cell is hexagonal with a bond length of 1.44 Å as shown in Fig. 2. Amongst the possible stacking sequences of hBN it has been theorized that three are the stable, these are: AA' where the top layer is perfectly aligned with the bottom layer and the Boron atoms sit on top of a Nitrogen atom as shown in Fig. 3a ; AB1 where the Boron atoms of the top layer sit on top of the Boron atoms of the bottom layer and the Nitrogen atoms of the top layer sit in the center of the bottom layers hexagon as shown in Fig. 3b ; AB2 which is the same as AB1 only with the positions of the Boron and Nitrogen atoms switched as shown in Fig. 3c [24]. For CVD grown hBN only the

AA' stacking sequence has been observed [25]. This is mainly due to the fact that the AB2 mode is less energetically favorable than the AA' mode having an energy ~64meV/atom higher, however the AB1 mode has practically the same energy per atom as the AA' mode (38.1meV/atom) and has not been reported. Furthermore, the stacking of hBN has been found to be governed by the electrostatic interactions between layers and the vdW interactions only determine the interlayer distance but don't play a role in the stacking. The stability of the AB1 mode is important since it's been found that when bilayer hBN is shifted from AA' to AB1 a decrease in the bandgap of 0.6eV occurs. This makes hBN's electrical properties strongly dependent on its mechanical properties. The strong electromechanical properties of hBN were first reported in 2009 by Naumov et al. [26] where they found that corrugated monolayers become strongly polarized producing what's called a "giant flexoelectric effect".

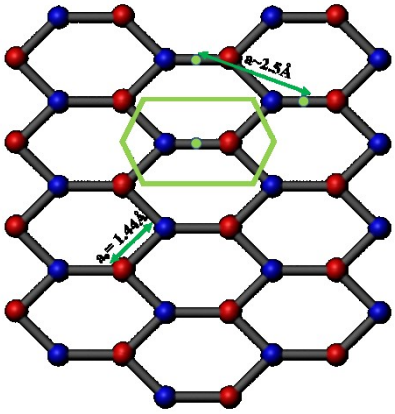

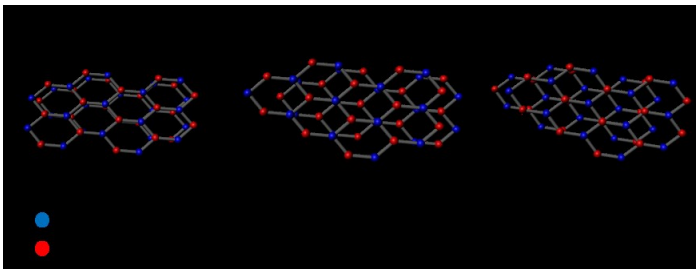

Figure 2 :hBN atomic plane (top view)
showing the lattice parameter "a" and spaing between atoms "a_o" as well as the WZ unit cell (green outlined hexagon).

Figure 3 : Stacking sequences for hBN planes: (a) AA' (b) AB1 (c) AB2

Owing to the strong in plane bonding between the Boron and Nitrogen atoms hBN's wide bandgap (~6eV [7]) has proven to host photostable defect centers which emit single photons at

room temperature [27, 28], this discovery has made 2D materials strong players in the fields of quantum information and nanophotonics paving the way for the development of solid state non-classical light sources [29]. hBN's lack of dangling bonds and strong in plane bonding has also made it suitable as an oxidation resistant coating [30] where it's been shown that monolayers survive in air up to 840°C [31]. Furthermore, monolayer hBN has been predicted to have one of the largest in plane thermal conductivities of the 2D family (~$600 W m^{-1} k^{-1}$) due to a suppression of phonon-phonon scattering in the single layer form as compared to bulk [32]. This makes hBN a prime candidate as a thermal heat spreader in 2D nanoelectronics [25, 33, 34]. It should be noted that the out of plane thermal conductivity of hBN is ~3 orders of magnitude lower than the predicted in plane [32], making it a poor out of plane thermal conductor which is the case with any 2D structure due to the lack of bonding in this direction [34]. In fact, hBN has been shown to be outperformed by SiO_2 itself when it comes to out of plane thermal conductance [35, 36], thus in order to take advantage of hBN's thermal properties patchwork "stitched" 2D heterojunctions must be made. A possible solution to the out of plane thermal conductance in 2D's has been proposed by a futuristic design involving BNNT's vertically aligned on an hBN sheet, with this structure the out of plane thermal conductivity has been shown to increase by 1 order of magnitude [37]. Due to its ~6eV bandgap hBN also has tremendous potential on the field of solid state DUV emission where initial studies have proven it to be a great contender [38, 39]. Unlike its partner III-nitrides GaN and AlN, hBN is unique in that it has an extraordinarily large exciton binding energy (~0.7eV [40]) which is an order of magnitude larger than AlN and GaN [41]. This large exciton energy is due both its 2D layered structure which confines excitons strongly in plane as well as the large electron negativity difference between its constituent atoms. Due to these reasons hBN's luminescence in the DUV range is much stronger allowing for high intensity sources that can

replace today's solid-state excimer lasers or mercury lamps [42]. A major problem in using AlN based DUV sources is that p-type conductivity is hindered in AlN effectively reducing the quantum efficiency (Q.E.) of these devices. Recent results have shown that hBN has a propensity to be p-type doped and its p-type resistivity is significantly lower than AlN [43]. One aspect of this thesis reviews our results in p-type conduction in monolayer hBN where we demonstrate that indeed p-type conduction is significantly enhanced in this layered structure.

References

[1] K. S. Novoselov, A. K. Geim, S. V. Morozov, D. Jiang, Y. Zhang, S. V. Dubonos, I. V. Grigorieva and A. A. Firsov, "Electric field effect in atomically thin carbon films," *Science,* vol. 306, p. 22, 2004.

[2] M. S. Dresselhaus and G. Dresselhaus, "Intercalation compounds of graphite," *Advances in Physics,* vol. 51, p. 1, 2002.

[3] S. V. Rotkin and K. Hess, "Possibility of a metallic field effect transistor," *Applied Physics Letters,* vol. 84, p. 3139, 2004.

[4] P. R. Wallace, "The band theory of graphite," *Physical Review Letters,* vol. 71, p. 622, 1946.

[5] Z. Lin, A. McCreary, N. Briggs, S. Subramanian, K. Zhang, S. Yifan, X. Li, N. J. Borys, H. Yuan, S. K. Fullerton-Shirley, A. Chernikov, H. Zhao, S. McDonnell, A. M. Lindenberg, K. Xiao, B. J. LeRoy, M. Drndic, J. C. Hwang, J. Park, M. Chhowalla, R. Schaak, a. Javey, M. C. Hersam, J. Robinson and M. Terrones, "2D materials advances," *2D materials,* vol. 3, p. 042001, 2016.

[6] D. Sheberla, L. Sun, M. A. Blood-Forsythe, S. Er, C. R. Wade, C. K. Brozek, A. Aspuru-Guzik and M. Dinca, "High electrical conductivity in Ni3 (2,3,6,7,10,11 - heximinotriphenylene)2 a semiconducting metal organic graphene analogue," *JACS,* vol. 136, p. 8859, 2014.

[7] G. Cassabois, P. Valvin and B. Gil, "Hexagonal boron nitride is an indirect bandgap semiconductor," *Nature Physics,* vol. 10, p. 262, 2015.

[8] M. Chhowalla, D. Jena and H. Zhang, "Two-dimensional semiconductors for transistors," *Nature Reviews,* vol. 1, p. 1, 2016.

[9] C. R. Dean, A. F. Young, I. Meric, C. Lee, L. Wang, S. Sorgenfrei, K. Watanabe, T. Taniguchi, P. Kim, K. L. Shepard and J. Hone, "Boron nitride substrates for high quality graphene electronics," *Nature Nanotechnology,* vol. 5, p. 722, 2010.

[10] A. S. Mayorov, R. V. Gorbachev, S. V. Morozov, L. Britnell, R. Jalil, L. A. Ponomarenko, P. Blake, K. S. Novoselov, K. Watanabe, T. Taniguchi and A. K. Geim, "Micrometer scale ballistic transport in encapsulated graphene at room temperature," *Nanoletters,* vol. 11, p. 2396, 2011.

[11] L. Wang, I. Meric, P. Y. Huang, Q. Gao, Y. Gao, H. Tran, T. Taniguchi, K. Watanabe, L. M. Campos, D. A. Muller, J. Guo, J. Hone, K. L. Shepard and C. R. Dean, "One dimensional electrical contact to a two dimensional material," *Science,* vol. 342, p. 614, 2013.

[12] J. Martin, N. Akerman, G. Ulbricht, T. Lohmann, J. H. Smet, K. von Klitzing and A. Yacoby, "Observation of electron hole puddles in graphene using a scanning single electron transistor," *Nature Physics,* vol. 4, p. 144, 2007.

[13] G. Giovannetti, P. A. Khomyakov, G. Brocks, P. J. Kelly and J. van den Brink, "Substrate induced band gap in graphene on hexagonal boron nitride," *Physical Review B,* vol. 76, p. 073103, 2007.

[14] I. Meric, M. Y. Han, A. F. Young, B. Ozyilmaz, P. Kim and K. Shepard, "Current saturatino in zero bandgap top gated graphene field effect transistors," *Nature Nanotechnology,* vol. 3, p. 654, 2008.

[15] F. Schwierz, "Graphene transistors," *Nature Nanotechnology,* vol. 5, p. 487, 2010.

[16] A. C. Ferrari, S. Reich, A. Loiseau, R. Arenal, I. Bello and J. Robertson, "Resonant raman scaterring in cubic and hexagnoal boron nitride," *Physical Review B,* vol. 71, p. 205201, 2005.

[17] L. Li, G. J. Ye, V. Tran, R. Fei, G. Chen, H. Wang, J. Wang, K. Watanabe, T. Taniguchi, L. Yang, X. H. Chen and Y. Zhang, "Quantum oscillations in a two dimensional electron gas in black phosphorus thin films," *Nature Nanotechnology,* vol. 10, p. 608, 2015.

[18] J. Wang, Q. Yao, C.-W. Huang, X. Zou, L. Liao, S. Chen, Z. Fan, K. Zhang, W. Wu, X. Xiao, C. Jiang and W.-w. Wu, "High moblity MoS2 transistor with low schottky barrier contact by using atomic thick hBN as a tunneling barrier," *Advance Materials,* vol. 28, p. 8302, 2016.

[19] S. Wang, X. Wang and J. H. Warner, "All chemical vapor deposition growth of MoS2:hBN vertical van der Waals heterostructures," *Nanoletters,* vol. 9, p. 5246, 2015.

[20] M. Wang, S. K. Jang, W.-J. Jang, M. Kim, S.-Y. Park, S.-W. Kim, S.-J. Kahng, J.-Y. Choi, R. S. Ruoff, Y. J. Song and S. Lee, "CVD growth of single layer graphene on CVD grown hexagonal boron nitride," *Advanced Materials,* vol. 25, p. 2746, 2013.

[21] Q. Zhang, Y. Chen, C. Zhang, C.-R. Pan, M.-Y. Chou, C. Zeng and C.-K. Shih, "Bandgap renormalization and work function tuning in MoSe2/hBN/Ru(0001) heterostructures," *Nature Communications ,* vol. 7, p. 13843, 2016.

[22] S. Behura, P. Nguyen, S. Che, R. Debbarma and V. Berry, "Large are transfer free oxide assisted synthesis of hexagonal boron nitride films and their heterostructures with MoS2 and WS2," *JACS,* vol. 137, p. 13060, 2015.

[23] Y. Kobayashi, K. Kumakura, T. Akasaka and T. Makimoto, "Layered boron nitride as a realease layer for mechanical transfer of GaN based devices," *Nature,* vol. 484, p. 223, 2012.

[24] N. Marom and a. et, "Stacking and registry effects in layered materials: the case of hexagonal boron nitride," *Physical Review Letters,* vol. 105, p. 046801, 2010.

[25] J. Yin, J. Li, Y. Hang, J. Yu, G. Tai, X. Li, Z. Zhang and W. Guo, "Boron nitride nanostructures: fabrication, functionalization and applications," *Small,* vol. 12, p. 2942, 2016.

[26] I. Naumov and a. et, "Unusual flexoelectric effect in two-dimensional noncentrosymmetric sp2-bonded crystals," *Physical review letterse,* vol. 102, p. 217601, 2009.

[27] N. R. Jungwirth, B. Calderon, Y. Ji, M. G. Spencer and M. E. Flatte, "Temperature dependance of wavelength selectable zero phonon emission from single defects in hexagonal boron nitride," *Nanoletters,* vol. 10, p. 16, 2016.

[28] T. T. Tran, K. Bray, M. J. Ford, M. Toth and I. Aharonovich, "Quantum emission from hexagonal boron nitride monolayers," *Nature Nanotechnology,* vol. 11, p. 37, 2015.

[29] I. Aharonovich, D. Englund and M. Toth, "Solid state single photon emitters," *Nature Photonics Reviews,* vol. 10, p. 631, 2016.

[30] Z. Liu, Y. Gong, W. Zhou, L. Ma, J. Yu, J. C. Idrobo, J. Jung, A. H. MacDonald, R. Vajtai, J. Lou and P. M. Ajayan, "Ultrathin high temperature oxidation resistant coatings of hexagonal boron nitride," *Nature Communications,* vol. 4, p. 2541, 2013.

[31] L. H. Li, J. Cervenka, K. Watanabe, T. Taniguchi and Y. Chen, "Strong oxidation resistance of atomically thin boron nitride nanosheets," *ACS Nano,* vol. 8, p. 1457, 2014.

[32] L. Lindsay and D. A. Broido, "Enhanced thermal conductivity and isotope effect in single layer hexagonal boron nitride," *Physical Review B,* vol. 84, p. 155421, 2011.

[33] H. Wang, Y. Zhao, Y. Xie, X. Ma and X. Zhang, "Recent progress in synthesis of two dimensional hexagonal boron nitride," *Journal of semiconductors,* vol. 38, pp. 031003-1, 2016.

[34] G. Bhimanapati, Z. Lin, V. Meunier, Y. Jung and a. et, "Recent advances in two dimensional materials beyond graphene," *ACS Nano,* vol. 9, p. 11509, 2016.

[35] C.-C. Chen, Z. Li, L. Shi and S. B. Cronin, "Thermal interface conuctance across a graphene/hexagonal boron nitride heterojunction," *Applied physics letters,* vol. 104, p. 081908, 2014.

[36] M. T. Alam, M. S. Bresnehan, J. A. Robinson and M. A. Haque, "Thermal conductivity of ultra thin chemical vapor deposited hexagonal boron nitride," *Applied physics letters,* vol. 104, p. 013113, 2014.

[37] N. Sakhavan and R. Shahsavari, "Dimensional crossover of thermal transport in hybrid boron nitride nanostructures," *ACS Applied Materials and Interfaces,* vol. 7, p. 18312, 2015.

[38] K. Wantanabe, T. Taniguchi and H. Kanda, "Direct bandgap properties and evidence for ultraviolet lasing of hexagonal boron nitride single crystal," *Nature Materials,* vol. 3, p. 404, 2004.

[39] Y. Kubota, K. Wantanabe, O. Tsuda and T. Taniguchi, "Deep ultraviolet ligh emitting hexagonal boron nitride synthesized at atmospheric pressure," *Science,* vol. 317, p. 932, 2007.

[40] B. Arnaud, S. Lebegue, P. Rabiller and M. Alouani, "Huge excitonic effects in layered hexagonal boron nitride," *Physical Review Lettersq,* vol. 96, p. 026402, 2006.

[41] L. Bornstein, "AlN excitonic energy gaps, excitonic binding energies and lifetime," in *Semiconductors Vol. 44*, New Jersey, Springer, 2008.

[42] S. Nakamura, "Current status of GaN based solid state lighting," *MRS bulletin,* vol. 34, p. 101, 2009.

[43] D. A. Laleyan and et al, "AlN/hBN heterostructure for Mg dopant free ultraviolet photonics," *ACS Nanoletters,* vol. 17, p. 3738, 2017.

II. CVD Growth of Hexagonal Boron Nitride

1 Historical Background

H-BN was first reported to have been synthesized by Balmain [1] in 1842 through a chemical reaction between boric oxide and potassium cyanide. It wasn't until two major discoveries that the CVD synthesis of hBN was possible. The first of which came in ~1852 where by Bunsen (yep, the same guy that the burner is named after) reported for the first time a method of synthesis of iron oxide crystals from hot volcanic gases containing hydrochloric acid (HCl) [2]. This crystal formation was the result of the following chemical reaction:

$$2FeCl_3(g) + 3H_2O(g) \leftrightarrow Fe_2O_3(s) + 6HCl(g) \quad (1)$$

This chemical reaction was taken to be the first ever synthesis by Chemical Vapor Deposition (CVD) and since then the field has seen exponential increase. Over a century later the first CVD grown hBN samples were prepared by Nakamura using the solid metal organic precursor Triethylboron (TEB) and ammonia [3]. This technique of using a metal organic source in CVD is quite different from other CVD methods and today forms a subfield of its own coined MO-CVD. We note that the topic of the first reported synthesis of CVD hBN is a bit of a debated one, thus, our choice of the first report is due to the fact that prior reports failed to solve the problem of contaminants and routinely obtained either amorphous or nanocrystalline films. Nakamura was also the first to report a "colorless transparent film" which was expected for boron nitride since it absorbs less than 98% of visible light [4].

A subsequent necessary discovery for hBN synthesis was its solid source precursor (other precursors are also possible, but we focus on the solid source in this thesis) Ammonia-Borane (AB). AB was first synthesized in 1955 by Parry and Shore at the University of Michigan [5]. They were able to synthesize the material from both Lithium Borohydride ($LiBH_4$) and Diammoniate

of Diborane ($[H_2B(NH_3)_2^+][BH_4^-]$) by adding Diethyl ether to catalyze the reaction of these with NH_4Cl. The discovery of the compound was further strengthened by X-ray diffraction analysis which verified that the resulting white powder had a crystalline form corresponding to Ammonia Borane. The CVD of hBN using AB as a solid precursor was first reported in 2010 by Song et al. [6].

Since the first synthesis of hBN via CVD many CVD based methods have been reported which mainly differ with regards to the precursor type. We will briefly describe these methods in the following sections. It's also worth noting that there have been several recent reports of Molecular Beam Epitaxy (MBE) grown hBN films [7, 8, 9], this technique is the ultimate goal for layered materials (and materials growth in general) due to the precise control of many different properties in the growing films. Another advantage of MBE is the negligible gas phase reactions which readily occur in CVD and can lead to unwanted secondary deposits. However, since most MBE growth efforts are at the moment mainly academic and require orders of magnitude larger investments than CVD growth, this thesis focuses on the CVD technique.

Finally, a motivation to the need of CVD has to be made in order to establish its broader role in electronics and technology. As we will describe in a latter section, the only sure way of obtaining single crystal hBN has been by exfoliating large bulk crystallites made under High Temperature High Pressure (HPHT) reactions [10, 11]. These bulk crystallites are however limited in size to a few hundred um's and the exfoliation method has no control over thickness. Furthermore, due to hBN's stronger adhesion between planes as compared to other 2D's [12] its more difficult to exfoliate monolayers of this material. CVD overcomes all of these disadvantages by offering layer control, crystal sizes that are only limited by the equipment and even morphology control [13]. The only downfall of CVD is that even for 2D structures which exhibit weak epitaxy with the

catalyst, the orientations of the nuclei are still dictated by the underlying crystal used in the growth. This means that various orientations will be present which ultimately lead to grain boundaries and smaller single crystal regions as compared to HPHT. It is the goal of this thesis to show that these defects can be overcome and CVD hBN can exhibit single crystal regions comparable to those of HPHT bulk crystallites.

2 Growth Techniques for hBN

As mentioned in the prior section we will restrict our discussion to CVD based techniques for growing hBN, one exception Is made for the section on High Temperature High Pressure (HTHP) based techniques which are essential for the creation of single crystal bulk hBN. The survey of CVD techniques will be majorly divided into three categories based on the choice of precursor, these are: Solid CVD, Gaseous CVD and Liquid CVD. Within these categories subdivisions will be made based on the pressure regime whether it was Low Pressure CVD (LPCVD) or Atmospheric Pressure CVD (APCVD).

2.1 Solid CVD

Using solid precursors in CVD is not uncommon and as mentioned before MOCVD is an entire subfield that treats this process. Two separate solid precursors for hBN synthesis have been used recently, these are Decaborane and Ammonia Borane (AB). The latter being the more widely used option. In the following section we sill briefly discuss the usage of Decaborane and the results people have achieved with it as well as its pros and cons. AB will be treated afterwards and quite extensively since it is the precursor of choice for this work.

2.1.1 Decaborane Precursor

Decaborane is a solid precursor with limitations similar to those for TEB, thus only

Decaborane will be discussed with the understanding that TEB suffers from similar limitations. In the case of Decaborane it is necessary to flow a Nitrogen containing gas (typically NH_3) since this material only serves as a Boron source. Due to this setback the stoichiometric control of the resulting films is quite difficult, and few results have been published using the Decaborane source [14, 15]. Decaborane can also spontaneously combust in air and thus has to be handled with care. Decaborane's advantages come with regards to its easily regulated vapor pressure up to 90°C during thermolysis as well as its sublimation without decomposition or additional reactants unlike AB. Despite these advantages the difficulties in reproducibly getting stoichiometric hBN at the pressure ranges of CVD (~mtorr- torr) and the hazards it promotes have led Decaborane to be only seldom used. The layer control of hBN using this precursor has not been reported and it has mostly been employed using APCVD.

2.1.2 Ammonia Borane Precursor

Ammonia-Borane on the other hand been widely used as the precursor for hBN CVD, it's also the precursor of choice for this work so it deserved its own separate section. The first monolayer hBN films using AB were prepared by Lee eta al. [16]. AB is commonly prepared as a white crystalline powder and is stable in air at room temperature and normal atmospheric conditions. AB's advantages are mainly due to its room temperature stability in comparison to the most popular liquid precursor Borazine, which makes it easy to handle. Its stoichiometric decomposition into the gas phase is another nice property that makes AB a better choice than most other precursors (with the only exception of Borazine which is also stoichiometric). Since its synthesis in 1955 by Shore and colleagues AB has attracted the attention of chemists due its high hydrogen storage content (~19.6 wt% [17]) which make it attractive for Hydrogen fuel cell applications.

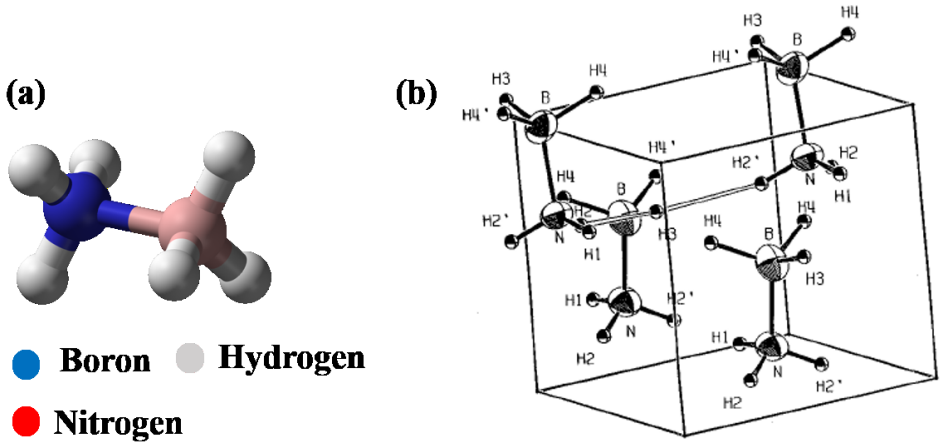

Figure 4 : (a) 3D depiction of the H3BNH3 monomer unit which composes the crystal Ammonia-Borane. (b) Unit cell of the crystal Ammonia-Borane taken from Fig. 3 of Ref. [18].

This property has made it a topic of rigorous study in the chemistry world which is fortunate for materials scientist's working on using the compound for hBN growth since there is a vast library of studies available on the compound. Its structure is composed of a monomer with chemical formula H_3BNH_3 which is depicted in Figure 4a. The crystal itself is very interesting since the monomers are held together through weak bonding of the Hydrogen terminations, this was a new type of intramolecular bond and was rigorously studied in the ~80's, today its known as the di-hydrogen bond [18]. A unit cell for the crystal is depicted in Fig. 4b.

An important aspect of AB for its usage in CVD is its stability at room temperature. It has been reported that at room temperature AB slowly decomposes into an insoluble polymeric compound called Poly Amino-Borane (PAB) which has distinctly different properties than AB [19]. This decomposition is caused by the slow release of H_2 at room temperature. It should be noted that the decomposition is very slow and varies depending on the methods that were used to prepare AB as well as on the humidity its exposed to [17], thus, it may take several days or even weeks to completely decomposed a 1mg of AB.

The decomposition of AB is in itself very interesting since the route to the PAB form consists of initially forming the salt Diammoniate of Di-Borane (DAB) [5]. This salt has been shown to

release a considerably larger gas phase content (i.e. partial pressure) of Borazine which is the key stoichiometric molecule necessary for the formation of hBN in CVD. Alternate ways of obtaining stable DAB have been proposed by forming a solution of AB in tetraglyme with leads to a liquid form of DAB [20]. Using this DAB compound as a precursor for hBN has not been reported and may be an interesting way of controlling the growth with greater precision. One of the weakness' in the usage of AB is that its partial pressure during sublimation is exceedingly small making the gaseous products different to control using a conventional Mass Flow Controller (MFC), liquid DAB may be able to overcome this problem. Regardless of the kinetics of the decomposition it is always recommended to store AB at low temperatures in a low humidity and inert atmosphere if possible.

Of upmost importance to the usage of AB as a precursor is its thermal decomposition upon heating, a process typically called Thermolysis. The thermolysis of AB is quite complicated and numerous studies have been published on this topic. It has been generally accepted that upon heating AB releases Diborane (Fig. 5a), H_2 (Fig. 5b), Monomeric Amino-Borane (Fig. 5c) and Borazine (Fig. 5d).

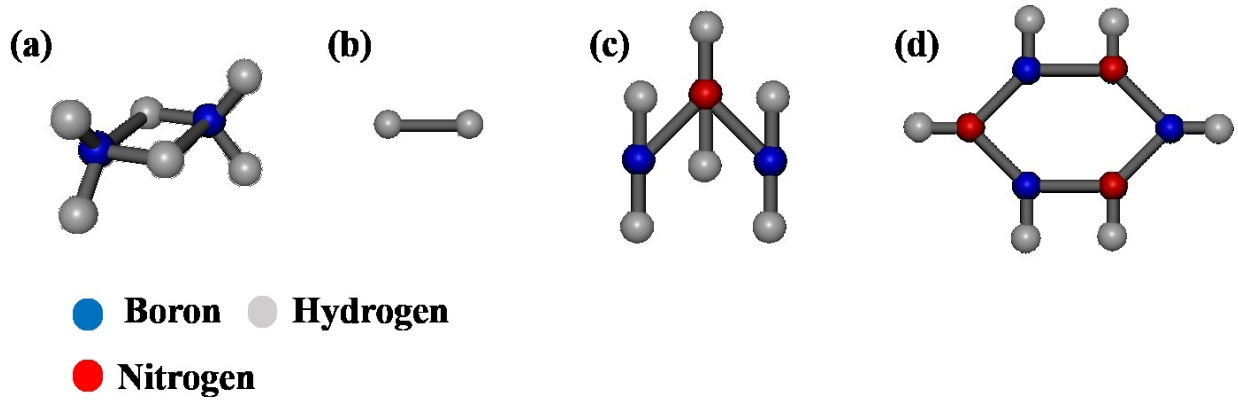

Figure 5: (a) 3D structure of DiBorane molecule. (b) 3D structure of H_2 molecule. (c) 3D structure of monomeric Amino-Borane (MAB). (d) 3D structure of Borazine molecule.

Of the various gaseous compounds released it is the Borazine molecule which is of greatest interest to the growth of hBN since its believed that the decomposition of this molecule is what ultimately leads to an hBN film on a catalytic surface. We can observe that, with the exception of DiBorane, all the gaseous products released have a 1:1 stoichiometry with respect to N:B which is why this precursor is very attractive for hBN growth. Much of the work on the thermal decomposition was done by Baitolow, Wolf and Baumman where rigorous studies using a variety of methods including Thermogravimetric analysis (TG), Differential Scanning Calorimetry (DSC) and Mass spectroscopy (MS) revealed the intricate nature of the thermolysis of AB [21]. Fig. 6a below shows (taken from Ref. [21]) shows the results of a DSC study on 20mg of AB. An initial high ramp rate (>1°C/min) was applied to the AB until 90°C was reached, the temp was heald steady at this value for 10hrs before a final heating ramp at 0.1°C/min was applied up to the final temperature of ~227°C. An initial exothermal reaction (labeled I) can be observed shortly after reaching 90°C, this exotherm is due to the melting of the AB. At this temperature it was reported to take a total of ~3hrs for the AB to completely melt and convert into its polymeric form PAB. We note that melting point of AB as well the melting process is quite complicated and has only recently been understood. Although the melting point of AB is typically cited ~100°C studies have confirmed that the melting process initiates even at room temperature [21, 22]. Essentially the melting process can be understood as a slow phase transformation process whereby the parent crystal phase AB slowly turns into a polymer PAB via dehydrogenation. As temperature increases, the dehydrogenation also increases and the transition to a PAB is quicker. Since the polymeric phase involves the crosslinking of long molecular chains it is not possible to reverse this process once initiated, however it can be stopped if the temperature is quenched below 25°C. A model that can be used to understand this process is based on the appearance of several PAB “nucleation”

sites within the surface and bulk of the AB. These sites will slowly crosslink with the dehydrogenated AB surrounding them until the entire crystal is transformed into PAB. Because of this "melting" it is desirable to keep the sublimation temperatures of AB below 90°C in order to increase the lifetime and usage of the AB. Fig. 6b shows the results of a mass spectroscopy analysis on AB at various temperatures. The takeaway from this figure is that borazine is never a large contribution to the measured gaseous products but rather its MAB and H_2 which dominate. It is also observed that the partial pressure of MAB and Borazine increase with increasing temperature leading to more reactive species that can produce hBN. This is in accordance with various growth experiments where they found that the thickness of hBN increases with the temperature of the precursor [23]. Lastly, at the melting point (labeled I in Fig. 6B) a rigorous release of H_2 is observed which is due to the dehydrogenation/polymerization process described earlier.

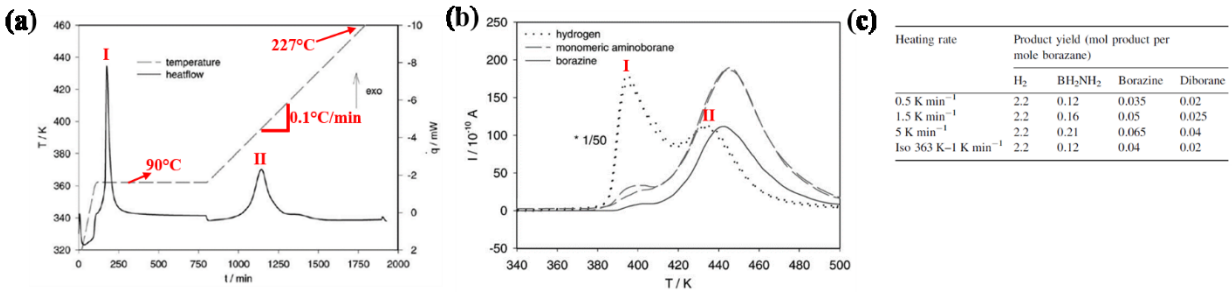

Heating rate	Product yield (mol product per mole borazane)			
	H_2	BH_2NH_2	Borazine	Diborane
0.5 K min^{-1}	2.2	0.12	0.035	0.02
1.5 K min^{-1}	2.2	0.16	0.05	0.025
5 K min^{-1}	2.2	0.21	0.065	0.04
Iso 363 K–1 K min^{-1}	2.2	0.12	0.04	0.02

Figure 6 : (a) DSC study on 20mg of AB taken from ref. [21]. (b) Mass spectroscopy study at various temperature of AB gaseous products taken from ref. [21]. (c) Gaseous product yield as a function of heat rate taken from [21].

Regardless of the temperature setting it can be seen that borazine is not a main component of the gaseous species prior to the melting point (labeled I in Fig. 6b). Since most efforts of CVD hBN growth have used temperatures below the melting point a valid question is therefore: "How can one obtain hBN without Borazine?". It appears that this specific question has not been

answered in the context of growth of hBN yet, however it is very likely that the main molecule responsible for growth is not Borazine but rather MAB. This is troubling since MAB is a lighter and more unstable molecule than borazine at the growth temperatures of ~1000°C used in hBN growth. Baitalow himself had shown that MAB dehydrogenates to a Mono Imino-Borane (MIB) at temperature below 100°C [19]. This MIB can then undergo varies reactions and form many compounds at high temperatures including Borazine, MAB and PAB amongst others. This means that gas phase reactions are much more easily produced with the presence of MAB and MIB within the system. For this reason, it is desirable to obtain a precursor that only decomposes into gaseous Borazine which is why the second most popular precursor is Borazine itself only in liquid form.

The problem with liquid Borazine is that it is highly susceptible to ambient and very difficult to handle within a CVD system. An intermediate product that is more robust at ambient conditions and releases mostly Borazine is therefore greatly desirable. As mentioned before this product can be obtained by the addition of Tetraglyme to solid AB to form DADB which releases as much as 40 wt% Borazine when it evaporates. One last point regarding the thermolysis of AB is how the heating rate effects the yield of gaseous products (Shown in Fig. 6c). Baumann had shown that as the heat rate increases from 0.5°C/min to 5°C/min the amount of volatile products apart from H_2 increases with MAB always being the major contributor. This seems like a desirable outcome since it would increase the partial pressure of the active species possibly leading to better control of the flow rate, however it has also been shown that as you increase the heat rate the AB undergoes melting more readily as well. Therefore, it is always desirable to keep the initial heat rate as low as possible (~0.1-1°C/min).

The thermolysis was also studied with respect to quantity of AB used. It was found that quantity (in mg) of AB loaded had little effect on the onset of melting [24]. However, for larger

quantities it was reported that non-uniform melting of the AB powder was observed. This overall leads to a mixture of areas where the conversion to PAB will have occurred to completion and areas of crystalline AB. This is expected in powder like materials due to air gaps inevitably present between individual grains, these airgaps lead to non-uniform thermal conductivity within the powder which causes non-uniform melting.

From what has been studied up to this point it can be seen that the thermal decomposition of AB is very complicated and depends on numerous factors such as: Heat rate, uniformity of load, exposure to ambient and temperature. As a finally summary of AB thermolysis we present some concluding comments on proper usage and guidelines for growth of CVD hBN using this precursor.

- Always keep the AB stored at low temperatures (T~0°C) to avoid polymerization of AB.
- Avoid exposing the AB to ambient for prolonged periods since humidity also leads to polymerization.
- Try to maintain the powder uniformly spaced in the container in order to minimize non-uniform heating.
- Maintain a small heating rate (~0.1-1°C/min) in order to avoid unintentional melting of the AB and prolong its lifetime.
- Maintain a final temperature below 90°C in order to minimize the "melting" of AB and prolong its usage (~60-70°C is ok).
- Keep the growth temperatures above 1000°C in order to promote complete dehydrogenation of any reactive species and obtain better crystal quality hBN. More on this note will be discussed in Chapter 3.

Keeping all these factors in mind, which are actually easier to maintain than other precursor',

we can study the progress made in recent years with regards to the pressure dependence of growth using AB. Both APCVD and LPCVD have been heavily studied and it seems that LPCVD has shown more reproducible and controllable results with regards to morphology and layer control. Koepke et al. has done a great systematic study on the role of pressure in the CVD growth of hBN [25]. They identified key trends that have been previously reported in various results over the years (See Fig. 7g), specifically they showed that as you increase the pressure beyond ~2torr the hBN begins to form sp3 bonds and is no longer a layered structure. These results are presented in Figure 7a-f. Furthermore, they demonstrated that high precursor flux lead to nanocrystalline sp3 hBN films regardless of the pressure regime. These sp3 hBN films did show larger crystal sizes in the LPCVD regime. They further investigated the role of H_2 in hBN growth and found that the main factor that controls crystallinity is the H_2 to precursor ratio (i.e. partial pressure). A high ratio and low pressures (<2torr) will give layered crystalline hBN films. Other investigations have shown that under APCVD the grown films are sensitive to position and non-uniform growths were observed along the length of a Cu foil [23]. This result can be attributed to the key difference in gas flow that occurs in the two pressure regimes. Under atmospheric pressures the gas flow tends to be more turbulent leading to irreproducible and many times uncontrollable growth. At low pressures one transitions into the laminar flow regime which is much better controlled and the partial pressures of the gasses can be easily manipulated under these conditions. Of course, the regime in which a particular CVD system operates depends on its size and the efficiency of the pumping system as well as the molecules that are flown, these factors are all taken into account with the Reynolds number which gives a rough estimate of when the transition from turbulent to laminar occurs [26]. Another problem with high pressure growths is the increased gas flow reactions due to the increased pressures, this because the mean separation between molecules is

decreased as pressure increases leading to more collisions at high temperatures, hence, more chemical reactions. Although APCVD is a more economically viable option to LPCVD since one avoids expensive vacuum pumps, the disadvantages of working in this regime out way the cost and LPCVD is generally preferred.

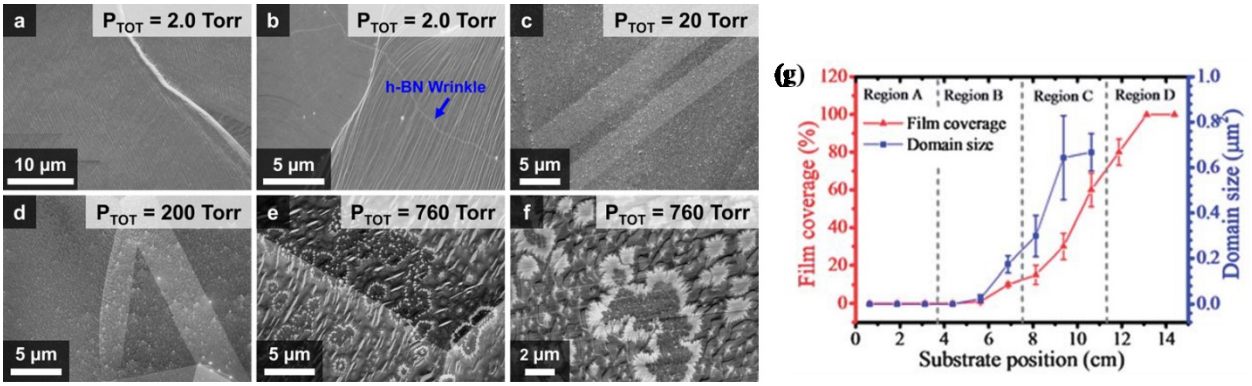

Figure 7 :(a-f) Morphology variation of hBN/Cu as a function of pressure. Taken from Ref. [25]. (g) Film and domain size variations as a function of position within the furnace observed in APCVD. Taken from Ref. [27].

2.2 Liquid CVD

With regards to using liquid precursors in the CVD growth of hBN there have two main chemicals used, these are Borazine (shown in Fig. 8a) and Boron Tricholoroborazine (BTC, shown in Fig. 8b). They are both aromatic molecules and have similar properties as well as similar downfalls, because of this only Borazine (the more popular of the two) will be treated in this

section. The main disadvantage with the usage of BTC is its purity. BTC is an opaque solid at room temperature and melts at ~75°C, its corrosive when exposed to air and hydrolyze to form HCl. Researchers have found that BTC must be put through several melting/freezing cycles before suitable for growth and even then, the growth has to be done at ultrahigh vacuums to maintain the stability and purity of the BTC [28]. Another seldom used liquid source is Triethyl-Boron (TEB) however its usage is not recommended since its highly unstable in air and can spontaneously combust [15] but it's worth mentioning since TEB was the boron source of Nakamura et al. when he initially grew the first crystalline hBN thin films [3].

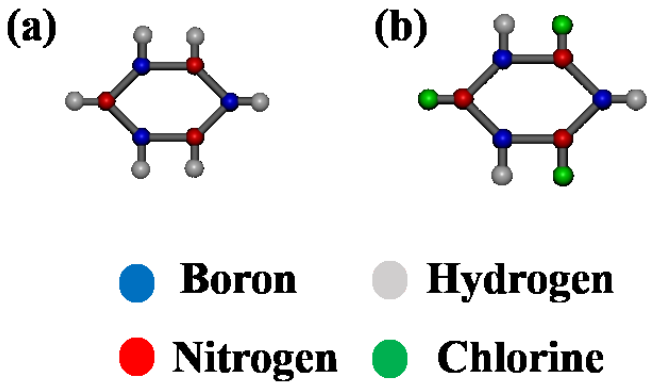

Figure 8 :(a) Borazine molecule. (b) Boron Trichloroborazine molecule.

2.2.1 Borazine Precursor

Borazine was first synthesized in 1926 by Stock and Pohland [29] by the chemical reaction between Di-Borane and Ammonia whereby the gas mixture was heated in a pressurized contained to obtain liquid Borazine. Stock is also attributed with laying the foundations for the field of boranes in general. At room temperatures Borazine is a colorless liquid which is quite unstable and sensitive to moisture. It has been shown that Borazine readily decomposes to boric acid, ammonia and hydrogen in the presence of water. For this reason, Borazine is typically stored at

low temperature (<°C). Borazine was also the precursor used to synthesize the first monolayer of hBN on a Ni foil by Nagashima et. al. [30]. Due this first success they paved the groundwork for future findings in CVD hBN. They were able to find that after the initial monolayer completely covered the underlying Ni catalyst the growth rate reduced by three orders of magnitude. They also identified that after the initial monolayer the growth proceeds by Stranski-Krastanov mode (i.e. Island mode) instead of layer by layer, this finding is in accordance with modern CVD techniques as well [23]. At the time there was heated debate as to the electronic structure of this monolayer (i.e. its dispersion relations) and many different theoretical calculations predicted different bandgaps amongst other properties [31]. Nagashima resolved this debate to a great extent by isolating a crystalline monolayer of hBN and performing Angle Resolved Ultraviolet Photo-Electron Spectroscopy (ARPUS) as well as Angle Resolved Secondary Emission Spectroscopy (AREES) on the as grown hBN/Ni stack. Their experiments lead to the first experimental determination of the work function for monolayer hBN (~3.6eV) as well as accurate widths of the σ and π bands, a value crucial for the determination of the effective mass of carriers in hBN. The bandgap was still at the time underestimated to a value of ~4.6eV, this value and the direct or indirect nature of the gap was only resolved recently in 2016 [32]. In a follow up study in the same year Nakamura showed that hBN monolayers are weakly adsorbed to the surface of metals such as Pt an Pd with adsorption energies that put it in the physisorption range (<0.1eV/atom) while on Ni the binding is stronger by ~1eV [33]. This effect is of great importance since it has been determined that rare gas solids which are also physisorbed on metal surfaces actually change the work function of the metal in to reach equilibrium flat band conditions. The same effect was found with hBN on these metal surface where changes as large as 1.9eV where observed (See Fig. 9). For the purposes of this thesis, this is an important finding to understand the band alignments of

hBN with metals and use it as a conducting layer.

Substrate	Work function		N 1*s*		B 1*s*		π band (at $\bar{\Gamma}$)		σ band (at $\bar{\Gamma}$)	
	Clean	BN covered	E_B^F	E_B^V	E_B^F	E_B^V	E_B^F	E_B^V	E_B^F	E_B^V
Ni(111)	5.3	3.6	399.1	402.7	191.3	194.9	10.3	13.9	5.3	8.9
Pd(111)	5.3	4.0	398.2	402.2	190.5	194.5	8.7	12.7	4.8	8.8
Pt(111)	5.8	4.9	397.3	402.2	189.7	194.6	8.2	13.1	3.9	8.8

Figure 9 :Table I taken from [33] showing the work function change of metals when covered by a monolayer of hBN.

Lastly, the pressure regime that has been used for growth via Borazine is in the High Vacuum (~10^{-8} torr) [34, 30, 35]. This is due to the volatility of the liquid which tends to release other gaseous species as the precursor is increased. This limitation to the high vacuum regime increases the costs of a CVD exponentially due to the need for high vacuum pumps and other specialized equipment. A study performed on Cu is shown in Fig. 9a-c where they demonstrated that complete coalescence occurs by simply increasing the growth time. Furthermore, there have been reports of growing at atmospheric pressures using borazine, however, these results were done by initially maintaining the catalyst at a low temperature (<450°C) while flowing the gaseous species in order to deposit non-volatile oligomers containing B and N. The catalyst with the layer of oligomers on it was then heated to T>1000°C in order to crystallize them and create hBN [36]. This method, although done using APCVD, has not shown promise due to its lack of layer and morphology control. The results of films grown via this method are shown in Fig. 9d-e. Its not made clear whether or not the regions within the observed grain boundaries in these images are single crystal or not.

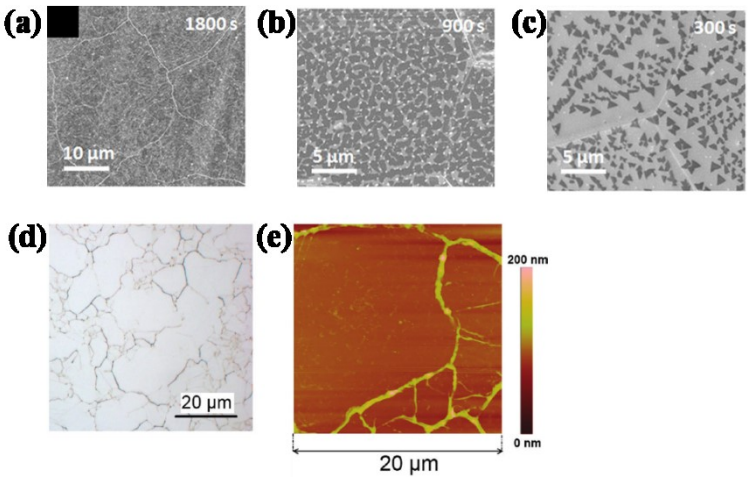

Figure 10 :(a-c) An hBN film grown by borazine at ultra-high vacuum on Cu foil [35]. The study shows that films coalescence can be achieved by simply increasing the growth time. (d) Optical image of hBN/Ni grown by APCVD using borazine [36]. (e) AFM image of hBN/Ni grown by APCVD using borazine [36].

2.3 Gaseous CVD

Using gas sources of Boron and Nitrogen is a great alternative to the Solid and Liquid sources due to the ability to easily control the volume flow of the gases. One difficulty in using separate B and N supplies is that the stoichiometry is more difficult to tune and the parameter space where hBN grows may be difficult to find. Inspite of this many groups have demonstrated good control of hBN growth using gaseous precursors [37, 38, 39]. The main problem with gaseous precursors is their toxicity which is why this method has not been as popular as others. Until non-toxic boron gaseous sources are found using Gas CVD will be remain a challenge.

To the best of our knowledge the most extensive and detailed study on gaseous precursors was done by Ismach et al. at using ammonia and diborane [38]. They worked in the LPCVD regime and were able to obtain layer control of their films as shown in Fig. 11a. They also established that at temperatures below 800°C nanocrystalline or turbostatic hBN was obtained regardless of the gas partial pressures which they attributed to the poor decomposition of Di-Borane at T<800°C.

This topic was also treated in Section 2.2.1.1 for the AB precursor. They also demonstrated that poor crystallinity is obtained at T~1000°C for hBN on Sapphire substrates (Fig. 11b). This was recently confirmed and resolved by growing hBN on sapphire at T>1300°C using the AB precursor [40]. In their report they also came up with a novel method to grow hBN which is very similar to atomic layer deposition (ALD) whereby they fed only the N (B) gas source followed by a H_2 clean and then fed the B (N). This enabled them to obtain great control over hBN thickness as show in Fig. 11c-d. Another crucial factor that they demonstrated was that BN particles are regularly seen for long growth periods due to their desorption from the chamber walls. We have also confirmed this fact in our experiments. Lastly, they made a very important contribution to the field by confirming that hBN growth at LPCVD is not dominated by gas phase reactions but rather by catalysis at the substrate. This is great since gas phase reactions are always undesired in CVD and lead to poor crystallinity. We note that this result is not in contention with our previous discussion about the gas phase reactions likely to occur using AB since they had no MIB in their gaseous products.

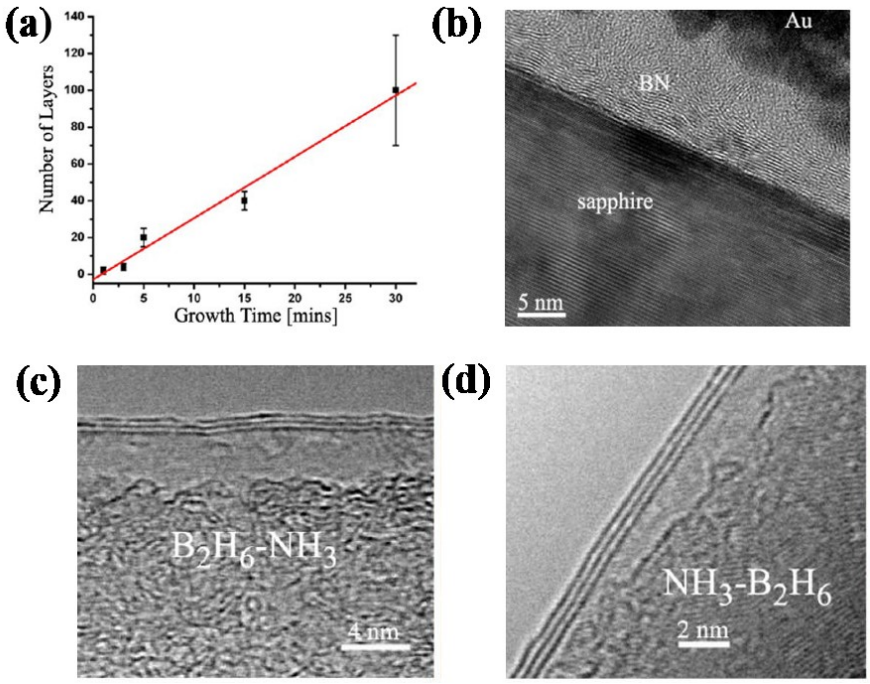

Figure 11 :(a) Linear dependence of hBN thickness with growth time showing that the film is not limited to a monolayer. (b) Cross sectional TEM of hBN grown sapphire showing amorphous films. (c) Cross sectional TEM of hBN on Ni grown by feeding the B_2H_6 first and the NH_3 second Cross sectional TEM of hBN on Ni grown by feeding the NH_3 first and the B_2H_6 second.

In summary, gaseous CVD can be great resource for industrial and academic endeavors focused on obtaining large area hBN. It has demonstrated potential to control the thickness and stoichiometry of the resulting films quite well and has even been shown to function similar to ALD growth. However, until nontoxic precursors are found, gaseous CVD has remained mostly as a less popular academic tool.

2.4 High Pressure High Temperature (HPHT)

This section will discuss the methods used to obtain bulk single crystal hBN which are quite different than conventional CVD. However, it's important to discuss these methods since they are currently the only means to obtain layered single crystal hBN. The single crystals obtained are typically limited to ~100um and due to the exfoliation method used they can't be controlled for

thickness. Due to these reasons they are employed mostly in the academic world for fundamental research.

The growth method used for produced high quality (i.e. semiconductor grade) single crystals of hBN is typically called a Hydrothermal Melt growth. Its has historically been used for many materials including Ge, Diamond, Graphite, GaP, $BaTiO_3$, GaN and of course Si amongst others [41]. Hydrothermal growth is an expansive subject with many different techniques contained under this category, it is not the intention of this section to do an exhaustive review of all the methods but rather to get a feel for how the method is employed in hBN growth. For the interested reader there are many other sources that go in depth on the topic [41, 42].

The essence of the growth technique used for hBN is a re-solidification of a molten solution where the molten solution is composed of hBN and another metal catalyst (Ni for the case of hBN) [11]. The starting solid mixture contains hBN powders and Ni flakes which are then taken to pressures above 5GPa and temperatures above 1300°C. We note that the role of the Ni (or any other catalyst used) must be to promote the formation of hBN and is carefully selected so that it satisfies certain constraints: (i) It must not react with hBN (ii) should have small vapor pressure. The role of the high pressure is two fold (i) it increased the solubility of BN in Ni and (ii) it increase the liquidus temperature of the solution. Higher solubility is needed to avoid earyl supersaturation and unwanted recrystallization whereas higher liquidus temperatures are needed so that the solution remains in the liquid form until the desired crystallization temperature is reached (~1300°C for hBN). Once the solution has reached the desired pressure and temperature spontaneous re-crystallization of hBN within the melt occurs where supersaturation is the driving force. The solution is then quenched to room temperature and a Ni solid with hBN crystals in it is obtained. The Ni is then removed via acid etchants which do not attach the hBN and the remaining

hBN crystals are collected.

The initial method for semiconductor grade hBN by HPHT was developed by Kubota et al. [11] where they were able obtain small crystals of 10-25um in size (Fig. 12a). Their initial study involved both the formation of cBN and hBN and presented a phase diagram for these materials within the Ni molt as reproduced in Fig. 12d. They studied the luminescence of their hBN crystal and were able to get detailed band edge properties showing excitonic peaks which demonstrated the purity of their material (Fig. 12e). In a follow up study they changed the solvent to a Ni-Mo alloy and were able to obtain millimeter sized crystals at atmospheric pressures and high temperatures (APHT) as shown in Fig. 12b. This opened the doors to using Liquid Phase Epitaxy (LPE) where a sapphire substrate was used with the molten Ni-Mo + hBN solution to yield highly crystalline hBN on Sapphire (Fig. 12c). which have become the standard crystals used today in academics [43].

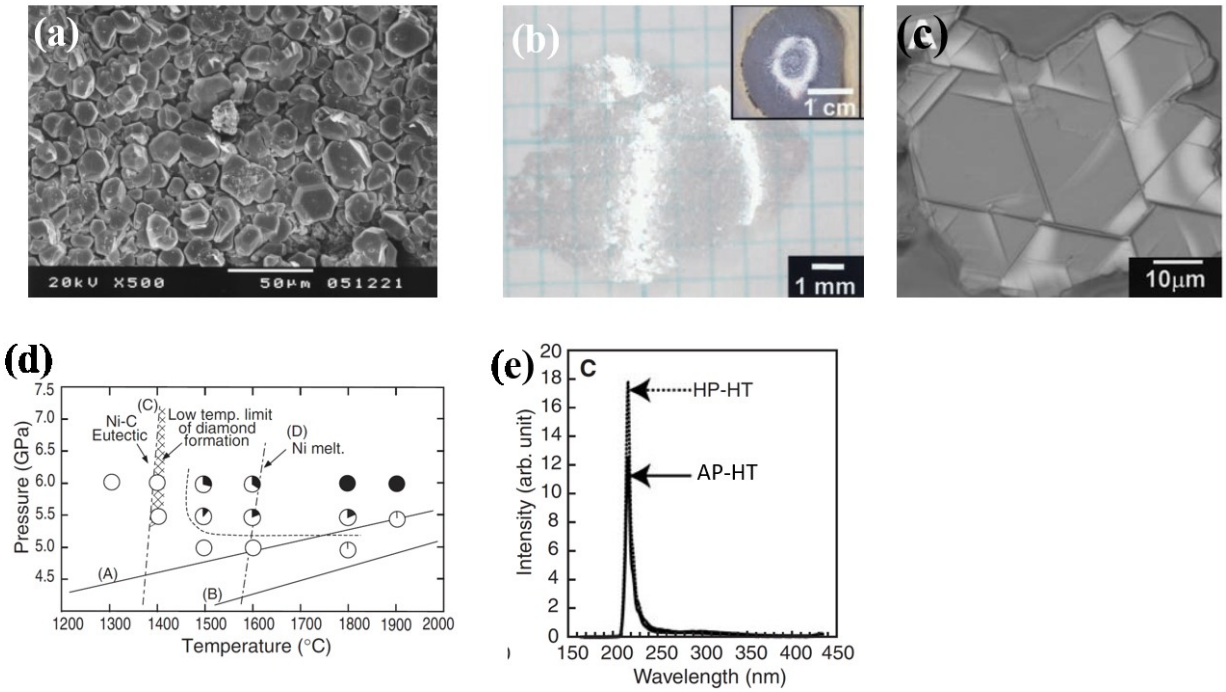

Figure 12 :(a)SEM image of hBN crystals formed by HPHT method [11]. (b) White light image

of hBN grown by APHT method [43]. (c) hBN on Sapphire synthesized by APHT method [43]. (d) Phase diagram for hBN and cBN formed in a HPHT process. (e) Cathode Luminescence comparison of hBN grown by HPHT and APHT showing good agreement between both and high quality hBN.

Finally, before we digress into the next section we leave a summary of the most common precursors and their respective downfalls.

Table 1 : List of precursors for CVD growth of hBN including their downfalls.

Precursor	Room Temp. Composition	Composition to deliver precursor	Major Downfalls
Ammonia-Borane	Solid	Solid	No control of gas flow
DecaBorane	Solid	Solid	Spontaneous ignition in air. Stoichiometry control difficult.
$(BNHCl)_3$	Solid	Liquid	Spontaneous ignition in air. Ultrahigh vacuum needed. Purity grade low.
Triethly-Boron	Liquid	Liquid	Spontaneous ignition in air. Ultrahigh vacuum needed.
Borazine	Liquid	Liquid	Unstable in air. Ultrahigh vacuum needed.
BF_3+N_2	Gas	Gas	BF_3 is toxic and corrosive.
Diborane+NH_3	Gas	Gas	Poisonous. Flammable in air. Reacts with H_2O

3 Chamber Design

Here we will briefly describe our chamber design and its components. This is necessary at this point since we will begin presenting our preliminary results in the following sections and an understanding of the physical system needs to be in place prior to presenting these results.

A simplified schematic of our chamber is shown in Fig. 13 where some relevant dimensions are noted such as the length of the quartz and it inner diameter (6cm). Our system consisted of a conventional split tube furnace with clamshell heating elements capable of temperature up to 1250°C. Temperature within the flat zone was monitored using a thermocouple. A fused quartz

tube was used within the furnace. Stainless steel tubing was used to connect the various components and throughout the system (MFC's, pressure gauge's etc..). A total of four gas lines were available for usage, however, only two were used during growth since only H_2 and Ar were needed. The AB was contained in a custom made fused quartz container that was displaced from the gas inlet for a distance of ~45cm (1.5ft). The AB was heated using conventional heat tape and the temperature was monitored using a thermocouple. A pressure gauge at the outlet of the AB contained was used monitored the pressure of the sublimed gases from the AB. The sublimed gases from the AB reached the hot zone by diffusion through a length of ~20cm and were then carried into the hot zone via the carrier gases (H_2 or Ar or both). Another pressure gauge was placed at the outlet of the CVD tube to monitor the system pressure. A roughing pump was used to evacuate the chamber down to ~3-5mtorr.

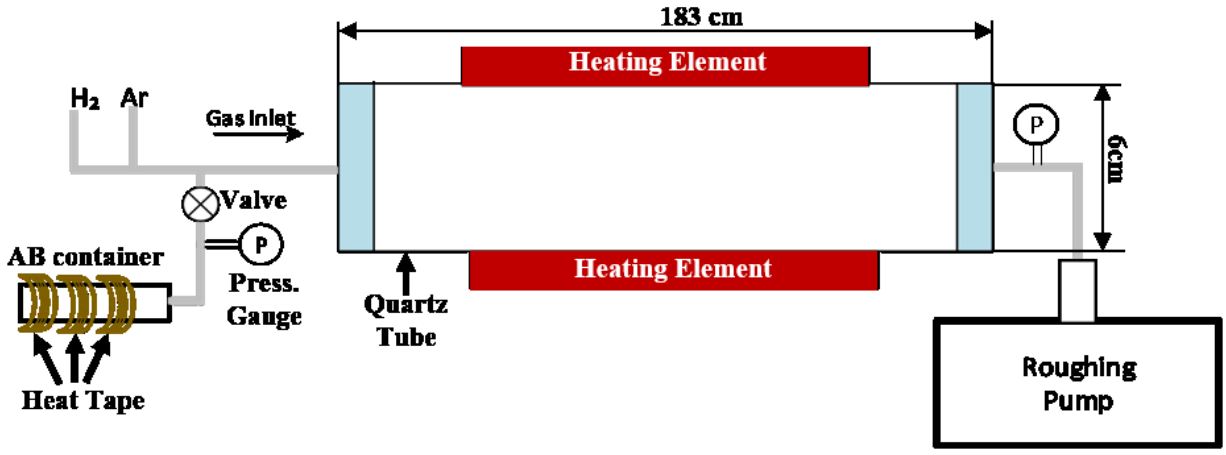

Figure 13 : Schematic representation of the CVD system used for hBN growth.

4 Role of Catalyst

A catalyst by definition is a substance that increases the rate of a chemical reaction without

itself undergoing a permanent change or changing the thermodynamics of the process. A working definition more appropriate for our purposes is "a substance that promotes the formation (i.e. growth) of a crystal on its surface rather than in the gas phase (i.e. deposition)". This statement says that molecules near the surface of our catalyst will preferentially form a crystal on the catalyst surface then a deposit within the gas. The catalytic behavior of materials can be quite complex [44], however, a simplified definition can be used for metals which are typically good catalysts due to their incompletely filled orbitals (i.e. free electrons) which enables them to give and receive electrons at their surface facilitating chemical reactions. Complexity enters when we consider things such as surface energy which depends on atomic packing factors which in turn depends on crystal orientation. External factors also determine catalytic behavior including temperature and pressure.

In our experiments we used mainly two metals, Ni and Cu, which gave distinctly different results and will be discussed in the sections below. The goal of this section is to introduce our intial results and the reason why we choose to optimize our growths on Cu and avoid Ni. The full optimization scheme on Cu will be presented in chapter 3. Other so called "non-catalytic" substrates were also attempted and will be discussed in the "others" section.

4.1 Ni

Many of the initial work on hBN used Ni as the catalyst due to the close lattice match between Ni and hBN (~0.1% mismatch [36]) as well as the success that Nagashima et al. had in synthesizing the first monolayer on Ni [33]. Throughout the years the community has realized that the lattice mismatch didn't play such a large role in growth of 2D materials due to the weak bonding with the substrate [23], instead, more important factors such as diffusivity of Boron and Nitrogen as well as thermal expansion coefficients were more relevant.

Before presenting our results on Ni its noteworthy to mention that all of our work was done at parameters which are well within the scope of a zero-dimensional plug flow growth system (See Appendix A for details). This means that our growths will be surface reaction limited at the catalyst surface which in turn means we will have uniform deposition along the length of the tube. Deviations from non-uniformity will likely be due to second order effects not considered in the plug flow model such as boundary layer thickness, parabolicity of the velocity profile, thermal diffusion currents etc.

Our initial efforts at growth of hBN on Ni were done on Ni foils ~100um thick purchased form Alfa Aesar. We used large quantities of AB (~3-5g) placed within the AB container and heated it to temperatures between 90-100°C. This was done in order to produce sufficient vapor pressure from the AB in order to control the flow with a MFC. As explained in section 2.2.1.1 this leads to melting of the AB and the majority of the vapor species are H_2 instead of B and N containing molecules. Thus, reproducibility was difficult with these parameters (as we painfully learned) and adequate control of the growth was not obtained. To the extent that we were able to control reproducibility we obtained some important initial insights from these initial experiments. Shown in Fig. 14 Is a series of AFM images taken from growths of hBN on Ni foils while varying both the time (x-axis) and flow of AB (y-axis). From these images we can see that at long growth times increasing the AB flux actually leads to a smoother film. This is expected since at high precursor concentrations and large times we will obtain very thick films and variations in the roughness due to the catalyst surface or other phenomena will be minimized since CVD growth is a conformal coating process. In order to study the role that the substrate plays with regards to film morphology the time was decreased to 20min. and the AB flow was varied in the same manner. A different scenario is seen now whereby increasing the precursor flux leads to increased film

roughness. This is now understood due to the formation of spherical deposits of BN molecules which adhere to the surface during the initial monolayer nucleation and act as defect centers which getter B and N species leading to 3D growth (Volmer-Weber) [6, 45, 46]. When transferring our thick hBN films (long time at large flows) we were able to confirm that the morphology is indeed quite rough and the films are thick, as shown in Fig. 15a.

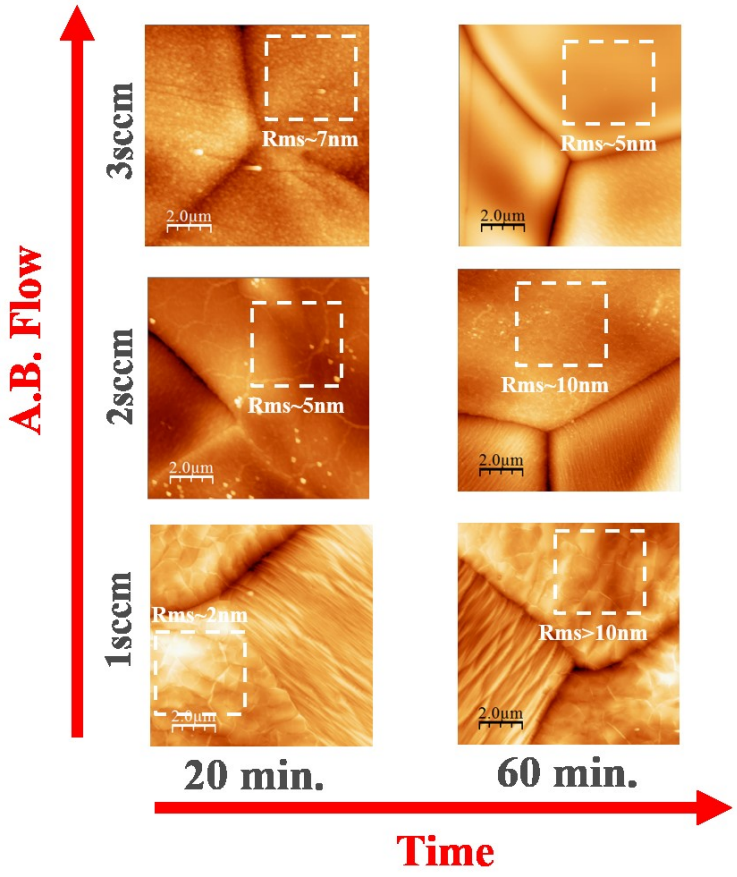

Figure 14 : AFM images of the surface morphology of several growths of hBN on Ni foils (~100um thick) by varying the growth time (x-axis) and AB flow (y-axis). The white dotted boxes within each image depict the region over which the roughness was estimated.

The as grown films on Ni foil were further analyzed using Raman spectroscopy and special attention was paid to the thinnest films grown at 20min with a flow of 1sccm of AB (See bottom

left of Fig. 14). Figure 15b shows an AFM scan of one of these films where the intersection of Ni grains is clearly visible. Furthermore, one can observe steps in the grain on the left while the other two are smooth. Raman was taken on both types of Ni grains (smooth and step bunched) as shown in the inset to the right of Fig. 15b, and the characteristic hBN shift near 1365cm^{-1} [47] was only observable on one grain and not on the other. This was explained due to the different catalytic constants of different Ni faces where it was shown that the growth rate of hBN on the (100) plane is much larger than that on the (111) [48]. This is the main reason why Ni was avoided as a catalytic substrate for hBN growth. The large difference in ks leads to non-uniform growths even when the fluid dynamics of the system show that we're in the uniform range (i.e. surface limited). As mentioned earlier this is one of the second order effects which can lead to non-uniform deposition which are not considered in the plug-flow model.

We conclude this section by noting that recent work using Cu-Ni foils has shown that multilayered hBN can be grown controllably and uniformity is well maintained throughout [49], however no insight was given as to how the problem of reactivity was overcome. Recent work has shown Cu-Ni alloys [50] lead to increased crystallinity by taking advantage of the difference in surface reactivities of these metal, however the problem of growing uniform hBN on pure Ni foils remains unsolved [51].

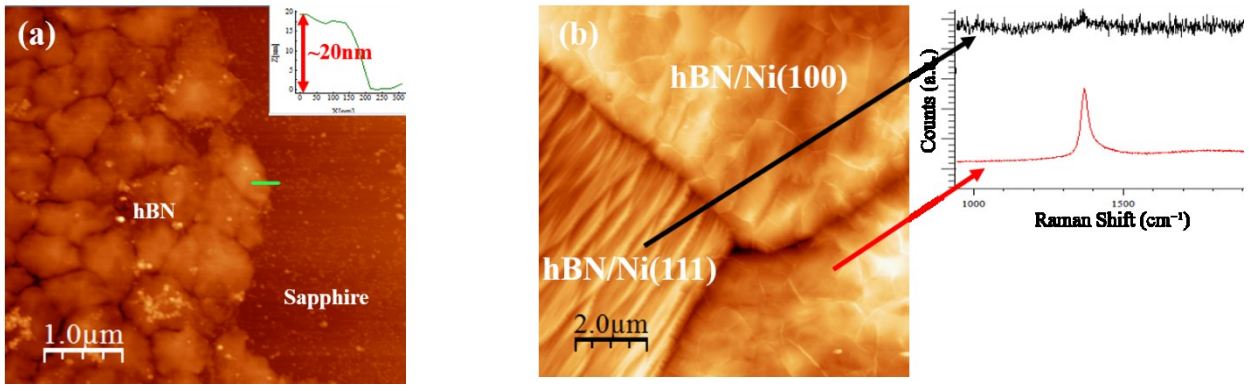

Figure 15 :(a) AFM scan of a thick hBN film transferred to a sapphire substrate. The inset in the

upper right shows the height analyses at the edge of the transferred film which estimates a thickness of ~20nm. (b) AFM scan of a thin hBN film grown on Ni where different Ni grains are observed. The inset to the right of the image is a Raman spectrum taken at different Ni grains showing that the (111) (black spectrum) orientation has undetectable hBN while the (100) (red spectrum) orientation has a clear hBN peak.

4.2 Cu

Initially Cu was seldom used in hBN growth, however once the downfalls with Ni started to become evident Cu quickly became the preferred catalyst. The lattice mismatch between Cu and hBN is also very small with hBN having ~2% smaller lattice than Cu(111) [52]. More importantly, experiments found that the film deposition was quite uniform over the entire Cu surface and the kinetics didn't change much [23]. This was the crucial factor that lead to the hBN/Cu system being well studied and used for CVD growth. One reason why Cu is superior for hBN growth is explained due to the occupation of the 3d states of Cu vs Ni [53]. Nickel has only partly occupied 3d states located near the metals Fermi level making those states highly energetic, while Cu has a fully occupied 3d orbital with state 2-5eV below the fermi level. This difference is key to the catalytic behavior of each metal since hBN is strongly chemisorbed on Ni while only weakly chemisorbed on Cu. Thus, in a surface reaction rate limited experiment, one would expect that difference in the Cu's Ks (due to different faces of the Cu in a typical polycrystalline foil) play much less of a role than they do in Ni. Another potential factor is the diffusivity of B and N atoms into Cu and Ni. Unlike the case of Gr where it was shown that C has a much smaller diffusivity into Cu than it does into Ni, therefore making Gr growth on Cu purely surface mediated [54], for hBN it has been shown that B can easily diffuse into the subsurface and bulk of Cu and Ni, while the diffusivity of N into these same catalysts is much smaller [35, 51, 55]. Therefore, the role of the subsurface is important in both Cu and Ni and cannot account for the variations in growth seen with these

catalysts. Experimentally the uniformity of hBN growth on Cu was confirmed with the first synthesis of a monolayer of hBN on Cu in 2012 by Kim et al. [56]. Using LPCVD and AB as the precursor they demonstrated that the growth on Cu was uniform and not self-limited as it was for Gr on Cu [54]. The growth was shown to proceed as island on layer (Stranski–Krastanov) after the initial monolayer was formed, thus layer by layer growth was proven to be difficult in this system. Lastly, they were also the first to report the effects of electro-polishing pre-treatments on Cu foils which were shown to decrease nucleation density and consequently increase grain size. Thus, the main difference and advantage that Cu holds over Ni is its weak surface interaction with hBN during growth enabling uniformity and layer control.

All of the above results where confirmed in a very nice systematic study done by Kidambi et al. [35] where they used in-situ XPS and XRD to study the growth evolution in real time of hBN on Cu. Their deduced growth model is shown Fig. 16 where they propose that initially the precursor molecule (Borazine) arrives at the Cu surface and dissociates into B and N atomic species. From there B has two competitive venues for diffusion, this is either into the Cu subsurface or along the surface. Nitrogen on the other hand only diffuses on the Cu surface. At equilibrium the surface flux of B and N must be equal in order to form stoichiometric hBN ($J_b = J_N$ as shown in the figure), since there will be an excess of B supply due to diffusion into the Cu multilayers can be formed if N is supplied to the Cu interface after the initial layer has formed. This type of growth is very similar to the "bottom up" growth observed for Gr on Ni and explains why hBN is not self limited to monolayers on Cu as Gr is. The difficulty comes about in the continued supplied of N to the underlying Cu after the initial layer has coalesced, N would have to diffuse through hBN grain boundaries or other defects in the sheet, this effectively increases the growth rate of subsequent layers by orders of magnitude. Again, this model explains the reason why Nakamura

[30] observed an exponential increase in growth time of hBN on Ni in his experiments. A more important problem with this bottom up or surface segregation method is that we've effectively introduced a huge diffusion barrier (the coalesced hBN layer) into the system. This is qualitatively equivalent to increasing the stagnant layer thickness to the extent that the growth mode is no longer surface limited but mass transport limited. Growth in the mass transport limited regime is highly non-uniform and good control of the layer number is unlikely. This is the main reason why electronic grade multilayer hBN has yet to be achieved in CVD, although some groups have shown that its possible to grow thick hBN, the crystal quality of this thick material is typically low.

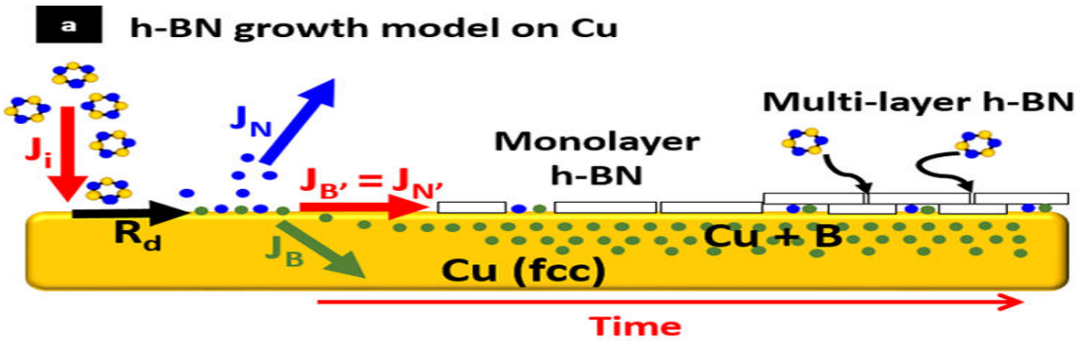

Figure 16 : Growth mode of hBN on Cu using LPCVD and liquid borazine as the precursor [35].

We present some of our initial results of hBN growth on Cu in Fig. 17. These growths were performed with similar conditions to those used for Ni where ~1g of AB was loaded into a quartz container and was heated with heat tape up to ~90-100°C. Argon was used a carrier gas and the temperature of the growth zone was set to 1000°C as measured by a thermocouple. As the flux of the carrier gas was increased while keeping the growth time constant (30min.) the morphology observed in SEM looked more uniform. This is the same trend that was observed for Ni and can be explained due to the thicker films formed at higher fluxes. The important difference was that Raman analysis on our Cu foils showed the presence of hBN everywhere. This is shown in Fig.

17d where representative Raman spectra are shown for three different Cu grain all showing the E2g peak at ~1370cm^{-1} characteristic of hBN.

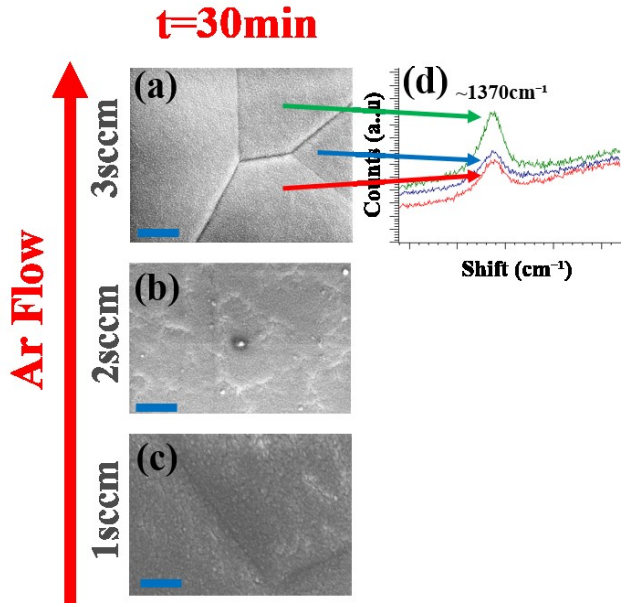

Figure 17 : (a-c) SEM micrographs of several growth of hBN on Cu. The SEM shows the qualitative difference in morphology as the carrier gas (Ar) flux is increased will keeping the growth time constant. (d) Raman spectra taken at three Cu grains showing the presence of hBN everywhere.

4.3 Others

H-BN growth was also attempted on a variety of other substrates apart from Ni and Cu, in this section we'll introduce some preliminary results on these substrates as well as some recent literature results.

Non-metallic or so called non-catalytic substrates such as Sapphire, SiO_2 are of great interest to the electronics industry due to their role as potential gate dielectrics which can be used in the fabrication of MOSFETs. Direct growth on these substrates also avoids the necessity to transfer the 2D material since these substrates are compatible with conventional fabrication technologies. As an example, the growth of Gr on Sapphire or semi-insulating SiC was first

demonstrated in 2010 by Hwang et al. [57] and opened up the potential to produce large scale 2D materials directly on insulating substrates suitable for large scale processing and fabrication. In these initial results poor layer control was shown and little knowledge of the detailed growth process was given, however in a seminal follow up study in 2013 Hwang et al. [58] both of these issues were resolved where layer control and a detailed growth process were developed. Today the field of CVD growth of 2D materials on non-metallic substrates is vast and in some cases, has shown to produce materials that are of competitive quality with those grown on metallic substrates [59].

This was our initial motivation to attempt growth of hBN directly on Sapphire and include hBN in the family of non-metallically produced CVD materials. Our initial results are shown in Fig. 18 where we used ~1g of AB and we were subliming it at temperature up to ~100°C, the temperatures and pressures used were 1050°C and ~1torr respectively with a growth time of 30min. As shown in the optical micrograph of Fig. 18a the deposited hBN is highly non-uniform and patchy. The difference in color is due to a combination of different thickness' as well evidence of three dimensional (i.e. sp3 bonded) hBN present since sp2 hBN is strictly transparent in the visible range. The raman analysis in Fig. 18b confirms that both the presence of hBN everywhere on the surface along with the characteristic Sapphire peaks of the substrate. AFM micrographs were taken at three distinct regions shown in Figs. c-e where the overall morphology is quite rough. Fig. 18e shows the presence of clustered 3D islands likely formed by sp3 bonded hBN. Fig. 18c is a bit interesting, it gives insights into how this non-uniform growth may have progressed with the green colored regions serving as the initial layer facilitating further growth and coalescence of the circular blue regions. This type of growth can be attributed to random agglomeration around a nucleation center due to low mobility of the gas molecules on the surface of Sapphire at 1000°C

[60]. This was later attributed to the diffusion of large polymeric molecules form the high temperature used for sublimation of our AB as explained previously. At the time we were still unaware of the chemistry involved in the decomposition of our precursor and suffered the consequences. After this initial attempt we lowered the temperature of our precursor to ~70°C and obtained drastically different results as shown in Fig. 19a-d. The AFM micrographs in Fig. 19a and c show a uniform film with very low roughness typically of layered hBN, furthermore Raman analysis in Figs. 19b,d shows a weak but evident hBN peak located at ~1370cm^{-1}. Fig. 18 c is a 45min growth while Fig. 19a is a 30min growth. No difference in morphology of Raman resonance was seen in these experiments, however, the precise thickness of the films was not verified with other methods. In Figs. 19e-h we show AFM micrographs and Raman analysis of CVD hBN films grown Sapphire by the use of gaseous precursors (Diborane and Ammonia) produced by Structured Material Inc. (SMI). The temperatures and pressures were similar and the materials quality was also comparable to ours. The films produced were not studied further due to the lack of reproducibility and low temperature decomposition of the hBN. The intent was to use the hBN/Sapphire substrate as a starting substrate for the growth of Gr/hBN/Sapphire samples at high temperatures up to ~1400°C, however the hBN films degraded at values much lower than expected (T~1000°C) which indicated poor crystallinity of our films. This was recently explained in a paper by Jang et al. [40] where temperature up to 1400°C were necessary to grow crystalline hBN on Sapphire substrates. The also demonstrated that wrinkles are greatly suppressed in hBN/Sapphire due to the small difference in thermal expansion coefficients. We note that reaching those temperatures in our experiments was not possible due to the glass transition temperature (~1150°C) of the Quartz processing tube. Jang et al. used an alumina tube which enabled them to reach temperatures up to 1400°C.

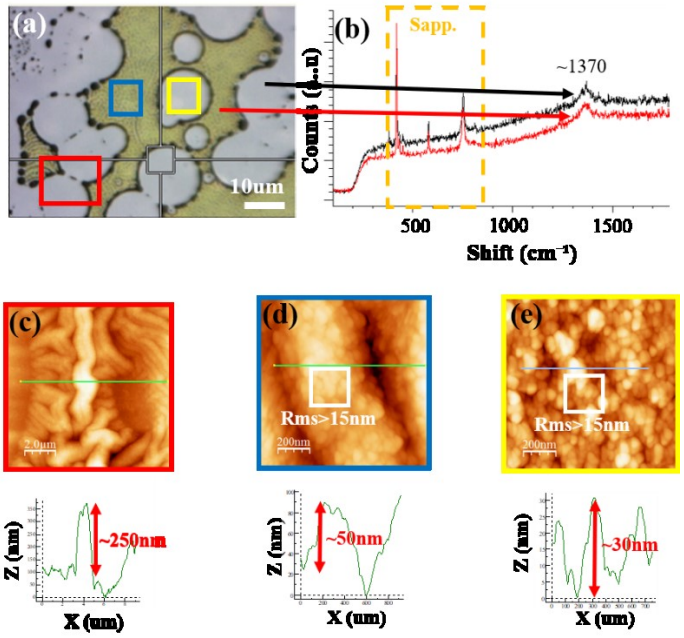

Figure 18 : (a) optical micrograph of hBN grown on Sapphire. (b) Raman analysis of the purple region (red spectrum) and green region (black spectrum) showing the hBN peak was found everywhere along with the characteristic Sapphire peaks. (c-d) AFM micrographs taken at three different positions shown in colored boxes in (a). Below each micrograph is the corresponding height analysis taken across the image.

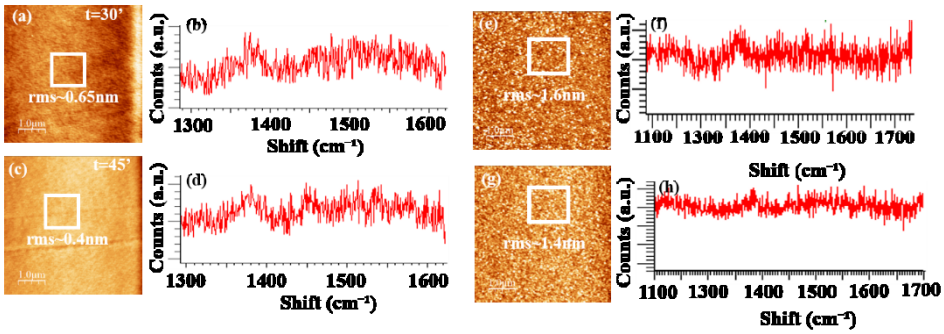

Figure 19 : (a,c) AFM micrographs of CVD hBN grown on Sapphire using AB for times of 30 and 40min respectively. Roughness values are shown in each picture and are similar to CVD hBN on metals. (b,d) Raman spectrum of the hBN/Sapphire films in (a) and (c) respectively. A small peak is observed at ~1370cm^{-1} representative of hBN. (e,f) AFM micrographs of CVD hBN grown on Sapphire using gaseous precursors from SMI. The roughness values shown are comparable to those grown by us using AB. (f,h) Raman spectrum of hBN on Sapphire from (e) and (g) respectively showing a weak but evident peak at ~1370cm^{-1} indicative of hBN.

We also attempted to grow hBN directly on CVD produced Gr/Cu substrates which were grown by SMI. Initially anneal tests we done where the Gr/Cu was taken to the growth temperatures under an inert atmosphere (Ar) at low pressures (~1torr) in order to verify that the Gr survives the heat cycle. Fig. 20 shows the results of these attempts. In Fig. 20a we shows an optical micrograph of as received Gr/Cu and in Fig. 20b we show the raman spectrum (red) compared to the raman spectrum of a bare oxidized Cu substrate (blue). Copper oxide is clearly present in the Gr/Cu as small peak at ~1280cm^{-1} confirms that the graphene has partially bonded to the CuOx species. The post-annealed substrate is shown in the optical micrograph of Fig. 20c where a clear roughening of the surface is evident. The Raman spectrum of the post annealed Gr/Cu is shown in Fig. 20d where no Graphene of CuOx peaks are present, thus proving that Gr/CU does not survive at the temperatures needed to grow hBN on it. For comparison we also annealed a Gr/SiC film at the same conditions and showed that these films did survive, thus, its only the Gr/Cu substrates that are not amenable to growth at high temperatures. We were unable to explain this phenomena and decided to focus on other projects at the time. Other groups have also attempted to hBN on Gr/Cu and have dealt with similar problems [61] where the Gr was etched away and hBN was grown instead. To the best of our knowledge no one has been able to grow hBN directly on Gr/Cu but Gr gown on hBN/Cu was readily demonsrated in 2011 [62] less than a year after hBN was first synthesized on it. We believe on of the main reasons is the necessity of H_2 to act as a co-catalyst to the formation of hBN however, the addition of H_2 to the gas stream will inevitably etch Gr/Cu.

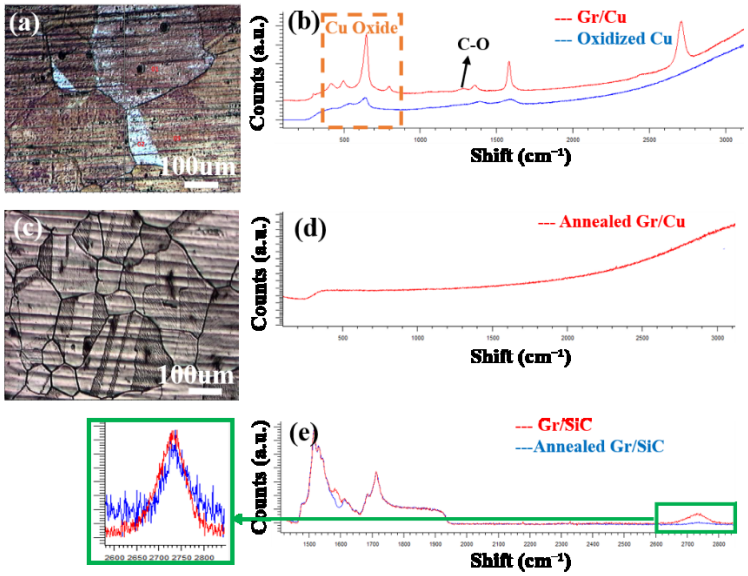

Figure 20 : (a) Optical micrograph of received CVD Gr/Cu substrate. (b) Raman spectrum of received Gr/Cu (red) and Oxidized bare Cu (blue). The Gr/Cu spectrum shows evidence of CuOx formation as well as C-O bonding. (c) optical micrograph of annealed Gr/Cu substrate showing signs of roughening. (d) Raman spectrum of annealed Gr/Cu where no Gr or CuOx peaks are present. (e) Raman spectrum of Gr/SiC (red) and annealed Gr/SiC (blue) where a Gr peak is evident in both. The left inset shows the Gr 2D peak at ~2750cm^{-1} before (red) and after the anneal process (blue).

References

[1] W. H. Balmain, "Remarks on the formation of boron and silicon compounds with nitrogen and certain metals," *Advanced Synthesis and Catalysis,* vol. 27, p. 422, 1842.

[2] M. Allendorf, "From bunsen to VLSI," *The elctrochemical society,* p. 1, 1998.

[3] K. Nakamura, "Preparation and properties of boron nitride films by metal organic chemical vapor depositoin," *Journal of the Electrochemical Society,* vol. 133, p. 1120, 1986.

[4] R. V. Gorbachev and a. et, "Hunting for monolayer boron nitride: optical and raman signatures," *Small,* vol. 7, p. 465, 2011.

[5] S. G. Shore and R. W. Parry, "The crystalline compound ammonia-borane," *Thermochimica Acta,* vol. 77, p. 6085, 1955.

[6] L. Song and a. et, "Large scale growth and characterization of atomic hexagonal boron nitride," *Nanoletters,* vol. 10, p. 3209, 2010.

[7] T. Q. P. Voung and a. et, "Deep ultraviolet emission in hexagonal boron nitride grown by high temperature molecular beam epitaxy," *2D materials,* vol. 4, p. 021023, 2017.

[8] D. Fu and X. Zhao, "Molecular beam epitaxy of highly crystalline monolayer molybdenum disulfide on hexagonal boron nitride," *Journal of the American Chemical Society,* vol. 139, p. 9392, 2017.

[9] Y.-J. Cho and A. Summerfield, "Hexagonal boron nitride tunnel barriers grown on graphie by high temperature molecular beam epitaxy," *Scientific Reports,* vol. 6, p. 34474, 2016.

[10] Y. Kubota, K. Watanabe, O. Tsuda and T. Taniguchi, "Deep Ultraviolet light emission hexagonal boron nitride syntehsized at atmospheric pressure," *Science,* vol. 317, p. 932, 2007.

[11] Y. Kubota, K. Watanabe and T. Taniguchi, "Synthesis of Cubic and Hexagonal Boron Nitride by using Ni solvent under high pressure," *Japanese journal of applied physics,* vol. 46, p. 311, 2007.

[12] J. Yin, J. Li, Y. Hang, J. Yu, G. Tai, X. Li, Z. Zhang and W. Guo, "Boron nitride nanostructures: fabrication, functionalization and applications," *Small,* vol. 12, p. 2942, 2016.

[13] Y. Stehle, H. M. Meyer and a. et , "Synthesis of hexagonal boron nitride monolayer: Control of nucleation and crystal morphology," *Chemistry of Materials,* vol. 27, p. 8041, 2015.

[14] S. Chatterjee and a. et, "Cemical vapor deposition of Boron Nitride Nanosheets on metallic substrates via decaborane ammonia reactions," *Chemistr of Materials,* vol. 23, p. 4414, 2011.

[15] K. Ahmed and a. et , "Metalorganic chemical vapor deposition of hexagonal boron nitride on (001) sapphire substrates for thermal neutron detectors," *Vacuum,* vol. 137, p. 81, 2017.

[16] K. H. Lee and a. et, "Large scale synthesis of high quality hexagonal boron nitride nanosheets for large area graphene electronics," *Nano Letters,* vol. 12, p. 714, 2012.

[17] C. F. Lane, "Amonia-Borane and related NBH compounds and materials," DOE, 2006.

[18] W. T. Klooster and et al, "Study of the dihydrogen bond including the crystal structure of BH3NH3 by nuetron difftraction," *Journal of the American Chemical Society,* vol. 121, p. 6337, 1999.

[19] J. Baumann and a. et , "Thermal decomposition of polymeric aminoborane under hydrogen release," *Thermochimica Acta,* vol. 430, p. 9, 2005.

[20] D. W. Himmelberger, "Hydrogen release from ammonia borane," Univeristy of Pennsylvania, 2010.

[21] F. Baitalow, J. Baumann, G. Wolf and a. et, "Thermal decomposition of BNH compounds investigated by using combined thermoanalytic methods," *Thermochimica Acta,* vol. 391, p. 159, 2002.

[22] D. Neiner, "Promotion of hydrogen release from ammonia borane with mechanically activated hexagonal boron nitride," *Journal of Physical Chemistry C,* vol. 113, p. 1098, 2009.

[23] H. Wang, Y. Zhao, Y. Xie, X. Ma and X. Zhang, "Recent progress in synthesis of two dimensional hexagonal boron nitride," *Journal of semiconductors,* vol. 38, pp. 031003-1, 2016.

[24] N. Mohajeri and a. et, "Ammonia-Borane complex for Hydrogen Storage," Florida solar energy center, 2007.

[25] J. C. Koepke and a. et, "Role of pressure in," *Chemistry of Materials,* vol. 28, p. 4169, 2016.

[26] D. M. Dobkin, Principles of Chemical Vapor Deposition, San Jose: WJ communications, 2006.

[27] R. Y. Tay and a. et, "A systematic study of the atmospheric pressure growth of large area hexagonal crystalline boron nitride film," *Journal of materials chemistry C,* vol. 2, p. 1650, 2014.

[28] W. Auwater and a. et , "Synthesis of on monolayer of hexagonal boron nitride on Ni (111) from B-Tricholoroborazine (ClBNH)3," *Chemistry of Materials,* vol. 16, p. 343, 2004.

[29] A. Stock and E. Pohland, "B3N2H6," *Boron Hydrides (Borwasserstoffe),* vol. 9, p. 2215, 1926.

[30] A. Nagashima and a. et , "Electronic dispersion relations of monolayer hexagonal boron nitride formed on the Ni(111) surface," *Physical Review B,* vol. 51, p. 4606, 1995.

[31] A. Catellani and a. et, "Electronic interlayer states in hexagonal boron nitride," *Physical Review B,* vol. 32, p. 6997, 1986.

[32] G. Cassabois, P. Valvin and B. Gil, "Hexagonal boron nitride is an indirect bandgap semiconductor," *Nature Physics,* vol. 10, p. 262, 2015.

[33] A. Nagashima and a. et, "Electronic structure of monolayer hexagonal boron nitride physisorbed on metal surfaces," *Physical Review Letters,* vol. 75, p. 3918, 1995.

[34] P. Sutter and a. et, "Chemical Vapor deposition and etching of high-quality monlayer hexagonal boron nitride," *ACS Nano,* vol. 9, p. 7303, 2011.

[35] P. R. Kidambi and a. et, "In situe observatoins during chemical vapor deposition of hexagonal boron nitride," *Chemistry of Materials,* vol. 26, p. 6380, 2014.

[36] Y. Shi and a. et, "Synthesis of few layer hexagonal boron nitride thin films by chemical vapor deposition," *Nanoletters,* vol. 10, p. 4134, 2010.

[37] L. Qin and a. et, "Catalyst free growth of mono and few atomic layer boron nitride sheets by chemical vapor deposition," *Nanotechnology,* vol. 22, p. 1, 2011.

[38] A. Ismach and a. et, "Toward the controlled synthesis of hexagonal boron nitride films," *ACS Nano,* vol. 6, p. 6378, 2012.

[39] S. Middleman, "The role of gas phase reactions in boron nitride growth by chemical vapor deposition," *Materials Science and Engineering,* vol. A163, p. 135, 1993.

[40] A. R. Jang and a. et, "Wafer scale and wrinkle free epitaxial growth of single orientated multilayer hexagonal boron nitride on Sapphire," *Nano Letters,* vol. 16, p. 3360, 2016.

[41] H. V. Keer, Principles of solid state, New Delhi: New Age International Publishers, 2005.

[42] J. B. Mullin, Single Crystal Growth I: Melt growth, New York: Plenum Press, 1991.

[43] Y. Kubota, K. Wantanabe, O. Tsuda and T. Taniguchi, "Deep ultraviolet ligh emitting hexagonal boron nitride synthesized at atmospheric pressure," *Science,* vol. 317, p. 932, 2007.

[44] T. Fujita and a. et, "Atomic origins of the high catalytic activity of nanoporous gold," *Nature Materials,* vol. 11, pp. 775-780, 2012.

[45] M. S. Bresnehan and a. et, "Integration of hexagonal boron nitride with quasi-freestanding epitaxial graphene," *ACS Nano,* vol. 6, p. 5234, 2012.

[46] N. Guo and a. et, "Controllable growth of trianbular hexagonal boron nitride domains on copper foils," *Nanotechnology,* vol. 23, p. 415605, 2012.

[47] A. C. Ferrari, S. Reich, A. Loiseau, R. Arenal, I. Bello and J. Robertson, "Resonant raman scaterring in cubic and hexagnoal boron nitride," *Physical Review B,* vol. 71, p. 205201, 2005.

[48] Y.-H. Lee and a. et, "Growth selectivity of hexagonal boron nitride layers on Ni with various crystal orientations," *RSC Advances,* vol. 2, p. 111, 2012.

[49] Z. Liu and a. et, "Ultrathin high temperature oxidation resistant coatings of hexagonal boron nitride," *Nature communications,* vol. 4, p. 2541, 2013.

[50] G. Lu and a. et, "Synthesis of large single crystal hexagonal boron nitride grains on Cu-Ni alloys," *Nature Communications,* vol. 6, p. 6160, 2014.

[51] S. Liu and a. et, "Atomistic insights into the nucleation and formation of hexagonal boron nitride on Nickel," *ACS Nano,* vol. 11, p. 3585, 2017.

[52] J. G. Diaz and a. et, "Hexagonal boron nitride on transition metal surfaces," *Theoretical Chemistry Accounts,* vol. 132, p. 1350, 2013.

[53] A. B. Preobrajenski and a. et, "Monolayer of hBN chemisorbed on Cu(111) and Ni(111): The role of the transition metal 3d states," *Elselvier,* vol. 582, p. 21, 2005.

[54] X. Li and a. et, "Large area synthesis of high quality and uniform graphene films on Cu foils," *Science,* vol. 324, p. 1312, 2010.

[55] L. Bornstein, Vol 5 "Phase equilibria, Crystallographic and Thermodynamic Data of Binary Alloys", New York: Springer, 1997.

[56] K. K. Kim and a. et , "Synthesis of monolayer hexagona boron nitride on Cu foil using chemical vapor deposition," *Nano Letters,* vol. 12, p. 161, 2012.

[57] J. Hwang, V. B. Shields, C. I. Thomas, S. Shivaraman, D. Hao, M. Kim, A. R. Woll, G. S. Tompa and M. G. Spencer, "Epitaxial growth of graphitic carbon on C-face SiC and sapphire by chemical vapor deposition," *Journal of Crystal Growth,* vol. 312, p. 3219, 2010.

[58] J. Hwang, M. Kim, D. Campbell, H. A. Alsalman, J. Y. Kwak, S. Shivaraman, A. R. Woll, A. K. Singh, R. G. Hennig, S. Gorantla, M. H. Rummeli and M. G. Spencer, "van der Waals epitaxial growth of graphene on sapphire by chemical vapor deposition without a metal catalyst," *ACS Nano,* vol. 7, p. 385, 2013.

[59] J. Pang, M. H. Rummeli and a. et, "Self-terminating confinment approach for large-area uniform monolayer graphene directly over SiOx/Si by chemical vapor deposition," *ACS Nano,* vol. 11, p. 1946, 2017.

[60] I. Markov, Crystal growth for beginners, 2003: World Scientific, New York.

[61] D. P. Goplan, R. M. Feenstra and a. et, "Formation of hexagonal boron nitride on graphene covered copper surfaces," *Arxiv,* p. 1, 2015.

[62] Z. Liu, P. Ajayan and a. et, "Direct growth of Graphene/Hexagonal Boron Nitride stacked layers," *NanoLetters,* vol. 11, p. 2032, 2011.

III. Optimization of hBN CVD Growth

As mentioned in the previous section, using solid AB as a precursor has many problems associated with it (See section 2.2.1.1), however with regards to optimizing the growth the main drawback is the inability to control the flow rate with a conventional MFC. This is mainly due to the exceedingly small partial pressure of gases that are released upon heating AB as well as the mixture of different species released. One can therefore, never be sure what the partial pressure of an individual species, such as Borazine, is when sublimating AB. Without this parameter it's impossible to model the deposition rate (i.e. growth rate) or obtain more detailed information such as the parameter space under which we obtain our crystal (typically called a CVD phase diagram) [1]. For this reason, most of the work in this chapter will focus on system temperature and *total* pressure as variables during growth. The effects that these have on the crystal growth will be inferred in terms of ex-situ analysis of the obtained films. This is not the ideal method to study

crystal growth. Typically, one can model the gas phase and surface reactions and obtain growth rates as a function of molar ratios of the gasses used as well as stoichiometry and even morphology of the grown films [2, 3]. Without a knowledge of the precursor flow rate this modeling is not possible.

A further note on the extent and applicability of modeling is due at this point. CVD in particular is an enormously complex method, it has many different components that require a vast breadth of knowledge in many different fields. For example, to study gas flow, kinetics is necessary and within this study one must often determine so called “molecular potentials” and “effective volumes” of the constituent gases in order to find binary diffusivities, this requires a good understanding of quantum statistics. The effects that temperature can have on a system require a good working knowledge of heat transport (which is essentially kinetics applied to thermally driven movement). Chemistry is required to study the catalytic effects different substrates will have on the gas stream and crystallography and thermodynamics is necessary to understand how your films will deposit. This is why models can only get us so far and the best we can hope for is that a good understanding of our model will enable us to set a certain parameter space for our growths, at worst, our model will lead us down the wrong path.

1 Temperature dependence of Ammonia Borane

As mentioned in section 2.2.1.2 Ammonia-Borane has quite a complicated thermolysis which complicates its usage as a solid precursor for hBN. As a summary we note that the sublimation of gaseous precursors from AB depends on the final temperature, the ramp rate, the surface area of the powder and the exposure to atmosphere. Of all of these dependencies the final target heating temperature was the critical parameter that modulated the growth of hBN on metal catalysts. In

this section we will discuss our efforts on understanding the relation between the heating temperature of AB and the growth of hBN on Cu foils.

As shown in Fig. 15 our initial growths were quite non-uniform and rough, this was due to the high temperature at which we were heating our AB (T~100°C). In order to study the gas evolution while heating our precursor we installed a pressure gauge at the outlet of the quartz container where the AB sits. Figure 21a shows the results of these measurements where the pressure is plotted as a function of time. For these measurements the AB was heated to 100°C at a ramp rate of ~5°C/min using the heat tape. We note that the power delivered to the heat tape was controlled with a variac power controller unit, thus, the heat rate is not well controlled since only the power delivered is being controlled. The heat rate would necessitate a temperature gauge at the quartz container to serve as the feedback parameter, but this was not done, instead the cited rate is more of an average value taken by the average time it took to reach the desired temperature (~20min. for 100°C). The three different plots shown in Fig. 21a (red, green and blue curves) correspond to the time that the AB was held at the target temperature of 100°C which was varied from 15min to 60min. No significant difference was seen with regards to holding time at the target temperature. From this plot we can see that there is a distinct peak pressure reached which decays slowly. This peak is reached within 8-11min of heating at 100°C. In order to understand this behavior, we relate this pressure dependence to prior studies done on AB with similar results shown in Fig. 21b-c. Fig. 21b is reproduced from ref. [4] and shows the results of measuring the gaseous content released during AB sublimation while heating to a target temperature of 90°C. The evolved gases where measure with mass spectrometry (shown in the Y-axis in units of amps) and the experiment lasted for >9hrs. From this figure we can see similar behavior to our results in Fig. 21a where it can de deduced that the majority of the gaseous content which is responsible for the pressure rise is H_2

with a smaller amount of MAB and an almost negligible amount of Borazine. This release of H_2 has been attribute to the thermal decomposition of AB into a polymer PAB as explained in section 2.2.1.2. Thus, we concluded that we were indeed melting our precursor at the temperatures used and the majority of the gas flow was H_2. This is the reason why our initial growths were non-uniform and irreproducible. To solve this problem, we decided to avoid the melting of our AB and heat it to lower temperatures, the specific temperature range used was chosen to be 60-75°C. The upper limit is explained in Fig. 21c (reproduce from Fig. 3 of ref. [5]) which shows differential scanning calorimetry measurements at various target temperatures. It can be seen that at 75°C it takes ~6hrs for the melting process to initiate which means we can safely grow for at least this time length at this temperature without inducing significant polymerization of the AB. The lower limit is taken from empirical results from our growths where at any temperature below 60°C we were unable to obtain hBN growth even after 10hrs. This is likely due to the negligible gas evolution at lower temperatures.

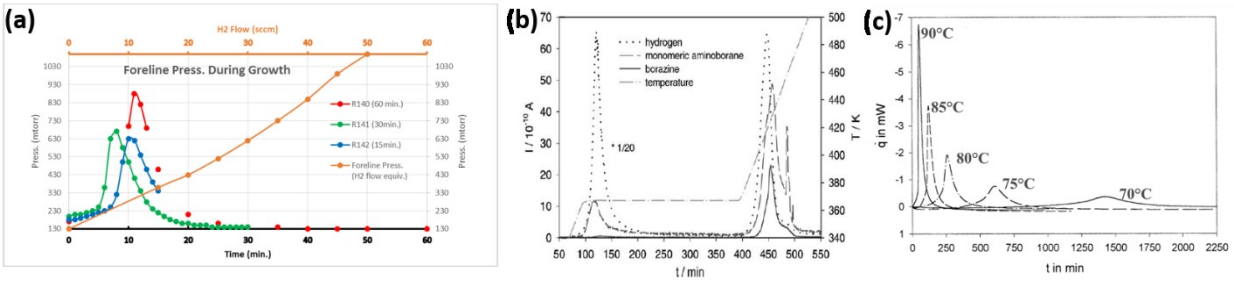

Figure 21 : (a) Pressure vs time plot taken from a pressure gauge placed at the outlet of the AB container. The target temperature for all plots was 100°C and the AB was held was held at this temperature for 60min (red) 30min (blue) and 15min (green). (b) Fig. 8 reproduced from ref. [4] where the AB was heated to 90°C at a controlled ramp rate of 5°C/min and held for ~9hrs. The evolved gases were measured with a mass spectrometer (Y-axis in amps) and their intensities are plotted as a function of time. (c) Fig. 3 reproduced from ref. [5] showing differential scanning calorimetry measurements of AB held at various constant temperatures for >24hrs. The y-axis shows the evolved heat measured in mW.

An unintended consequence of using this new lower temperature range is that our sublimed

gases produce pressures that are quite small, to the extent that it was not possible to use a Mass Flow Controller (MFC) to control the flow rate of our precursor as was done in prior experiments at 100°C (See Fig. 14). This is therefore the principal reason why a complete model for our growth system was not possible since in order to produce an Arrhenius plot it is necessary to know the growth rate which in turn is related to the precursor flow.

A typical growth result using the lower precursor temperatures is shown in Fig. 22. This growth was carried out under similar conditions to prior growths where the complete parameter description is shown in Fig. 22c. Fig. 22a shows an SEM micrograph of a coalesced hBN on Cu foil where we can see for the first-time grain boundaries and wrinkles present. A grain size of ~2um is achieved and apart from a coalesced film there is also presence of 3D triangular nuclei (see inset of Fig. 22a) which likely nucleate due to defect centers following an island growth mode. AS shown in the SEM several 3D nucleation lines are observed that closely follow the underlying grain boundaries. This is a typical result of 2D materials growth and crystal growth in general where grain boundaries and defects provide a smaller energetic barrier to the formation of stable 3D nuclei [6]. Fig. 22b shows a large area white light image of a film transferred to an oxidized silicon substrate with 90nm of SiO_2. Large areas where successfully transferred as shown in Fig. 22b, however, due to the nature of the wet transfer process (the details of which will be treated in Chapter 4) various holes are observed in the film. Nevertheless, the observance of grain boundaries, wrinkles, as well as a purplish color contrast under white light illumination all indicate that we have successfully grown a coalesced monolayer [7].

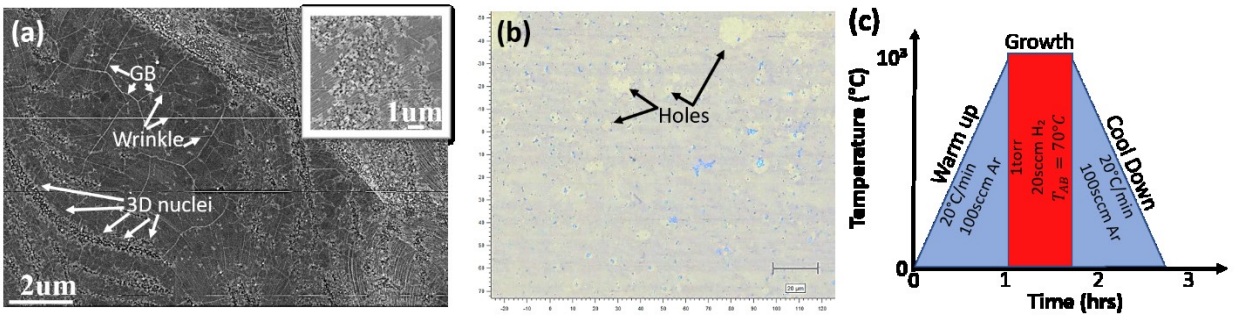

Figure 22 : (a) SEM micrograph of hBN grown on Cu foil with an AB temperature setting of 75°C. Grain boundaries, wrinkles and 3D nucleation are observed. The inset shows a magnified view of the triangular nucleation centers. (b) Large are white light image of an hBN film transferred to an SiO_2(90nm)/Si substrate. Various holes can be observed in the transferred monolayer which are induced during the transfer process. (c) Schematic depicting the growth process used to obtain the hBN on Cu films shown in (a).

2 Substrate optimization

In the prior section we dealt with the optimization of our precursor which lead, amongst other things, to the first successful synthesis of a coalesced hBN monolayer with our system. In this section we will discuss the optimization of the Cu foil in order to further increase grain size and get better control of our films.

2.1 PreAnneal

The as received Cu foils which are typically used for hBN growth are quite rough and have some non-negligible impurity content. An SEM image of a typical as received Cu Foil is shown in Fig. 23a where no distinct microstructure is visible and diagonal streak lines appear. These lines are due to the way in which the Cu foils are processed where thick sheets of cast Cu are pressed between two metal cylinders at high temperatures (~750°C) to produce thinner Cu foils. This process is known as a “Hot roll” process and is schematically depicted in Fig. 23c. A post-roll milling procedure can also be added to remove unwanted scales that form during the hot roll. The

direction of the lines observed in any Cu foil are indicative of the direction that the original cast Cu was rolled since they follow the small corrugations of the large metal rollers used. Since this is a high temperature process some degree of contamination can be introduced from the roller itself which is typically a metallic alloy. In Fig. 23b we present an EDX spectrum of the as received Cu foils where other than O_2 an Cu we also found evidence of Si and Al. Lastly, some oxidation of the Cu surface is evident by Raman measurements shown in Fig. 23d where a CuO_2 peak is found.

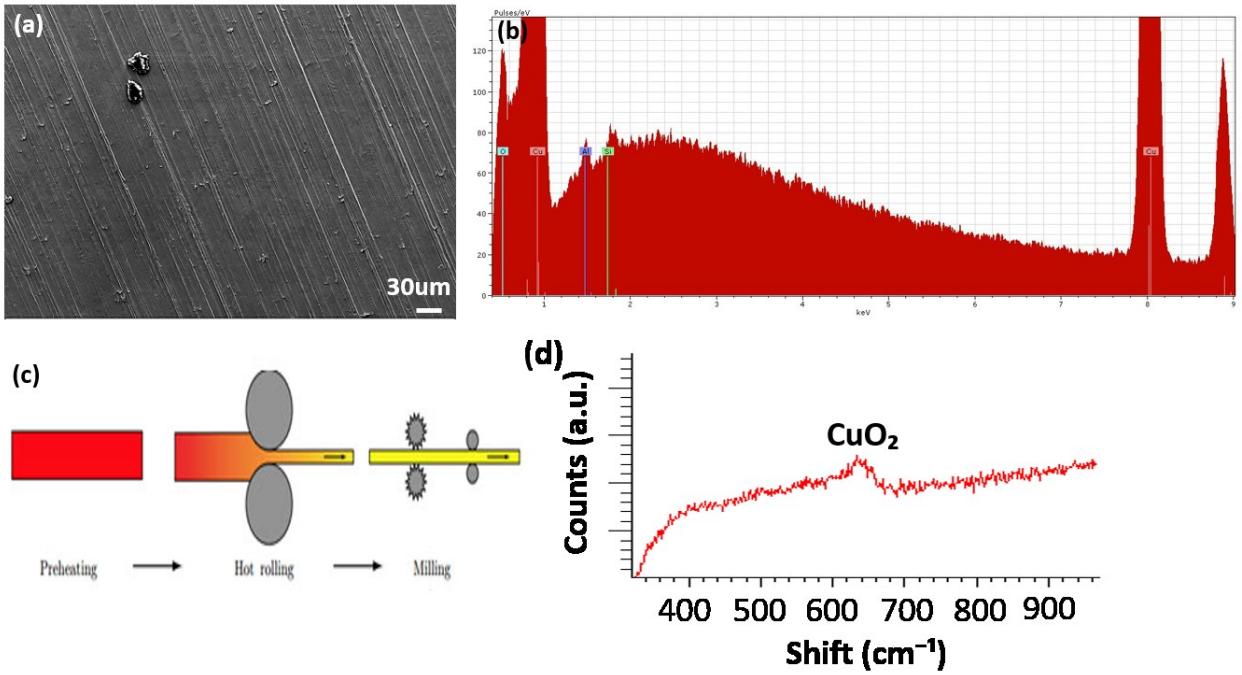

Figure 23 : (a) SEM micrograph of as received Cu foil. Rolling lines and surface residues can be observed. (b) EDX analysis of as received Cu foils where other than Cu and O_2 Si and Al are present. (c) Depiction of the Cu Hot Roll process [8] used to produce thin Cu foils from thicker cast Cu plates.

Thus, the as received Cu foils suffer from process related contaminants and are quite rough and non-uniform on the micro-scale. Our first attempt to obtain better quality Cu foils for hBN growth involved high temperature anneals in various atmospheres to exploit the well-known recrystallization of the surface [9, 10].

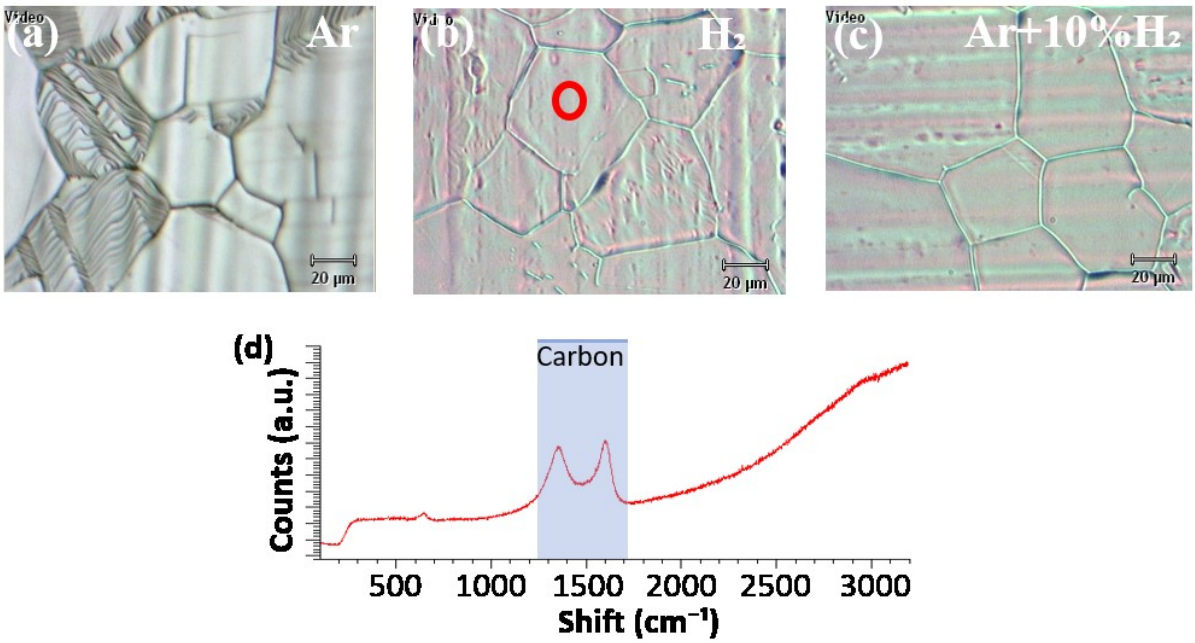

Figure 24 : (a) White light image of Cu foil after annealing at 1000°C in an (a) Ar atmosphere, (b) H_2 atmosphere, (c) Ar+10%H_2 atmosphere. (d) Raman spectrum taken at the red circle shown in (b). Carbonaceous peaks are clearly visible in this spectrum.

Show in Fig. 24 are the results of various annealing experiments done in different atmospheres at 1000°C with a total pressure of ~1torr. We can see that an Ar only atmosphere results in a roughening of certain Cu grains while a H_2 only atmosphere results in a smooth surface. We also found that in a H_2 only atmosphere there would always be evidence of carbonaceous peaks after annealing (see Fig 24d) which sometimes crystallized to form graphene. This is in agreement with previous work where it was found that annealing and growth atmosphere with high H_2 content promote the formation of graphene from the small amounts of C contamination present in all commercial Cu foils [11, 12]. Ultimately, it was found that a small amount of H_2 added to the gas stream is enough to obtain smooth surfaces free of carbonaceous residues after a high temperature anneal as shown in Fig. 23c.

The results shown in Fig. 24 are consistent with prior reported results on Cu foils used for Gr LPCVD growth [13, 14, 15, 16] where the roughening of the surface is attribute to step bunching of the Cu surface promoted by CuOx and impurity sites which prevent the diffusion of surface Cu atoms at the annealing temperatures used. Fig. 25 is reproduced from the work of Ibrahim et al. [13] where they show results very similar to ours (Fig. 25a-c) and they suggest that the role of H_2 during the annealing treatment is to remove the surface impurities and enable the stable recrystallization of the Cu at the high temperatures without the formation of steps, as shown in Fig. 25d. Furthermore, it has been suggested that H_2 uptake into the Cu sub-surface occurs at the annealing temperature of ~1000°C due to the non-negligible diffusion coefficient of H_2 in Cu at this temperatures ($3.3x10^{-4}cm^2/s$). Thus, it was found that large percentages of H_2 used during the annealing phase lead to H_2 outgassing from the Cu bulk during growth which has negative effects on the nucleation of the initial films. This is why we optimized our Cu annealing so as to use the smallest percentage of H_2 needed (10% as shown in Fig. 24c) In order to prevent roughening and enable cu grain growth. Finally, we note that our roughening (Fig. 24a) seems to be limited to only certain Cu grains. This has not been reported in the literature, however, we postulate that it may be due to the susceptibility of different Cu orientations to form oxide species due to the varying surface energies of a given Cu face.

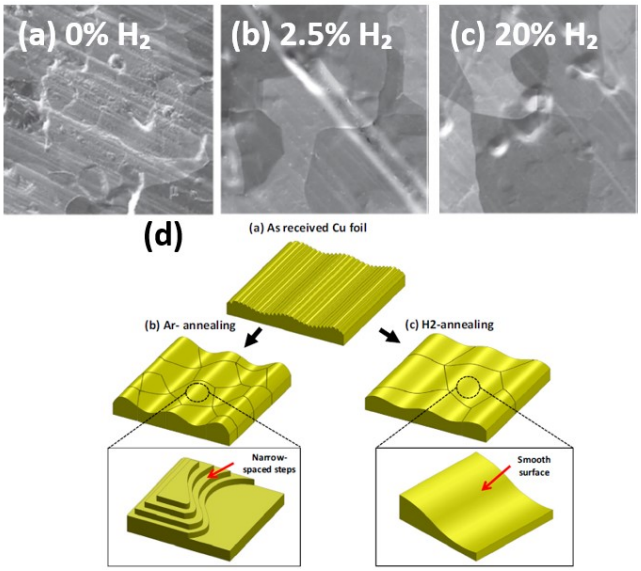

Figure 25 : SEM micrographs of annealed Cu foils taken from Ref. [13] under an (a) Ar only atmosphere (b) H_2 only atmosphere and (c) 10%H_2+Ar atmosphere. (d) The proposed surface reconstruction scheme of Cu when annealing in either Ar only atmospheres (left) or H_2 only (right) [13].

Once we determined the correct ratio of H_2/Ar gasses used during our Cu annealing the next step was to explore the temperature dependence of this anneal in order to attempt to further increase the size of the Cu grains. In Fig. 26 we show our results where it was found that the Cu grains grew from ~10's of um's at 1000°C to ~mm's at 1060°C, no significant change was seen at 1070°C as shown in Fig. 26c. These experiments were all carried out under 10%H_2+Ar atmospheres. Fig. 26d shows the process steps that we have until now for hBN growth.

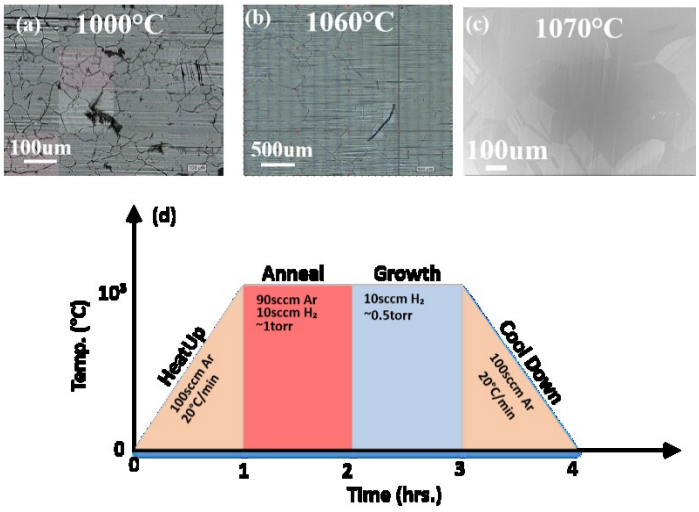

Figure 26 : Optical images of Cu foils annealed in a 10%H_2+Ar atmosphere at (a) 1000°C and (b) 1060°C. (c) SEM image of Cu foil annealed at 1070°C in a 10%H_2+Ar atmosphere. (d) Processing steps deduced until now for hBN growth.

2.2 Electropolishing

Proper annealing in a H_2 atmosphere lead to smoother Cu films, however, there was still a significant degree of contaminants at the surface which serve as unwanted nucleation centers. In order to eliminate these contaminants, we implemented an electropolishing technique which has been shown in other reports to reduce surface contaminants, decrease roughness and minimize Cu oxidation [7, 17, 18, 19]. Polishing has also been successfully applied to many other material systems [20, 21]. Our setup consisted of a solution of 2.17M H_3PO_4 + 9.67M Ethylene glycol in DI water as shown in Fig. 27a where a constant current source is maintained by an external sourcemeter (Keithley 2400). We note that a constant current is ket to avoid pitting since operating in constant voltage would lead to current variations over the Cu surface which in turn produce holes and pits. Furthermore, we heated our solution to ~65°C since it has been shown that the solution gives the best results at this temperature [19]. The working electrode is by definition the electropolished Cu foil (Anode) and for the counter electrode we used

a large piece of bulk cast Cu (Cathode) with a cross sectional area slightly larger than the anode. This larger cross sectional area is necessary to maintain the current flow as uniform as possible on the faces of the cathode and avoid pitting [22]. Our initial Cu foils were 100um thick purchased from Alfa Aeasar (No. 46365) and we cut them so that a cross sectional area of ~1"x3" would be polished. Using Faraday's Law of electrolysis (Eq. 2) we can roughly estimate the thickness of the final polished foil. Faraday's law says that the mass of removed particles from the surface is proportional to the charge passing through the surface where the proportionality constant is called the "Electrochemical Equivalent" (Eq) and is tabulated for most materials. For Cu we have Eq=3.3x10^{-4}(g/C)=3.7x10^{-2}(μm/C). Given a constant surface area and the density of our material (in our case $\rho_{Cu} = 8.96\ (g/cm^3)$) we can modify Farady's law to give the removed thickness per unit area instead, as shown in Eq. (3) below. Here, Eq is in (μm/C) and Q is in (C/cm^2), thus the etched thickness "th" will be in (μm/ cm^2).

$$m = Eq * I * t = Eq * Q \tag{2}$$

$$th = Eq * Q \tag{3}$$

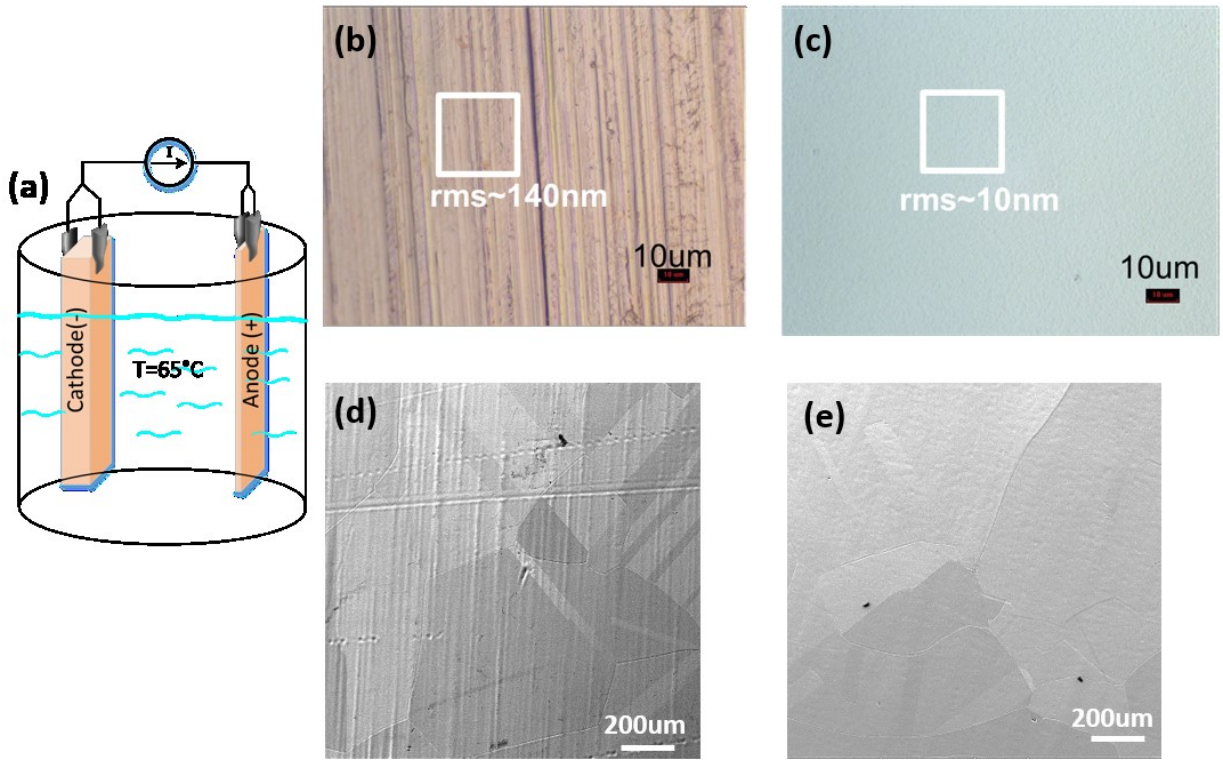

Figure 27 : (a) Depiction of our Electropolishing setup for Cu foils. Optical images of (b) as received Cu foil and (c) electropolished Cu foil. SEM images of (d) unpolished Cu foil after anneal treatment and (e) electropolished Cu foil after anneal treatment.

Given our measured current levels we estimate a total current density of ~350mA/cm^2 (i.e. 175mA/cm^2 per Cu face) which is equivalent to a total charge of 2.1x10^2(C/cm^2). Our etching experiments lasted for 5-10min. taking 10min. as the time we estimate a rough etched thickness of th~77.4(μm/ cm^2). Cu foils measured with a Vernier caliper gave thickness' of ~25um which would translate to a total etched thickness' of ~75um given our initial 100um foils.

Shown in Fig. 27b,c are optical images of as received Cu foils (Fig. 27b) and electropolished foils (Fig. 27c) where it is clear that the electropolished foil is much smoother and shows greater specular reflectance. We also used AFM to measure the rms roughness of these foils and show a reduction of atleast an order of magnitude. Figure 27d,e

shows SEM images of Cu foils that we annealed according to the procedure and parameters established in the previous section (See Fig. 26d). We find that both films exhibit good grain growth after annealing however the unpolished Cu foil maintains its striations due to its processing while the polished Cu foil presents a very smooth morphology with little evidence of surface defects. It has been proposed that during the Cu electropolishing process impurities present at the surface and sub-surface diffuse away from the Cu face leaving a pristine surface [22].

3 Wrapping Technique

In this chapter, up to now, we have optimized the precursor usage (Section 3.1) and the Cu foil (Section 3.2), now we show some empirical results that lead us to implement a completely new growth methodology for hBN.

3.1 Methodology

With the implementation of the high temperature anneal step to increase our Cu foil grain size we ran into some logistic problems. At the anneal temperature (~1060°C) Cu has a very high vapor pressure and the surface is very soft since we're approaching the melting point of 1085°C, thus, after the anneal was done, the Cu would stick to the Quartz tube sidewalls and it was difficult to retrieve the sample. In order to solve this problem, we designed a custom quartz boat that would enable us to easily push and pull our samples in and out of the hot zone of the furnace (See Fig. 28a). The boat was positioned by means of a small magnet attached to one end as shown in Figure 28a. The Cu foils were then wrapped around the flat end of the quartz boat and a small spacing was left between the Cu foil and the boat in order to prevent the foils from melting onto it during

the anneal stage.

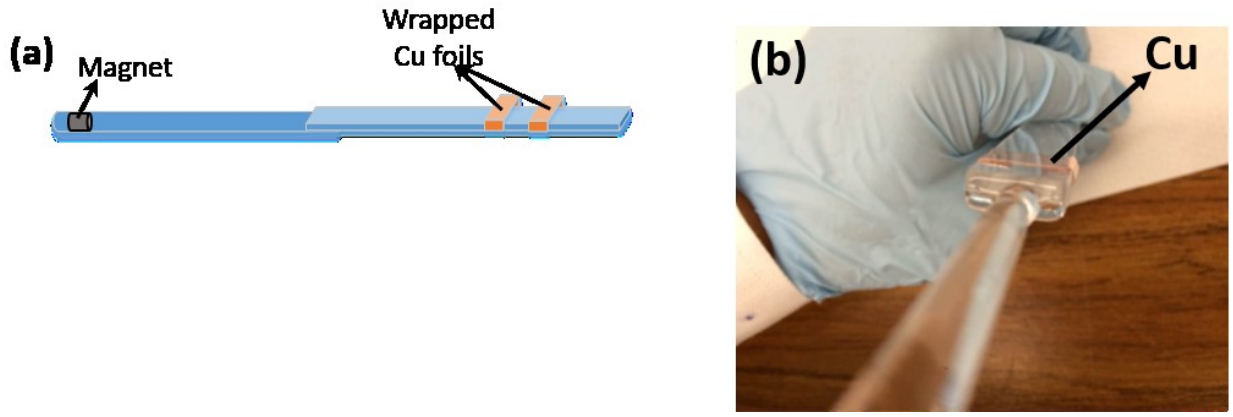

Figure 28 : (a) Depiction of new quartz boat design used to easily position the Cu foils inside and outside the hot zone of the furnace. (b) Picture of Cu foil wrapped around quartz boat.

With this new design we now had the option to analyze the growth on two sides of the Cu foils, the front side which is exposed to 0the CVD tube environment and the back side which has a narrow spacing between the Cu and the quartz boat as shown in fig. 29b. An SEM micrograph of the front side of the Cu foils for a typical 1hr growth following the procedure depicted in Fig. 26d is shown in Fig. 29a and an the backside is shown in Fig. 29b. We can see that the front side exhibits a completely coalesced film with many small white particles present while the back side shows uncoalesced triangular nuclei (for the first time!) with an average size of ~8um. Closer examination of the SEM in Fig. 29b shows that the nuclei are actually oriented differently across the grain boundary (accentuated with a purple line) and all nuclei within a grain boundary are well oriented with respect to each other. This is a clear sign of van der Waals epitaxy occurring in our growth where the weak bond between the Cu substrate and the hBN dictates the long-range alignment of the 2d film as opposed to the direction of flow suggested by Han et al. [23]. This has also been observed in the literature and it has been proposed that the Cu(111) direction has the strongest interaction since islands were seen to be consistently more uniformly aligned on these

grains [12].

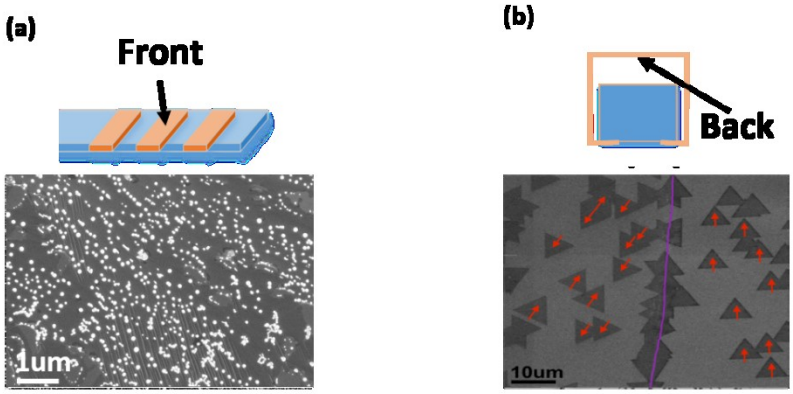

Figure 29 : (a) (Top)Schematic of Cu foil wrapped around quartz boat showing what is defined as the "Front" side. (Bottom) SEM of the front side of the hBN/Cu growth. (b) (Top) Schematic of Cu foil wrapped around quartz boat showing what is defined as the "Back" side. (Bottom) SEM of hBN/Cu foil grown on the back side where triangular nuclei can be seen to be aligned differently across different Cu grains.

The question remains however, why is the growth on the backside behaving so differently than that from the front? There seems to be two major difference on these faces, the back side shows a slower growth rate and a negligible presence of unwanted white particles. We note that the epitaxial relationship to the substrate could also be occurring on the front side, however, we were never able to limit the front side growth to the initial nucleation stages in order to confirm this. The lack of particles on the back side suggests that they may originate from our quartz tube since the back side doesn't see the large surface are of the tube which the front side is exposed to. In our system we have verified that these particles are indeed SiO_2 as shown in Fig. 30 where we intentionally grew for an extended period (>3hrs.) and analyzed the front surface via EDX. Fig. 30b shows an SEM of the front face of the foil which seem We note that the topic of particle contamination in CVD growth of both hBN and Gr has not been completely resolved with some

groups proposing it to be due to spherical agglomeration of the precursor while others agree with our analysis [12, 23, 16, 24]. With regards to the slower growth rate seen on the back side, this is due to the different gas dynamics that are present in the small confined region between the back Cu face and the quartz boat, we will discuss how these dynamics change the growth in the subsequent section.

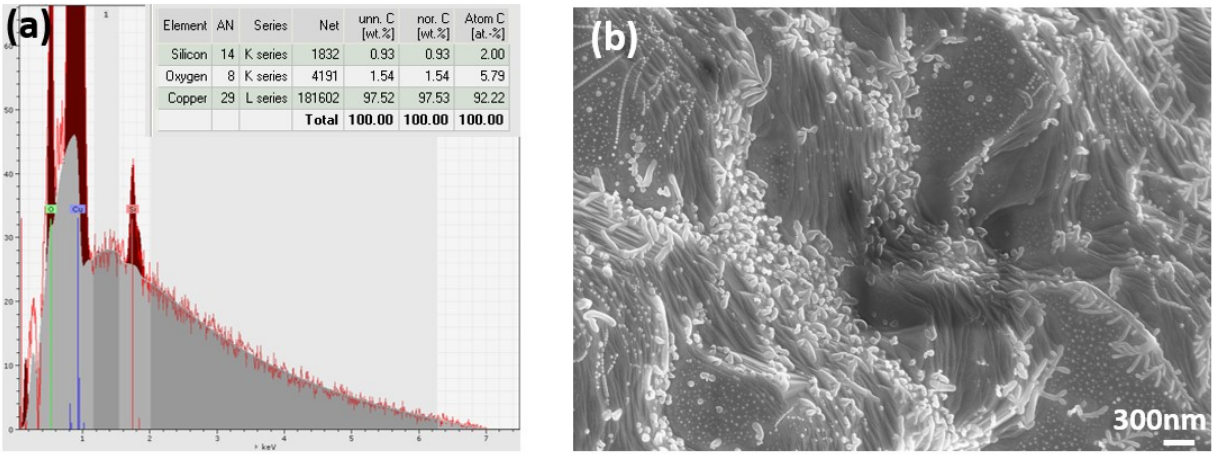

Figure 30 : (a) EDX analysis of the region shown in (b) where the elemental ratios of Si:O are ~1:2 indicative of the presence of SiO_2. (b) SEM image of the front side of a Cu foil after growing for >3hrs. Many small clusters of white particles can be observed which are proposed to be SiO_2 agglomerates coming from the quartz tube.

3.2 Diffusion dependent growth

In the previous section there was a drastic change in the hBN when observing the back face of the Cu foil. This face showed a reduced growth rate and much cleaner surfaces as compared to the front. These findings were similar to what was reported by Wang et al. [25] and were explained for Gr CVD by Cho et al. [26] in 2013. Our results on hBN reproduce their analysis quite closely where they found that when a narrow slit was formed between a Cu face and a quartz plate the Cu face was seen to be cleaner and the growth rate decreased. The reason this happens is that the boundary layer, which we neglected in the analysis of Appendix A, now limits the growth and

changes it from surface reaction rate limited to mass transport limited. We can see this by obtaining an estimate of the boundary layer thickness at the entrance of the slit (I've defined the "slit" to be the narrow opening between the Cu and the quartz boat) using:

$$\delta(x) = \sqrt{\frac{\upsilon * x}{U}} \sim 29.5\sqrt{x} \tag{4}$$

Where we've used the value of kinematic viscosity (υ) for H_2 ($1.824\text{x}10^{-1}(\text{m}^2/\text{s})$) found in Appendix A and the gas steam velocity of U~$2.1\text{x}10^{-4}$(m/s) also found in appendix A. If we assume a small distance of only x=0.1um the boundary layer thickness will be ~9.3mm, which is much large than the vertical slit opening (~1mm), thus it is safe to assume that the volume enclosed by the Cu face and the quartz boat is composed entirely of a stagnant gas. We note that our calculation for the boundary layer thickness is from Cho et al. where they obtained $\delta(x) = 0.52\sqrt{x}$. We believe the discrepancy lies in the kinematic viscosity which was not corrected for the effects of pressure by Cho et al. (i.e. lower pressure increases "υ"), correcting their equation for pressure (assuming ~1torr) their equation reads $\delta(x) = 14.8\sqrt{x}$, which is much closer to our result. Regardless, this change doesn't affect the conclusion that our precursor molecules now have to diffuse through a completely stagnant layer in order to reach the surface of the Cu, this effectively puts our growth in the mass flow limited regime, which, as discussed in Appendix A, is equivalent to growing in APCVD. This equivalence is seen in fig. 31. where we observed that near the slit entrance the films was at times nearly coalesced while at the exit it was almost always uncoalesced, these non-uniformities in the growth rate are exactly what one would expect for APCVD, or more in general, for mass transfer limited growth.

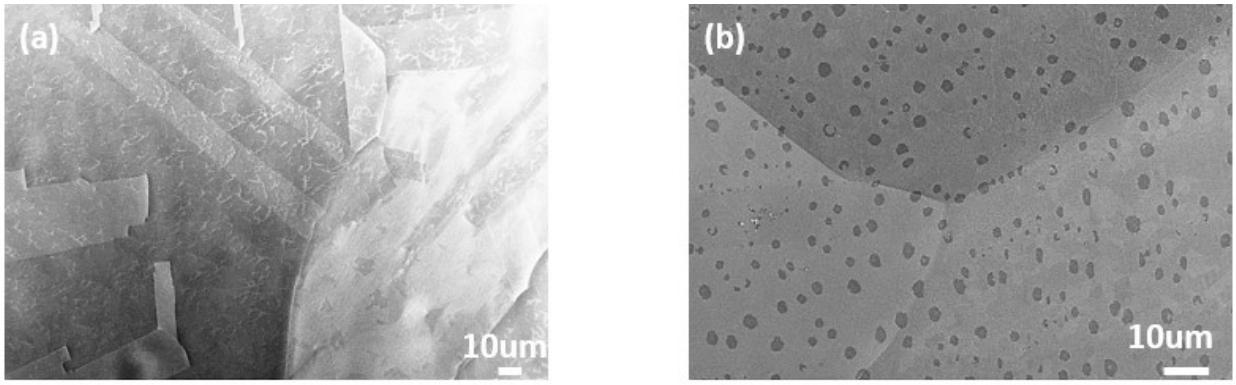

Figure 31 : (a) An SEM micrograph of hBN growth near slit entrance. A nearly coalesced film is observed. (b) An SEm micrograph of hBN growth near slit exit where an uncoalesced sparsely nucleated deposition is observed.

In order to better study the effects of the boundary layer we developed a method to controllably tune the slit gap. Shown in Fig. 32a is our new setup where a silicon wafer of a given thickness is placed between the Cu foil and the quartz boat to act as a spacer, the wafer is then carefully removed leaving a gap of the same size as the wafer thickness. We can now modulate the gap thickness by simple using silicon wafers of different thickness'. Shown in Fig. 32b is a plot of our measured nuclei size versus the gap size. We see that at gaps smaller than ~200um the domain size starts to sharply increase, this occurred in tandem with a decrease in nucleation density as well. In order to interpret these results we have calculated the Knudsen numbers as a function of gap size for a borazine molecule using Eqtn. A.9 and the dimensions of a borazine molecule. We've divided the plot in Fig. 32b into the respect regimes of Viscous, Knudsen and molecular flow. We see that the increase in domain size (decrease in nucleation density) occurs when we reach the molecular flow regime. Thus, if we would like to obtain large single crystal hBN films we would have to devise a mechanism to grow solely in the molecular flow regime. This is precisely what we did and is treated in the next section.

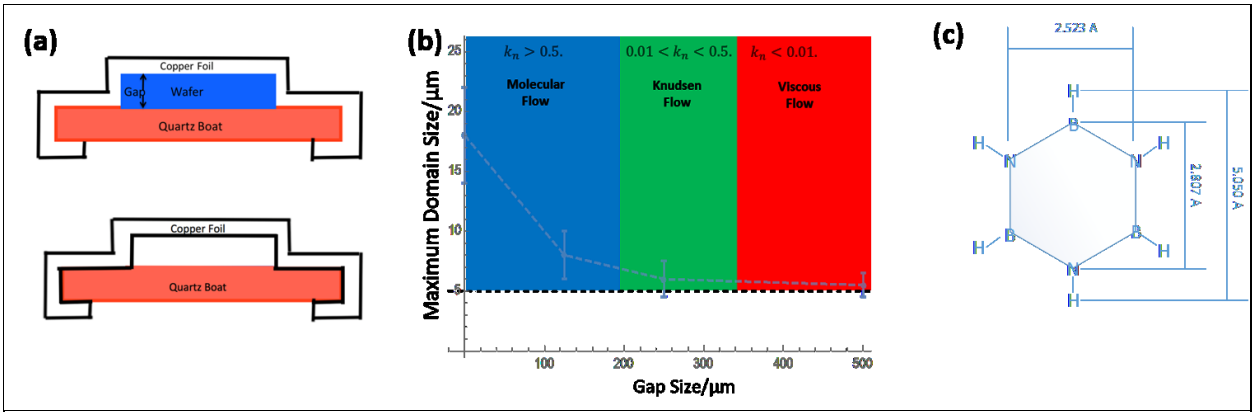

Figure 32 : (a) Depiction of new boat construct used to control the gap size. (b) Calculated nuclei size as a function of gap size within the different gaseous flow regimes. (c) Depiction of a borazine molecule showing the relevant dimensions used to estimate the diffusion length.

4 Cu Pocket Technique

As deduced in the prior section, growing in the molecular flow regime seems to have great improvements exhibiting reduced nucleation density and a decrease of contaminants (which could be responsible for the reduced nucleation density). The only adverse effect is that the smaller partial pressures of reactant molecules due to the combination of mass flow limited diffusion and molecular flow increase the growth times and lead to uneven growths along the length of the foil. In order to study all of these effects more closely we used the Cu pocket technique first developed by Li et al. [27] for Gr synthesis. Similar to their method, we folded an electro-polished Cu foil (following the procedure describe in 3.2.2) on all three sides and crimped the edges to form a pocket with openings that were sub-micron in height, as shown in Fig. 33e. The pocket was then placed in the center of the furnace as depicted in Fig. 33a. Shown in Fig. 33b,c are SEM images of two hBN growths done by using the wrapping technique (Fig. 33b) and the pocket technique (Fig. 33c), where the images correspond to the backside and interior respectively. There is a clear distinction in both nucleation density and nuclei size. We've estimated a factor of ~5.8 reduction in the nucleation density where the red circles (100um diameter) in each SEM image show the area

used for the calculations as well a doubling of the size of the nuclei (10um -> 20um triangles on a side). We note that although the growth using the pocket method yielded better results it also lasted six times longer.

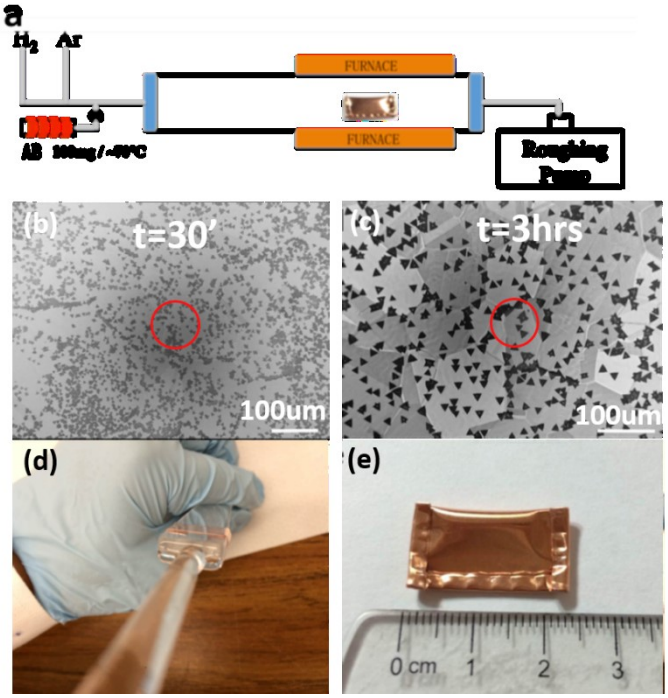

Figure 33 : (a) Depiction of CVD system showing the placement of the Cu pocket during growth. (b) SEM image of a typical growth using the wrapping method where the red circle depicts the area used for estimation of the nucleation density. (c) SEM image of a typical growth using the pocket method where the red circle depicts the area used for estimating the nucleation density. (d) Picture of the wrapping technique showing the Cu foil wrapped around a quartz boat. (e) Picture of a typical Cu pocket w/ crimped edges.

The reasons for the observed differences with both methods are varied and include the following:

(i) A cleaner gaseous environment within the Cu pocket. It has been in the literature as well as in our own studies that when Cu is exposed to the walls of the CVD tube its surface degrades significantly (See Figs. 29-30). Many explanations have been put forth to understand this one of which coincides with our own findings that SiO_2 deposits from the tube walls form in the gas phase and are placed on the Cu surface at

the high temperatures used [28]. Another reason used is that the tube itself is provides extraneous sources of unwanted species due to the accumulation of Cu and precursor layers on the tube walls overtime. These layers can delaminate and attach themselves to the Cu surface at the high temperatures and H_2 atmosphere used. This has led some groups to use an additional smaller diameter quartz tube within the larger tube to prevent these contaminants from reaching the surface of the catalyst [12]. Gas phase reactions can also not be ignored in the large volumes of the CVD tube. They can readily occur and form deposits which attach to the surface. These reactions are thought to be negligible inside the Cu pocket. Finally, any unwanted polymer species formed downstream, either from gas phase reactions or from the precursor sublimations, are unlikely to diffuse through the small lit opening of the crimped Cu pocket edges (~200-500nm [29]). Thus, it is safe to assume that the gaseous environment in the interior of the Cu pocket is composed solely of Borazine, H_2 and Cu.

(ii) A cleaner and smoother Cu surface in the interior of the Cu pocket. Researchers have theorized that this is due to the non-negligible Cu vapor pressure at the high growth temperatures of 1050°C (~5.5x10^{-5}torr [30]) which makes the sublimation and re-deposition of Cu an important factor in the surface recrystallization that takes place at these temperatures [26, 31, 32]. In the interior of the Cu pocket the evaporated Cu stagnates for longer times than in the exterior and suppress the sublimation leading to smaller re-depositions and better re-crystallization.

(iii) Different gas dynamics within the pocket. This is due to two main factors. First is the diffusion of the molecules through the narrow openings on the pocket edges. Since the openings are on the ~100's nm scale, they are much smaller than the diffusion length

of our Borazine or H_2 molecules at these temperature (~100's um) leaving us well within the molecular flow regime. In this regime, calculations have shown that the diffusivities of molecules decrease by ~4 orders of magnitude [29] within the slit leading to diminished precursor molecules reaching the interior of the pocket. It is well known from crystal growth theory that the nucleation rate is exponentially inversely proportional to the partial pressure of precursor molecules (i.e. the supersaturation "ΔG") [6, 33, 26]:

$$N^* = n_s \exp\left(-{}^{\Delta G}/_{kT}\right) * A_c * \upsilon \quad (5)$$

Where "N*" is the equilibrium concentration of critically sized nuclei, "n_s" is the density of nucleation sites, "A_c" is the critical surface area of a stable nuclei and "υ" is rate at which adatoms reach the edge of a growing stable nucleus. Thus, the nucleation rate in the pocket interior should be exponentially smaller than the exterior. The second factor that effects gas dynamics is the formation of a stagnant layer within the pocket which is expected to fill it completely. Thus, any diffusion to any interior surface of the pocket will be mass flow limited. This will in turn affect the availability of adatoms on the Cu surface that can impinge onto nuclei of critical radius A_c. In accordance with Eqtn. 5 "υ" is also decreased. These factors explain why the growth times increased and the nucleation rate decreased for the Cu pocket.

In summary, it seems that the reason why people have been successful with the Cu pocket or equivalent techniques [34] is that you are essentially using a brand new, thoroughly cleaned mini reactor (made of Cu) for each growth, this is why this technique is also sometimes called the Reactor in Reactor (RinR) technique. Since the growth of these 2D films has proven to be so sensitive to any parameters within the processing tube, as mentioned in (i) and (ii), the only way

to get clean reproducible growths (for the moment) is to use a brand new reactor each time.

Finally, we note that according to the last point (iii) we should have experienced an exponential decrease in the nucleation rate, however we only saw a decrease of about a factor of 6. In order to achieve this exponential, decrease we implemented other strategies which are discussed in the next sections.

5 H_2 Etching

It was found that despite the electro-polishing and high temperature annealing of our Cu foils, there were still a significant amount of defect sites that were contributing to the unexpected nucleation densities observed in Fig. 33c. In order to try to reduce the effects of these sites a H_2 etching step was incorporated into our growth process as shown in Fig. 34b. H_2 etching has been studied previously on CVD grown hBN films [35, 33] and its has been shown experimentally that the etching rate is highly sensitive to the partial pressure of H_2 where both the etching rate and etched morphologies change dramatically. Furthermore, the etching process was observed to be similar to a reverse Ostwald surface ripening process whereby the final state is a desorbed gas instead of a bound state [36, 37]. Using this model as a starting point it was shown that the limiting step in the etching process was the rate at which atoms would detach from an existing hBN nuclei and this detachment likely proceeds by formation of BH_x and NH_x intermediates [33]. This means that nuclei of different perimeters (i.e. different sizes) would etch at roughly the same rate since the limiting step is the detachment of atoms from the perimeter not the arrival rate of H_x species to it.

This is a crucial point since it means that one can, in theory, simply increase the H_2 supply during (or after) growth to etch smaller unwanted nucleation sites. This is exactly what we implemented experimentally by introducing an etching step which was done immediately after a

growth step and its purpose was to etch away any small nuclei that are formed at active defect sites in order to decrease nucleation density. Along with this etching step we also modified our growth by sequentially reducing the temperature of our precursor in order to reduce the feedstock of borazine to the Cu pocket and decrease the supersaturation. This sequential decrease in the supersaturation would in turn slowly grow the larger nuclei that haven't etched by the H_2 while minimizing the formation of new unwanted nuclei. This effect should be quite pronounced since the nucleation density it exponentially dependent to the superstation as shown ni Eq. (5). Thus, our new growth process has been modified to include a series steps, as shown in Fig. 34b, whereby the growth stages are followed by etching stages and in each growth stage the precursor supply is decreased. This unfortunately has the disadvantage of increasing our growth times from ~4hrs. to ~12-15hrs. making the yield quite inefficient, but it allowed us to explore the effects of etching on nucleation density. As shown in Fig. 34c,d we compare the growths using the two different process' via SEM. Fig. 34c shows the results of using the previous growth process while Fig. 34b shows the results of using the new method, it is clear form these figures that the etching steps have indeed suppressed the formation of smaller nucleation sites, however, the effective nucleation density is still comparable. Thus, H_2 etching enabled us to grow hBN nuclei that are uniform in size (w/o smaller nucleation sites) but still comparable in nucleation density. It was hypothesized that perhaps there was yet another unaccounted precursor supply that may be increasing the nucleation density. This supply was thought to be diffusion of N and B atoms through the Cu foil which would add another precursor source apart from the pocket' crimped edges. We explore this possibility in the following section.

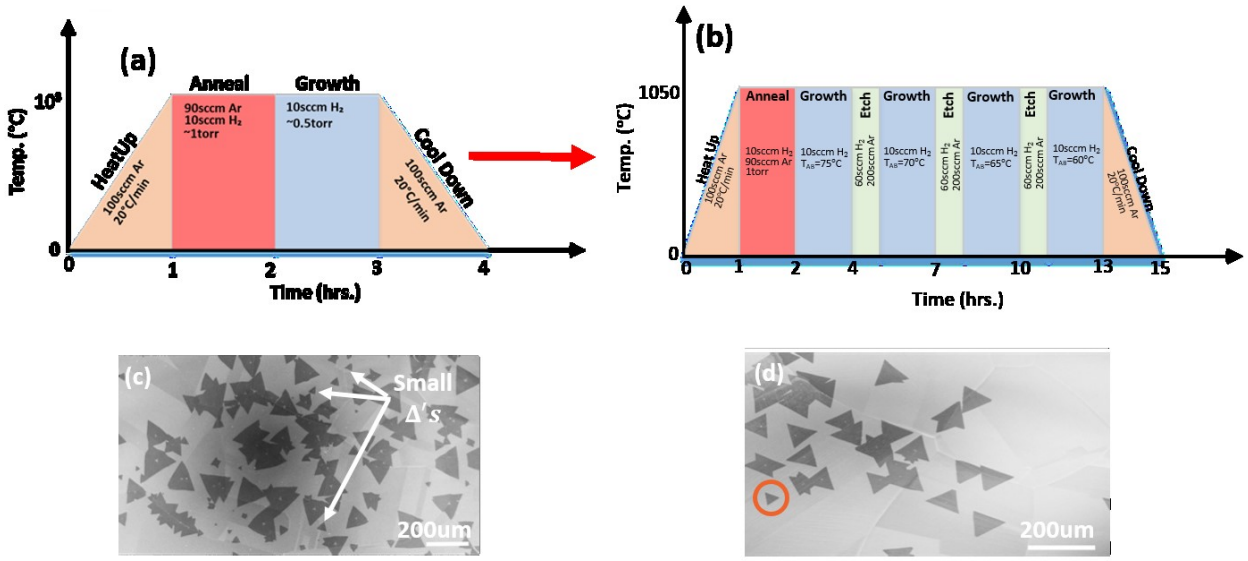

Figure 34 : (a) Previous growth process used for Cu pocket growths. (b) New growth process used in the Cu pocket methods. The inclusion of a H_2 etching step and its parameters are shown (green section) as well as the slight modification of the precursor temperature throughout all the growth steps (blue sections). (c) SEM image of interior of a Cu pocket showing hBN/Cufoil grown using the growth steps show in (a). Many smaller nuclei are observed. (d) SEM image of interior of a Cu pocket showing hBN/Cufoil grown using the growth steps show in (b). A steep decrease in the presence of the smaller nuclei is found and in this region only one potentially unetched nuclei is observed (red circle).

6 Role of Cu Thickness

It was shown in the previous section that the inclusion of H_2 etching step was efficient at reducing the presence of smaller nuclei, however, the nucleation rate itself didn't change much. This may be due to an additional source of B and N radicals that was unaccounted for. We considered the idea of B and N being supplied from the exterior of the Cu pocket by diffusion through the Cu bulk. The precise mechanism of diffusion was also considered due to the fact that the solubility of N in Cu was found to be null up to temperature of ~1400°C [38], however the case for the B-Cu system is quite different. Boron solubility in Cu is non-negligible and a binary eutectic phase diagram has been established for this system [39], as shown in Fig. 34a. The

solubility of B in Cu has been estimated to be ~0.3% at the eutectic temperature of 1013°C, thus, it is very likely that most growths of CVD hBN on Cu are done under B rich conditions, however, given that XPS measurements (shown in Chapter 4) have shown consistent stoichiometry of B:N ~1:1, it is assumed that this B uptake in the Cu does not affect the surface growth of 2D hBN. For our purposes, we have a reasonable argument for the supply of B species into the interior of the Cu pocket by mass transport through the Cu bulk, however, N transport is still negligible through the bulk at our growth temperature (~1050°C). Luckily, there have been previous studies that have already studied this phenomena of B and N diffusion in insoluble metals [40, 41, 42, 43, 44, 45, 46]. Satoru et al. [46] demonstrate that amorphous BN films deposited on an oxidized silicon substrate and coated with either Co or Ni would form crystalline hBN on the top metal surface by annealing in vacuum. They proposed that the only mechanism for the amorphous BN film to reach the top of the metal films is by grain boundary assisted diffusion of B and N through the metal. This would also be a valid argument for our supply of N through the Cu pocket and can be the reason for our lack of a small nucleation density.

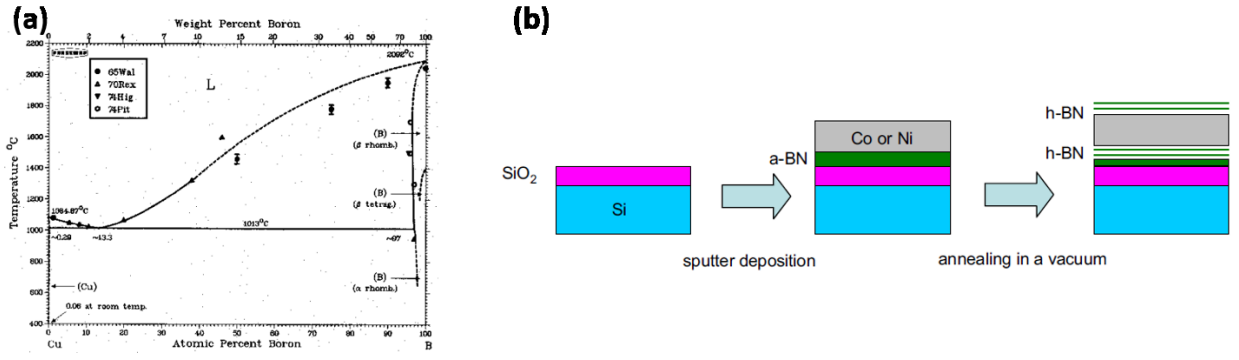

Figure 35 : (a) Binary eutectic phase diagram of the B-Cu system [39]. (b) Satori et al.'s method of growing hBN by precipitation of amorphous BN at elevated temperature through a metal (Co or Ni) layer [46].

We carried out experiments to test this theory by performing growth on Cu pockets made with foils of different thickness' (125um and 25um). For these experiments the pockets sides were

completely sealed by fusing the crimped openings on the edges at high temperatures during the anneal phase (~1060°C, shown in Fig. 36c), thus, leaving the only entry point of B and N species through the Cu foil from the outside atmosphere via grain boundary assisted mass transport. As shown in Fig. 36 d, for a Cu foil that was 125um thick we did not see any evidence of hBN nuclei formation in the interior, however for a 25um thick foil we found many individual small nuclei had form in the interior. Thus, similar to Satori et al., we were getting additional species through the thin Cu pocket that were contributing to the nucleation. We propose that species likely diffuse in the time it takes the outer Cu face to be completely covered with hBN as shown in Fig. 36a,b.

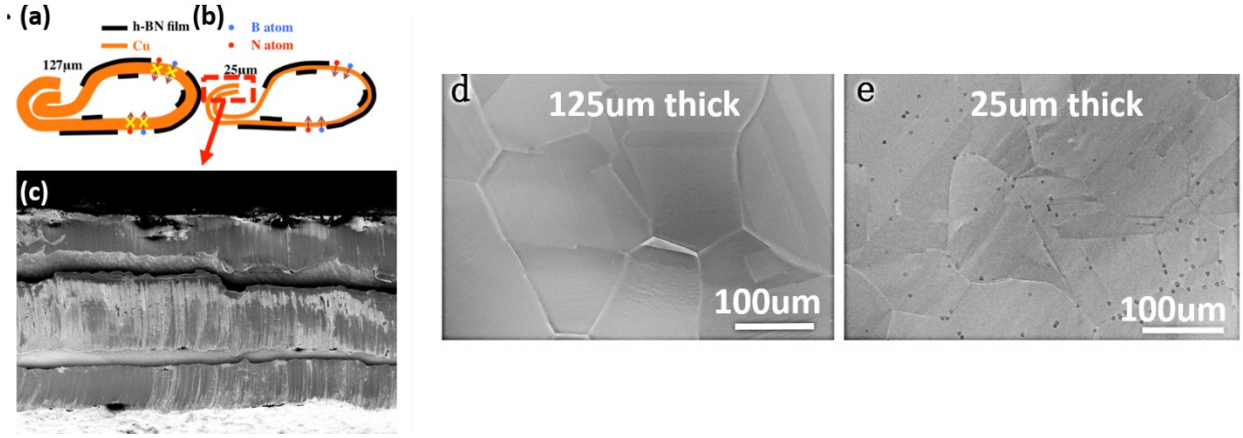

Figure 36 : Schematic of proposed diffusion mechanism through the Cu foil for a 125um thick foil (a) and a 25um thick foil (b). (c) Cross-sectional SEM of a fused Cu slit after the high temperature anneal. SEM micrographs of growth performed on completely sealed Cu foils of 125um thick (d) and 25um thick (e).

We summarize all the methodologies and changes incorporated to our hBN growth system up to this point:

Precursor:

(i) The temperature was lowered from 100°C to the range between 60-75°C.

(ii) The ramp rate to reach the final goal temperature was made as high as possible.

Catalyst:

(i) We've chosen Cu instead of Ni due to the uneven catalytic performance of polycrystalline Ni foils.

(ii) Annealing at high temperatures under small H_2 partial pressures alleviates surface contaminants and induces Cu grain growth.

(iii) We electropolish our foils prior to loading them into the system in order to further planarize the Cu surface and remove contaminants.

(iv) We use a thick Cu pocket technique made out of 125um thick Cu foil.

Growth Process:

(i) We operate in the LPCVD regime to obtain surface reaction limited uniform growths.

(ii) We use a high temperature growth (~1050°C) to get better crystal quality.

(iii) We incorporate a multistage growth process with sequential growth and H_2 etching steps.

Following all the above steps in our growth process we were finally able to obtain an exponential decrease in our nucleation density reaching values up to a single nucleus per mm^2 (See Fig. 37h). We also show that the size of corresponding single crystal regions increased with time as shown in Fig. 37d-g. Finally, were able to show that single crystal grains of hBN up to 0.3mm are obtainable (See Fig. 37i), which are comparable to the mm sized grains obtained for Gr with similar methods [27, 29].

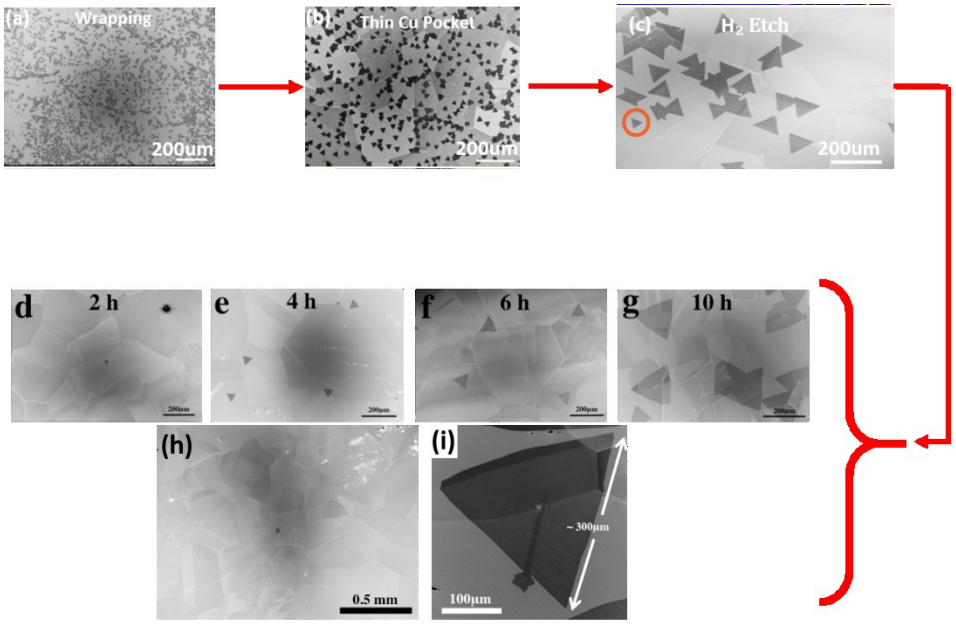

Figure 37 : (a) SEM micrographs of the evolution of our hBN films on Cu foils by applying various methods such as: Wrapping technique (a), thin Cu pockets (b), H_2 etching (c). (d-g) SEM micrographs of the size evolution (as a function of growth time) of hBN nuclei by applying all the techniques summarized in this section. (h) SEM micrograph of our lowest obtained nucleation density showing a single nucleus in an area of ~1mm^2. (i) SEM image of the largest obtained hBN single crystal grain in this study showing a side length of ~300um.

References

[1] P. M. Martin, Handbook of deposition technologies for films and coatings, New York: Elsevier, 2010.

[2] S. Middleman, "The role of gas phase reactions in boron nitride growth by chemical vapor deposition," *Materials Science and Engineering,* vol. A163, p. 135, 1993.

[3] D. M. Dobkin, Principles of Chemical Vapor Deposition, San Jose: WJ communications, 2006.

[4] F. Baitalow, J. Baumann, G. Wolf and a. et, "Thermal decomposition of BNH compounds investigated by using combined thermoanalytic methods," *Thermochimica Acta,* vol. 391, p. 159, 2002.

[5] G. Wolf, J. Baumann and F. P. Hoffmann, "Calorimetric process monitoring of thermal decomposition of B-N-H compounds," *Thermochimica Acta,* vol. 343, pp. 19-25, 2000.

[6] I. Markov, Crystal growth for beginners, 2003: World Scientific, New York.

[7] J. Yin, J. Li, Y. Hang, J. Yu, G. Tai, X. Li, Z. Zhang and W. Guo, "Boron nitride nanostructures: fabrication, functionalization and applications," *Small,* vol. 12, p. 2942, 2016.

[8] Total Materia, "Copper Foil Manufacturing," Toal Material, [Online]. Available: http://www.totalmateria.com/page.aspx?ID=CheckArticle&site=ktn&NM=352. [Accessed 3 November 2017].

[9] Wikipedia, "Recrystallization," [Online]. Available: https://en.wikipedia.org/wiki/Recrystallization_(metallurgy). [Accessed 5 November 2017].

[10] A. M. Torres and a. et, "Effect of annealing conditions on the grain size of nanoscrystalline copper thin films," *Materials Science Forum,* vol. 587, p. 483.

[11] A. J. Sturdwick and a. et, "Chemical vapor deposition of high quality graphene films from carbon dioxide atmospheres," *ACS Nano,* vol. 9, p. 31, 2015.

[12] G. E. Wood and a. et, "van der Waals epitaxy of monolayer hexagonal boron nitride on copper foil: growth, crystallography and electronic band structure," *2D materials,* vol. 2, p. 025003, 2015.

[13] A. Ibrahim and a. et, "Effects of annealing on copper subsrtate surface morphology and graphene growth by chemical vapor deposition," *Carbon,* vol. 94, p. 369, 2015.

[14] Y. Celik and a. et, "Relationship between heating atmosphere and copper foil impurities during graphene growth vial low pressure chemical vapor deposition," *Carbon,* vol. 109, p. 529, 2016.

[15] D. H. Jung and a. et, "Effects of hydrogen partial pressure in the annealing process on graphene growth," *The Journal of Physical Chemistry C,* vol. 118, p. 3574, 2014.

[16] L. Gan and a. et, "Turning off hydrogen to realize the seeded growth of subcentimeter single crystal graphene grains on copper," *ACS Nano,* vol. 7, p. 9480, 2013.

[17] R. Yingjie and a. et, "Growth of large single crystalline two dimensional boron nitride hexagons on electropolished copper," *NanoLetters,* vol. 14, p. 839, 2014.

[18] Y. Stehle, H. M. Meyer and a. et , "Synthesis of hexagonal boron nitride monolayer: Control of nucleation and crystal morphology," *Chemistry of Materials,* vol. 27, p. 8041, 2015.

[19] . G. D. Kwon and a. et, "Controlled electropolishing of copper foils at elevated temperatures," *Applied Surface Science,* vol. 307, p. 731, 2014.

[20] Wikipedia, "Electropolishing," [Online]. Available: https://en.wikipedia.org/wiki/Electropolishing. [Accessed 9 November 2017].

[21] Discovery, "Polishing a turd," Discovery, [Online]. Available: https://www.discovery.com/tv-shows/mythbusters/videos/polishing-a-turd-minimyth. [Accessed 9 November 2017].

[22] S. M. Kim and a. et, "The effect of copper pre-cleaning on graphene synthesis," *Nanotechnology,* vol. 24, p. 365602, 2013.

[23] J. Han and a. et, "Synthesis of wafer scale hexagonal boron nitride monolyaers free of aminoborane nanoparticles by chemical vapor deposition," *Nanotechnology,* vol. 25, p. 145604, 2014.

[24] D. P. Goplan, R. M. Feenstra and a. et, "Formation of hexagonal boron nitride on graphene covered copper surfaces," *Arxiv,* p. 1, 2015.

[25] L. Wang and a. et, "Monolayer hexagonal boron nitride films with large domain size and clean interface for enhancing the mobility of graphene based field effect transistors," *Advanced Materials,* vol. 26, p. 1559, 2014.

[26] S.-Y. Cho and a. et, "Gas transport controlled synthesis of graphene by employing a micrometer scale gap jig," *RSC Advances,* vol. 3, p. 26376, 2013.

[27] X. Li and a. et, "Large are graphene single crystals grown by low pressure chemical vapor deposition of methane on copper," *Journal of the American Chemical Society,* vol. 133, p. 2816, 2011.

[28] N. Lissi and a. et, "Contamination free graphene by chemical vapor dposition in quartz furnaces," *Scientific Reports,* vol. 7, p. 9927, 2017.

[29] Y. Hao and a. et, "Oxygxen activated growth and bandgap tunability of large single crystal bilayer graphene," *Nature Nanotechnology,* vol. 11, p. 426, 2015.

[30] H. N. Hersh, "The vapor pressure of copper," *Journal of the American Chemical Society,* vol. 75, p. 1529, 1953.

[31] L. Tao and a. et, "Uniform wafer scale chemical vapor deposition of graphene on evaporated Cu (111) film with quality comparable to exfoliated monolayer," *The Journal of Physical Chemistry C,* vol. 116, p. 24068, 2012.

[32] P. Y. Teng and a. et, "Remote catalyzation for direct formation of graphene layers on oxides," *NanoLetters,* vol. 12, p. 1379, 2012.

[33] P. Sutter and a. et, "Chemical Vapor deposition and etching of high-quality monlayer hexagonal boron nitride," *ACS Nano,* vol. 9, p. 7303, 2011.

[34] J. Yin and a. et, "Large single crystal hexagonal boron nitride monolayer domains with controlled morphology and straight merging boundaries," *Small,* vol. 11, p. 4497, 2015.

[35] L. Wang and a. et, "Growth and etching of monolayer hexagonal boron nitride," *Advanced Materials,* vol. 27, p. 4858, 2015.

[36] M. Giesen and a. et, "Step and island dynamics at solid-vacuum and solid-liquid interfaces," *Progress in Surface Science,* vol. 68, p. 1, 2001.

[37] P. A. Thiel and a. et, "Adsorbate enhanced transport of metals on metal surfaces: Oxygen and Sulfur on coinage metals," *Journal of vacuum science technology,* vol. 28, p. 1285, 2010.

[38] B. Landolt, O. Madelung and B. Predel, "Cr-Cs -- Cu-Zr," in *Group IV Physical Chemistry 5D*, Springer Materials, 1994.

[39] B. Landolt, O. Madelung and B. Predel, "B-Ba -- C-Zr," in *Group IV Physical Chemistry 5B*, Springer Materials, 1992.

[40] R. H. Stulen and a. et, "Surface segregration of boron in nitroden strengthened stainless steel," *Journal of Vacuum Science Technology,* vol. 16, p. 940, 1979.

[41] K. Yoshihara, M. Tosa and a. et, "Surface precipitation of boron nitride on the surface of type 304 stainless steels doped with nitrogen, boron and cerium," *Journal of Vacuum Science and Technology,* vol. 3, p. 1804, 1985.

[42] D. Fujita and a. et, "Characterization and thermal desorption specotroscopy study on a new, low outgassing material surface for impoved ultrahigh vacuum uses," *Journal of Vacuum Science and Technology,* vol. 6, p. 230, 1988.

[43] D. Fujita and T. Homma, "A new model of surface precipitation of boron nitride on an austentic stainless steel and its outgasing nature," *Thin Solid Films,* vol. 181, p. 267, 1989.

[44] Y. Minami and a. et, "Effects os some elements and temperature on the surface segregation of boron nitride," *Journal of Vacuum Science and Technology,* vol. 7, p. 1585, 1989.

[45] C. A. Long and a. et, "The formation of boron nitride on Fe-37 ni alloy," *Applied Surface Science,* vol. 5, p. 722, 1992.

[46] S. Satoru and a. et, "Growth ot atomically thin hexagonal boron nitride films by diffusion through a metal film and precipitation," *Journal of Physics D,* vol. 45, p. 385304, 2012.

IV. Characterization of Single Crystal hBN

This chapter is intended to be a short survey of the characterization methods and results of the grown hBN films in the previous section. The detailed characterization results were not presented in Chapter 3 in order to maintain a linear, cohesive and understandable reading of the evolution and optimization of our growth, they will now be presented.

1 Transfer

There are two main approaches to transfer 2D materials from their parent substrates: (i) Dry transfer and (ii) Wet transfer. There have also been reports of electrochemical methods [1], hwoever they are recent and require quite a bit of optimization. Dry transfer techniques have shown to yield layers with low residue and larghe area, however, for monolayers, these techniques have reportedly suffered from tears and require time consuming optimizations in order to yield clean layers with no mechanical damage [2, 3]. In order to minimize the time spent on the transfer optimization we choose to use the wet transfer technique since it requires little optimization and high yields with practically no tears [3, 4, 5]. This comes, however, at the cost of carbonaceous residues on the surface which are quite difficult to remove [6].

The transfer process is shown schematically in Fig.38a where we initially spin a layer of PMMA (4% dissolved in solvent) on the surface we intend to transfer. The stack is then turned around and the backside is etched in O_2 plasma for 3.5min in order remove the hBN that has grown on this side. This step is necessary so that the etching of the Cu substrate in the following step proceeds uniformly, if there is hBN on the backside the Cu etchant will not penetrate through this layer and the cu will be unevenly etched. We have also observed that the back (unwanted) layer gets transferred along with the top layer if it's removed. Following the backside etching the PMMA/Cu/hBN stack is then floated in Cu etchant (CE-100 from Transene) for ~12hrs to ensure the complete removal of the Cu substrate. The floating PMMA/hBN stack is then transferred

various times (3-4) to Di-H_2O containers in order to remove any Cu etchant residues on the back side and left to float for ~6hrs. The sample is then scooped onto the target substrate and left to dry in a desiccator for ~12hrs. The PMMA/hBN/substrate stack is then dipped in 1165 solvent for 12hrs to remove the PMMA layer. Finally, the sample hBN/substrate is annealed at high temperatures (discussed in the next section) in order to completely remove any residue from the PMMA. Figure 38b shows an example of a transferred film with this process where unfortunately some holes have been created. We were not able to completely optimize the process to minimize films damage.

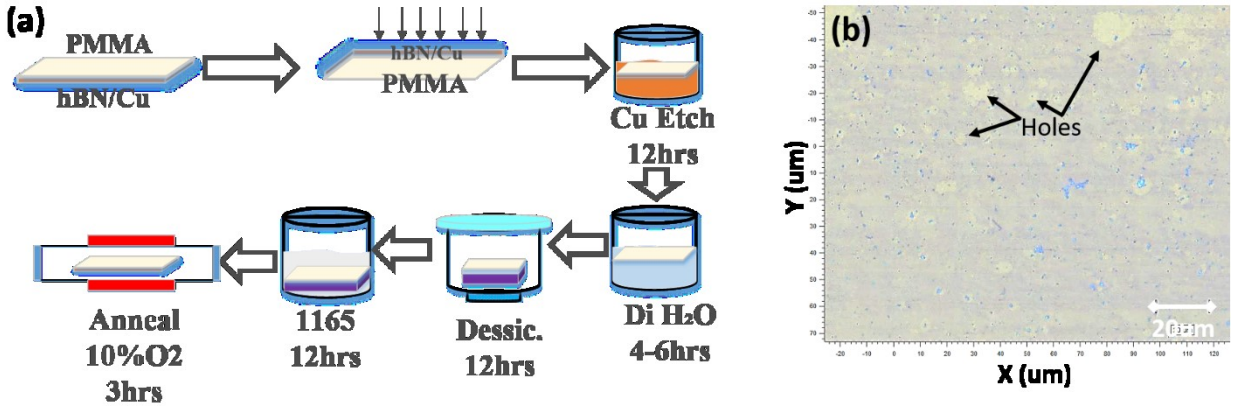

Figure 38

: (a) Schematic depiction of the transfer process used for CVD grown hBN on Cu foils. (b) Large area optical image of an hBN film transferred to an SiO_2/Si substrate. Holes induced during the transfer process are shown.

2 Annealing

In order to completely remove residues that are inevitably present in the hBN after transfer we implemented an annealing technique similar to that reported by Garcia et al. [6] where the transferred film is annealed in an O_2 atmosphere. Our detailed procedure consisted of annealing the transferred film in an environment of 10%O_2 +Ar at positive pressures (>1atm) under a flow of 3slpm at varying temperatures for 3hrs. Figure 39a shows Raman spectra of anneals performed

at both 500 (red) and 800°C (blue) under these conditions compared to the initial transferred spectrum (green) as well as a bare SiO_2 substrate (black). It is evident that a large background exists at wavenumbers above ~500cm^{-1}, this background has been attributed to carbonaceous residues left over by the wet transfer process [6]. The spectra of the annealed films show no such background pointing towards a removal of these residues, closer inspection shows that the 500°C anneal still presents a positively sloped background above ~1800cm^{-1} while the 800°C anneal shows no such trend and is almost indistinguishable from the bare SiO_2. The E_{2g} Raman mode corresponding to hBN at ~1370cm^{-1} [7] was not found in these characterizations due to the very weak signal that a monolayer of hBN presents [8] (more details to come in the following sections). In order to verisy that the transferred monolayers were not etched at 800C under the O_2 atmosphere XPS was performed before and after the anneal and is shown in Fig. 39c. No signs of oxidation was found [9, 10, 11, 12] and the stoichiometry was maintain at B:N=1:1 indicating that no damage to the hBN was induced. This is expected since it has been demonstrated that hBN monolayers can survive up to ~840°C in air (~21% O_2) without degrading [13].

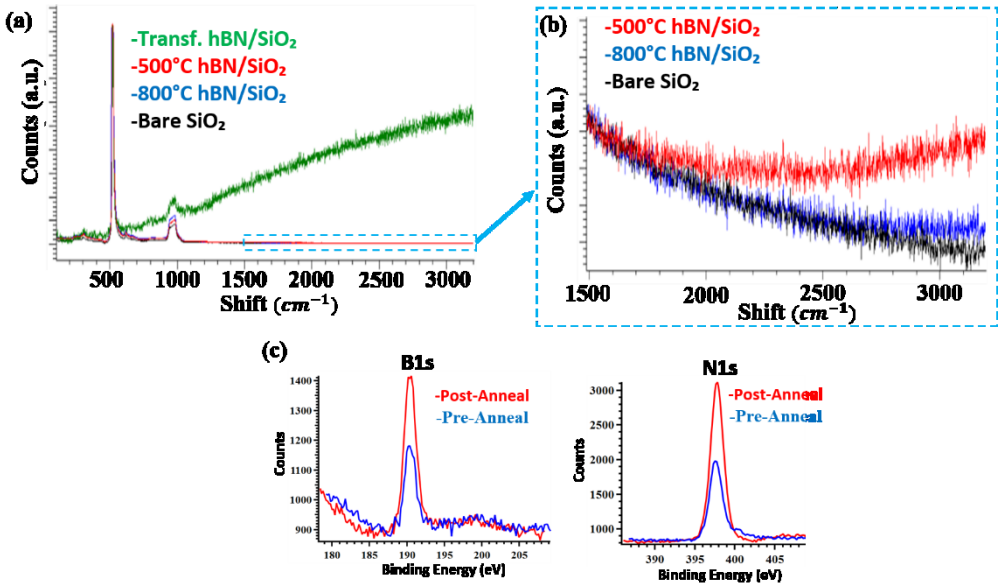

Figure 39

: (a) Raman spectrum of freshly transferred hBN film on SiO_2 (green), annealed at 500°C (red), annealed at 800°C (blue) and bare SiO_2 (black). (b) Magnified view of the spectra in (a) for the wavenumbers above 1500cm^{-1} showing evidence of residue in the 500°C anneal due to the positively sloped background. (c) XPS spectra of the Boron and Nitrogen 1s orbital peaks before and after the 800°C anneal showing no signs of oxidation in the hBN flim under these conditions.

3 Optical

3.1 Raman

Raman analysis has proven to be a fast, versatile and accurate method to analyze many 2D materials [7, 14] including hBN. Raman analysis has proven greatly useful to identify layer number and purity of Gr samples, however, the same cannot be said for hBN since its Raman spectra is much less rich than Gr exhibiting only one high energy Raman active peak at ~1364cm^{-1} (shown in Fig. 40b right image) corresponding to an in plane optical mode (E_{2g}) where the B and N atoms move opposite to each other as shown in fig.40a. Ferrari et al. [7] also reported that a second high energy active peak for hBN is located ~55cm^{-1}, however, this peak has not been reported experimentally to date. In Fig. 40b we also show the Raman spectrum of cubic boron nitride since its useful to have it as a reference to ensure that our films do not consist of this phase.

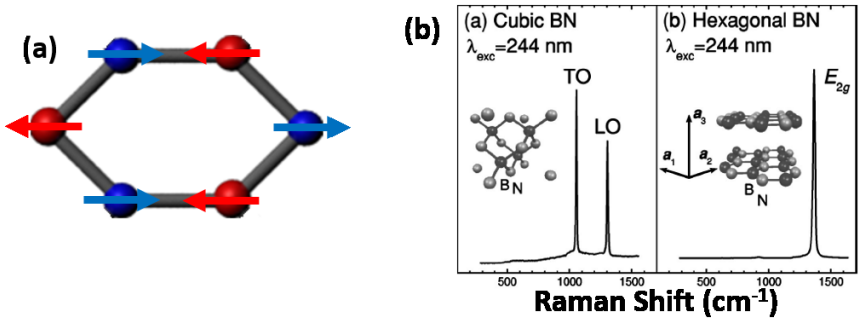

(c)		Cubic BN	Hexagonal BN	Diamond
ω_{ph} (cm^{-1})		1055	1364	1333
V_c (Å^3)		11.82	36.17	11.35
μ (a.u.)		6.10	3.05	6.00
514.5 nm, 2.41 eV				
n	(Ref. 49 and 50)	2.1	1.8	2.4
L (μm)	(Ref. 51–53)	1	0.25	1
a (Å^2)		0.5±0.6	10±5	4.3±0.6
$dS/d\Omega$		0.1±0.2	20±10	6.5±0.8
244 nm, 5.08 eV				
n	(Ref. 49 and 50)	2.3	2.1	2.7
L (μm)	(Ref. 51–53)	1	0.1	1
a (Å^2)		0.4±0.6	20±6	4.7±0.6
$dS/d\Omega$		1±2	1700±400	160±20

Figure 40

: (a) Depiction of the atomic in plane movements corresponding to the E_{2g} Raman active mode of hBN. (b) Measured Raman spectrum of cubic (left) and hexagonal boron nitride (right) taken from Ref. [7]. (c) Table II taken from Ref. [7] showing various materials parameters that are necessary to determine the Raman intensity of cubic and hexagonal boron nitride. Diamond is also given as a reference in the last row. The green square represents values for incidence energies in the green range (514.5nm) and the violet square for values in the DUV range (244nm).

3.1.1 Layer dependent signatures

It can be shown that the number of Raman scattered photons per layer is given by:

$$R_s = \frac{16}{\hbar\omega_l} P_l \Delta\Omega L \frac{dS}{d\Omega} \tag{6}$$

Where "P_l" is the laser power, "$\Delta\Omega$" the solid collection angle determined by the instrument setup, "L" the scattering length and "$\frac{dS}{d\Omega}$" the scattering efficiency. Figure 40c shows the values of $\frac{dS}{d\Omega}$ for cubic BN (an indirect material) and hexagonal BN (a direct material) where hBN consistently shows a larger value by at least an order of magnitude. Small corrections are typically made for layer number (i.e. thickness) and there are usually no significant changes in intensity as one proceeds to the monolayer limit as has been shown for graphene [14]. This does not seem to

be the case for hBN however, since many reports have shown that the intensity follows a somewhat linear trend down to bilayers and there's a sharp decrease for monolayers [8]. Figure 41a shows the results from Gorbachev et al. [8] where this relation is easily observed and Fig. 41b shows data taken from our CVD grown monolayers where the ratio between the bilayer and monolayer intensity is I_{bi}/I_{mono}~$1.5x10^3$. This is huge and cannot be accounted for by simply considering the thickness dependence on the number of scattered photons. One explanation can be put forth by observing the relation in Fig. 40c between an indirect semiconductor (cBN) and a direct one (hBN). We see that for indirect semiconductors the scattering efficiency drops dramatically even for below bandgap energies. Thus, the intensity decrease in monolayer hBN could potentially be due to a transition to an indirect gap. We also show in Fig. 41c that the area under the curve for the measured intensity is another good predictor of the layer number. The FWHM is also plotted in Fig. 41d and shows a steep decrease for bulk values indicating better crystallinity. This also accounts for the constant value observed for the Area plot after 4 layers since the area is proportional to the intensity and inversely proportional to the FWHM we see that while the intensity increases the FWHM decreases after 4layers making their ratio relatively constant.

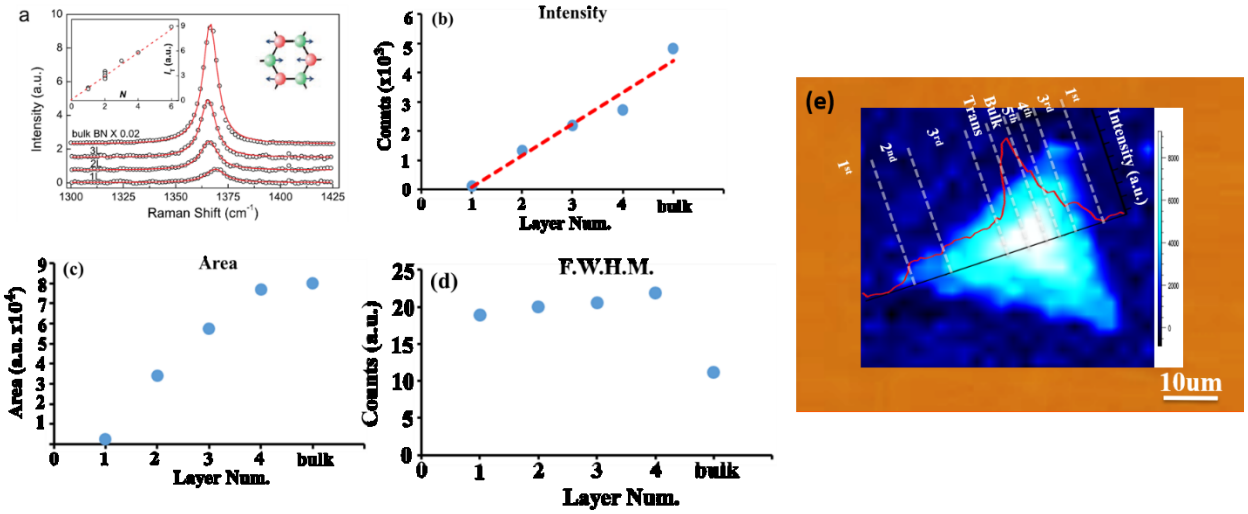

Figure 41

: (a) Raman spectrum and intensity plot versus layer number (inset) for exfoliated hBN of different thickness' taken from Ref. [8]. (b) Intensity of Raman signal for our CVD grown hBN as a function of layer number. (c) Area under the curve for the measure Raman intensities shown in (d) showing a layer number dependence. (d) FWHM of the Raman peaks used for the calculations in (b) and (c). (e) Raman map of the hBN island used for the Raman measurements shown in this figure. Overlayed on this map is a plot of the intensity of the Raman signal as a function of distance (therefore thickness) showing the same trend as in (b).

3.1.2 Substrate effects and Sheer mode

Another effect that contributes to the Intensity of the Raman signal for thin films is the interaction with the substrate which has been experimentally demonstrated for Gr [15, 16]. For our hBN samples we have found that the presence or absence of the substrate determines whether or not the Raman signal is measurable. Figure 42a shows an optical image of hBN transferred to a holey SiO_2/Si grid with 20um holes. Figure 42b shows a Raman map of an hBN multilayer nucleus found on the holey SiO_2 grid and Fig. 42c shows an SEM image of the same multilayer in 42b. Comparing the SEM image to the Raman map we can see that the upper left tip of the multilayer extends over a hole in the grid and its Raman signal is not observable. More detailed analysis is necessary in order to determine the exact nature of this interaction and to know whether its just to constructive interference when a substrate is present or whether there are other effects such as lattice expansion which have been shown in Gr [16].

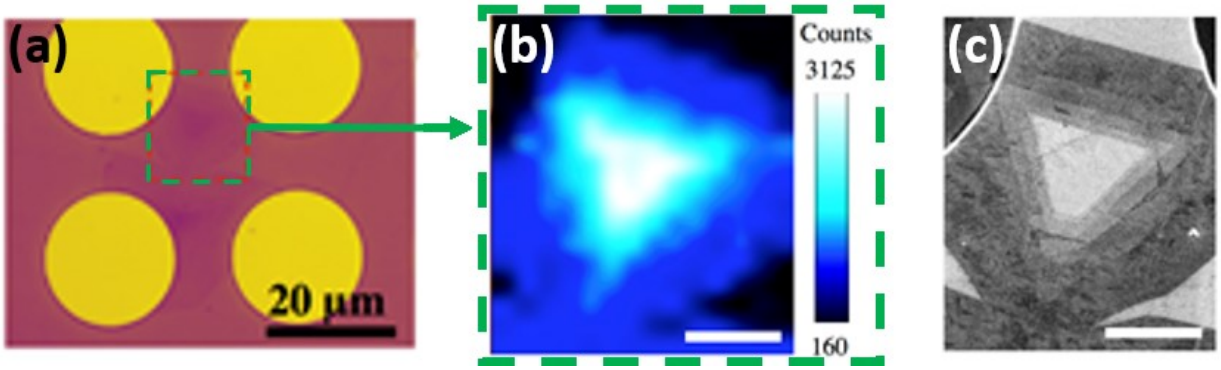

Figure 42

: (a) Optical image of hBN multilayers transferred to a holey SiO_2/Si grid with 20um diameter holes. (b) Raman map of an hBN multilayer located on the holey grid shown in (a). The map was created by plotting the integrated area under the spectrum between the shifts 1360-1375cm^{-1}. (c) SEM image of the same multilayer shown in (b). The scale bars in (b-c) are 10um.

Lastly, we show in Fig. 43 the different Raman spectra for varying thickness' of hBN where Fig. 43f shows their stacked plot. From this plot a clear blue shift can be seen as one proceeds from monolayer to bulk, this has been attributed to a relaxation of the hBN when transferred to SiO_2 [8].

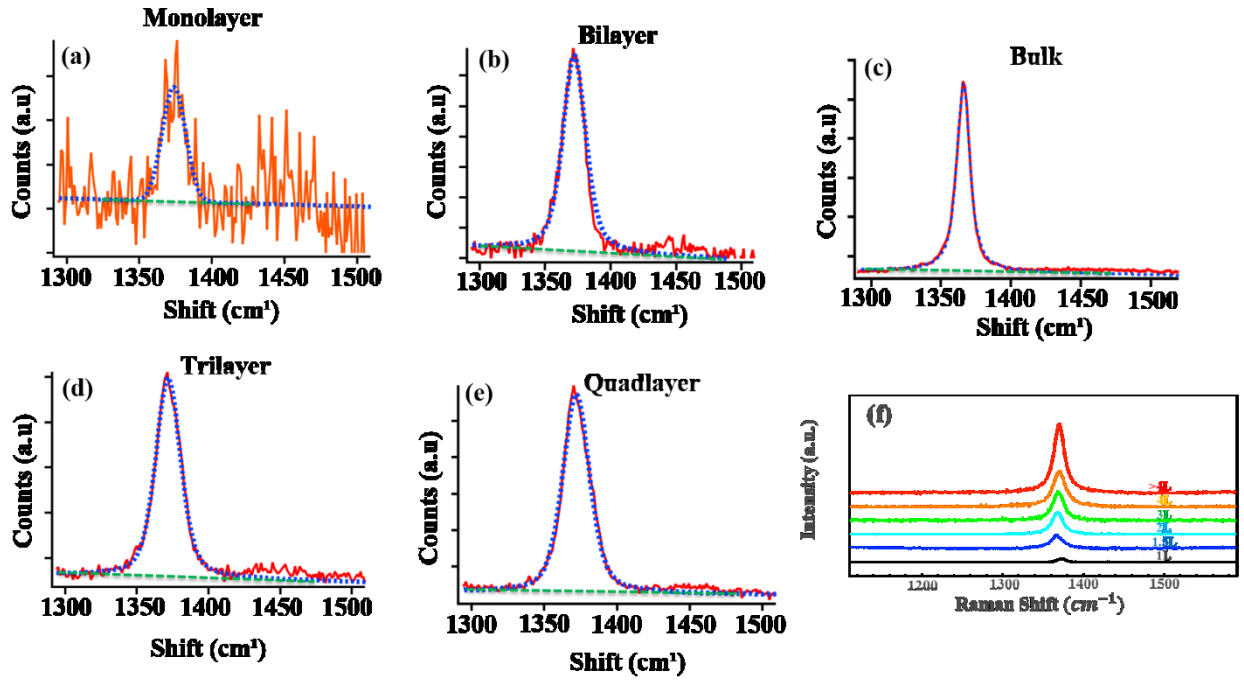

Figure 43

: Raman spectra of (a) Monolayer, (b) Bilayer, (c) Bulk (>5layers), (d) Trilayer and (e)Quadlayer hBN. These spectra were recorder from the hBN multilayer shown in Fig. 41e. (f) A stacked plot of the Raman spectra presented in (a-e).

3.2 UV-vis absorption

Figure 44 shows the absorption spectrum of a coalesced film of hBN transferred to a fused silica wafer (blue) along with the spectrum of bare fused silica (red). Its is clear from this plot that there is a distinct absorption peak at ~200nm which corresponds to an energy gap of ~6.2eV which is in agreement with other measurements done on CVD grown hBN [17, 18, 19]. The peak occurs at an absorbance of ~0.143 which corresponds to an absorption of ~28.1% for this monolayer of hBN. We note that this absorption is not necessarily the absorption of hBN since these measurements are done in air and attenuation of the light intensity can be due to various other sources such as scattering from H_2O molecules (which readily occurs in the UV), surface reflection and other physical process. In the inset of Fig. 44 we also show a plot of $\varepsilon^{1/2}/\lambda$ vs $1/\lambda$ where "ε" is the optical absorption taken from the main graph and "λ" is the wavelength of the incident light

in nm. Plots of this type are known as Tauc plots in reference to researcher who originally applied this analysis to Ge amorphous films [20]. Tauc' method comes from applying Fermi' golden rule to obtain the absorption coefficient as a function of wavelength "$\varepsilon(\omega)$" where with appropriate assumptions one obtains a linear relation of the form:

$$\omega^2\varepsilon = (\hbar\omega - E_g)^{1/2} \tag{7}$$

Where $\omega = 2\pi/\lambda$ and E_g is the bandgap of the material under measurement. If we plot $\varepsilon^{1/2}/\lambda$ (y-axis) as a function of $1/\lambda$ (x-axis) and extrapolate the plot (in the appropriate linear region) to the x-intercept we will find the E_g. For our data we estimate an E_g~5.65eV.

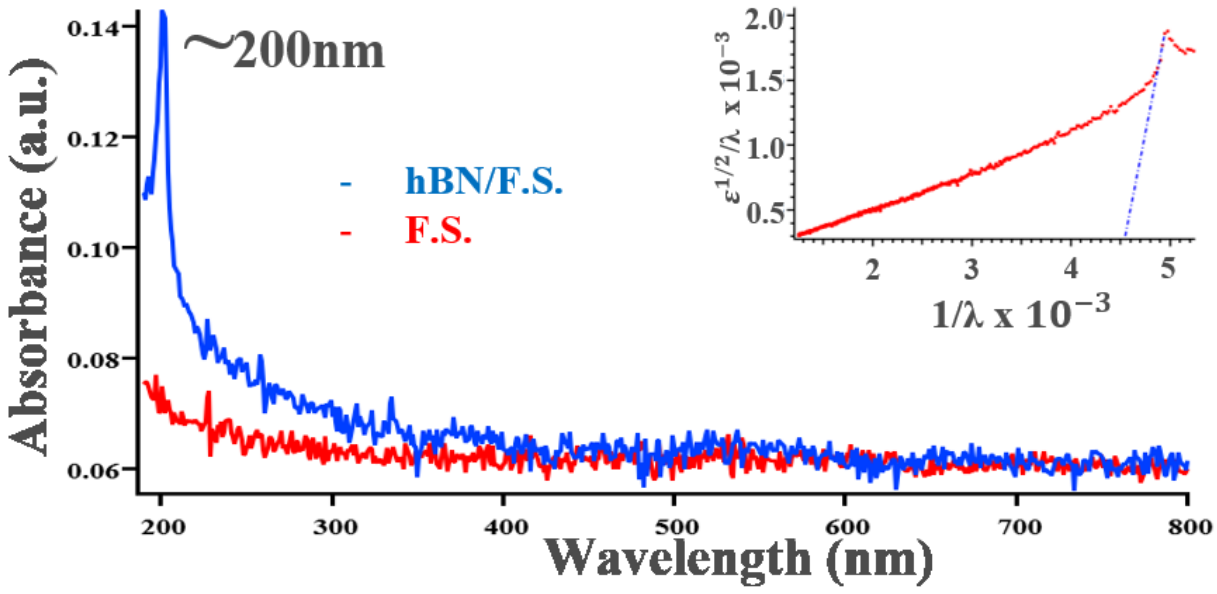

Figure 44

: UV-vis absorbance of a coalesced hBN monolayer grown on Cu-foil transferred to a Fused Silica substrate (blue) along with the absorbance of a bare fused silica wafer (red). (inset) Tauc's plot used to find the estimated optical bandgap of the thin film giving Eg~5.65eV.

4 Chemical analysis via XPS

Chemical analysis of our thin films was mainly done using X-Ray photoemission spectroscopy (XPS), however, we note that grazing incidence X-Ray Detection is also a commonly used method to characterize thin films. The reasons that these two methods are heavily applied to thin films is that they are surface sensitive techniques and minimize the signal from the bulk allowing the user to probe only the first few nm's of the surface.

One of the main emphasis' of this manuscript is the self-limiting nature of hBN growth on Cu due to the low diffusivity of B and N into it. We argue that our coalesced films are composed mostly of monolayers (>90%) with some small regions composed of thicker hBN that has grown mainly due to defect assisted island growth. XPS measurements done by Kidambi et al. [21] demonstrated that monolayer hBN has associated B-1s and N-1s peaks located at 191.1 and 398.6eV respectively, while multilayer hBN has them at 190.6 and 398.1eV. This makes is possible to distinguish between monolayer and multilayer signatures using high resolution XPS analysis. Figure 45c-d show high resolution XPS spectra of the B-1s and N-1s peaks of an hBN film grown on Cu foil. We note that our measurements were taken using an SSX-100 setup from surface science which uses an Al-K alpha source and has an SSI hemispherical analyzer capable of resolving peaks to within 0.25eV for measurements taken at high resolutions. This resolution is sufficient to differentiate monolayer hBN form the corresponding shifts observed from multilayers. The positions of our peaks in Fig. 44c-d are those corresponding to monolayers, given that the measurement is taken over an area of ~800x800um it can be inferred that most of our surface is covered by a monolayer of hBN. We also show survey spectrum of hBN/Cufoil (Fig. 44a) and hBN/SiO_2/Si (Fig. 44b) where the stoichiometry is close to the ideal value of B:N~1:1 in both substrates. Lastly we note the occurrence of a small pi-plasmon peak shown in Fig. 44c. This peak has been shown to occur in high quality crystalline sheets of hBN [21].

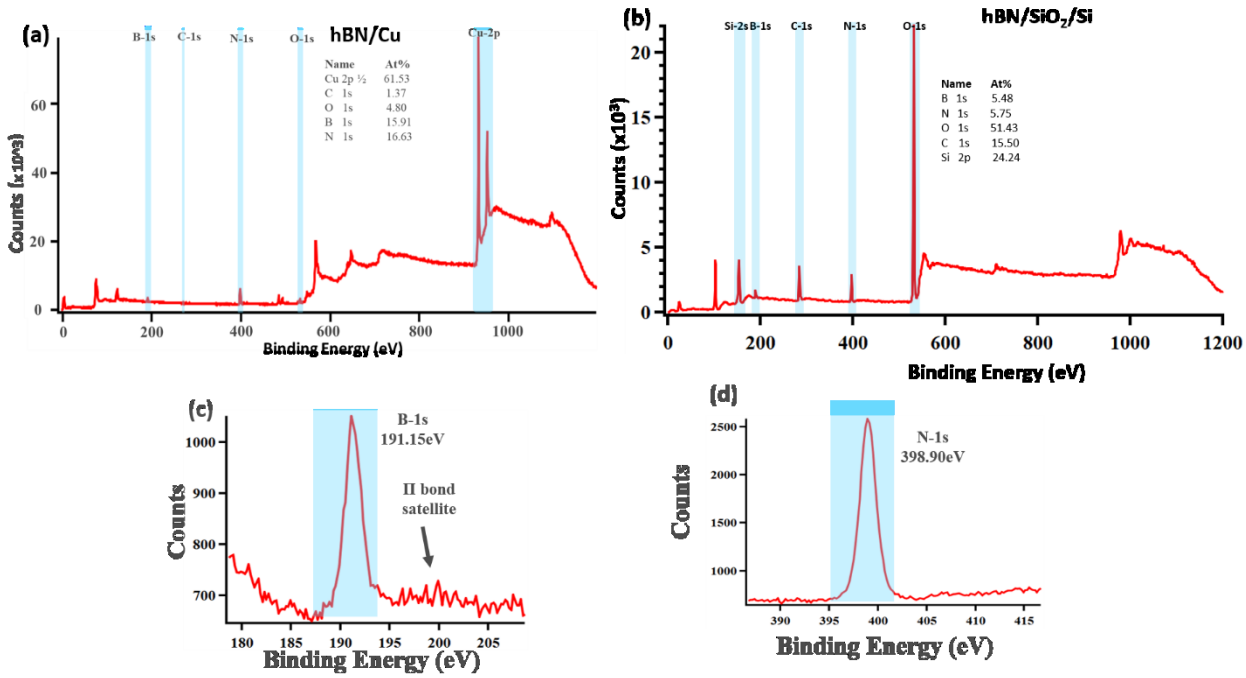

Figure 45

: XPS survey spectra of (a) hBN/CuFoil and (b) hBN/SiO_2/Si where the atomic percentages of the elements are calculated and its shown that B:N~1:1. High resolution XPS spectrum of the (c) B-1s and (d) N-1s peak where the peak positions are denoted and correspond to monolayer hBN. For the B-1s peak a pi-plasmon peak is observed as well.

5 AFM

Atomic force microscopy (AFM) was used to study the surface morphology of our hBN films after they were transferred to SiO_2/Si substrates. We note that the morphology of as grown hBN/Cu was proven to be difficult due to the large curvatures that were present after growth. Since AFM is a surface sensitive method its best results are obtained when samples are transferred to atomically flat substrates.

Figure 46a shows the AFM image of hBN/SiO_2/Si where the right inset is a trace of the height along an edge of the hBN sheet showing a height of ~0.5nm corresponding to monolayers [19]. We note that in order to obtain reproducible results contact mode AFM (CAFM) was used

for these measurements since it has been shown that tapping AFM (TAFM) gives inconsistent height measurements [22, 23]. This is mainly due to the out of plane pi-bonds that are present in hBN which can attract and interact with water vapor in the atmosphere (i.e. wetting). This water vapor on the surface in turn interacts with the AFM tip through attractive capillary forces. Although the measured heights using TAFM are influenced by a variety of forces (electrostatic, van der waals, capillary and chemical) its been shown that capillary can be dominant. This is a problem because precise measurements in TAFM occur when the net force on the tip is repulsive, however capillary forces will lead to attractive behavior giving inconsistent results [23]. Figure 46b shows the AFM map of a multilayer crystal of hBN where the height profile (shown below the AFM plot) shows a progressive increase of steps of ~1nm in height. Figure 46c shows the phase plot of the same multilayer where the hBN can be easily differentiated. This contrast in the phase plot is due to the different frictional properties present on 2D surfaces which change the measured phase with respect to the desired phase, this phase difference is what's show in Fig. 46b [22]. The SEM image of the same multilayer is shown in Fig. 46c for comparison.

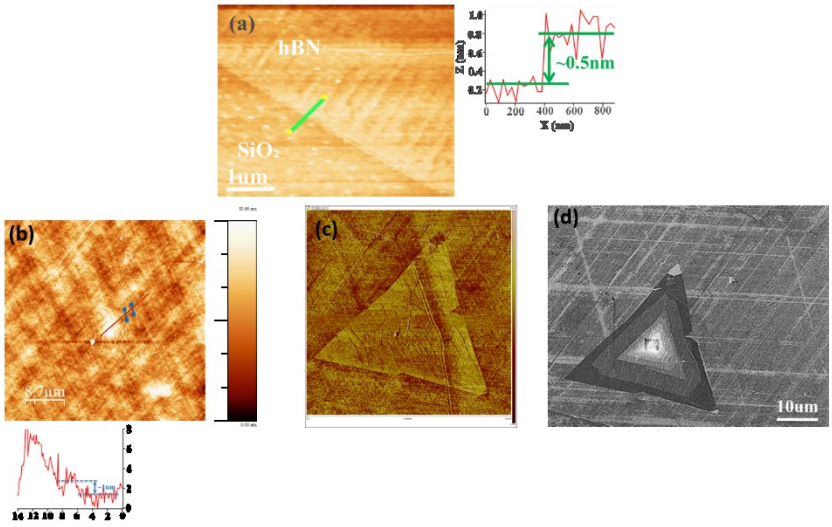

Figure 46

: (a) AFM map of hBN transferred to SiO_2. The right plot shows the height profile along the green line in the AFM image where a step height of the hBN of ~0.5nm is found. (b) AFM scan of a multilayer flake of hBN on SiO_2. It's hard to distinguish the hBN from the SiO_2 in this scan. The plot below shows a height profile along the red line shown in the AFM scan where step heights of ~1nm are calculated. (c) Phase image of the same multilayer flake in (b) where a clear distinction of the hBN is observed with respect to the oxide. (d) SEM image of the multilayer flake analyzed in (b) and (c).

6 Additional Characterization

Many other additional techniques were used to characterize our grown films which do not necessarily fit into any of the previous categories. These results will be presented here.

Low energy electron microscopy (LEEM) was used to obtain the detailed microstructure of our hBN films on Cu. LEEM has many advantages including the ability to obtain crystal structure information by low energy electron diffraction (LEED) as well as spectroscopic information about the material by varying the landing energy of the electrons which leads to complex IV curves rich in information about the local electronic properties [24]. Shown in Fig. 47a is an SEM image of a coalesced hBN film on Cu and in 47b we show a LEEM image of the same sample. The LEEM reveals that the surface is much less homogenous than the SEM image suggests. Figure 47c is a magnified view of 47b where tiny micrometer sized tears (black striations) are observed. Figure 47d-f shows the same pattern of images ((d) SEM, (e) Low Mag. LEEM, (f) Higher Mag. LEEM) for uncoalesced smaller nuclei where we can again observe the same micro tears. This is a huge problem for potential devices made out of this material and we hypothesize that it may be due to the very rapid cooling rates we used (>100°C/min) for these growths which lead to a large amount of stress in the hBN due to the difference in thermal expansion coefficient with the Cu.

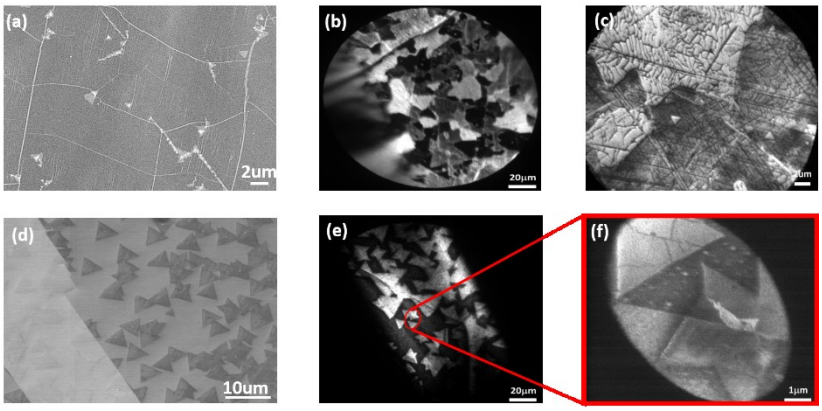

Figure 47

: (a) SEM image of coalesced hBN film on Cu. (b)Low magnification LEEM of coalesced hBN showing patchy film. (c) High magnification LEEM of coalesced hBN shown a large amount of micro-tears present. (d) SEM image of uncoalesced hBN nuclei. (e) Low magnification LEEM of nuclei. (f) High magnification LEEM of nuclei showing again the presence of tears.

The high cooling rate could have other detrimental effects on our films such as inducing re-structuring in the Cu beneath the hBN. Shown in Fig. 48 is an SEM image of hBN nuclei on Cu as where in 48b the magnified image shows that a clear re-structuring of the Cu occurs in the hBN covered regions. This has been attributed to the difference in thermal expansion between the hBN and Cu [25, 26]. We note that the re-structuring has not been observed in hBN/Ru [27] grown at 783°C, thus, it may be that this re-structuring occurs due to the high mobility of Cu surface atoms at the growth temperatures of 1050°C which are near the melting point (~1085°C). This is perhaps why this is not observed in Ru which has a melting point of 2334°C.

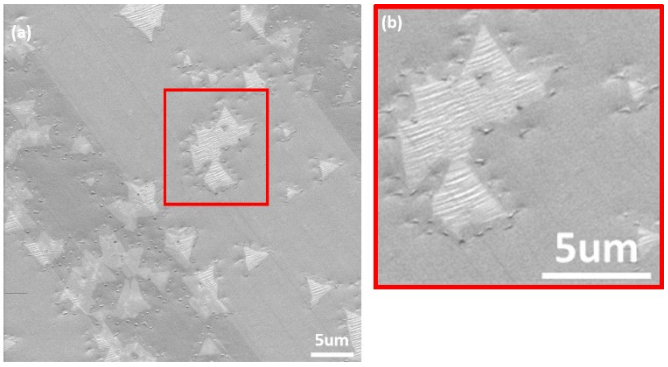

Figure 48

: (a) SEM image of hBN nuclei on Cu foil. (b) Magnified view of region shown in red circle in (a) where a clear wrinkling of the Cu surface can be observed in the hBN covered regions.

TEM studies were also done on our coalesced films in order to validate the argument that we had obtained films composed 100um sized grains. Shown in Fig. 49a is an SEM of a coalesced film used for TEM analysis before transfer to a TEM grid. Fig. 49b shows the film on the TEM grid (SiN) and Figs. e-i show our diffraction results. Due to the small field of view of the TEM instrument we devised a different method to analyze the crystallinity over a 100um region. In Fig. 49b we show a green line with areas labeled i-v. We took point diffraction images at each area and found that single crystal hBN was observed in areas i-iii-v with a characteristic diffraction pattern as shown in 49e,g. A complex diffraction pattern was observed in regions ii and iv with the corresponding diffraction pattern shown in 49f. This is attributed to a grain boundary which was confirmed using DF-TEM in 49c. Thus, it can be concluded that between regions ii-iv there is a single crystal hBN grain which was measured to be 100um. We also show that signatures of monolayer and bilayer hBN were found on films where bilayer growth was observed (49d). We took the intensity profile along the line between the two arrows shown in Figure 49 h,i respectively. The profile shows that for monolayer, the outer {2110} peak intensity is smaller than the inner {1100} peak intensity, whereas the peak intensity ratio of bilayer is $I_{\{2110\}}/I_{\{1100\}}>1$. This result is consistent with AA' stacked hBN [28]. Our result demonstrates that the monolayer h-BN can be identified *via* examining if the intensity ratio is $I_{\{2110\}}/I_{\{1100\}}<1$.

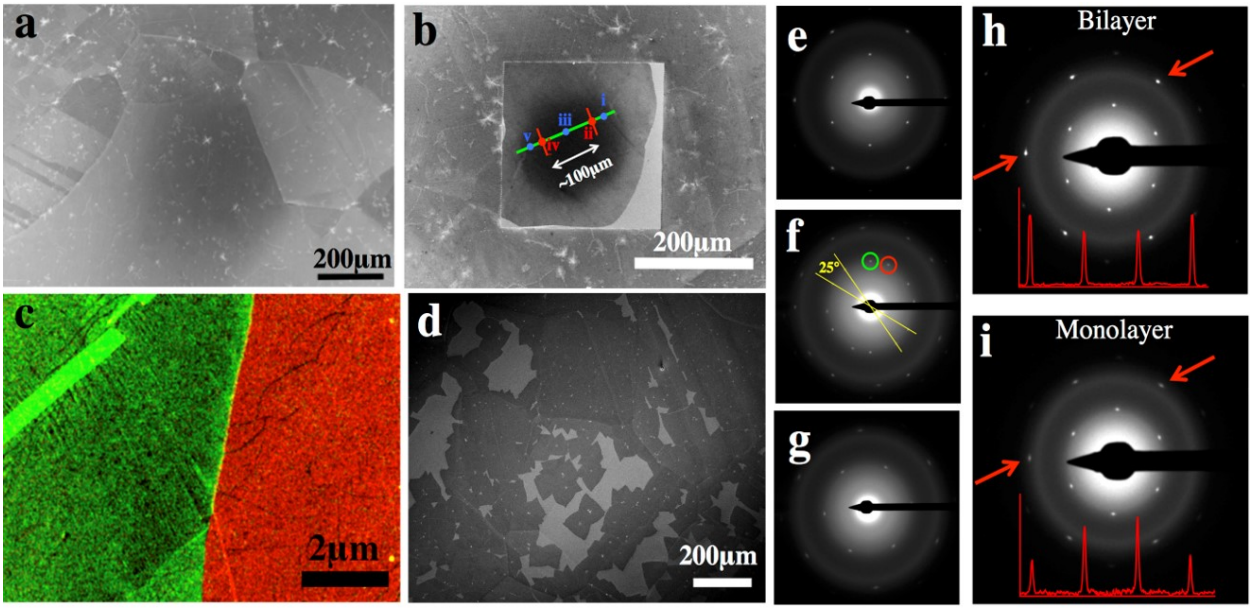

Figure 49

:(a) SEM image of the continuous film before transfer. (b) SEM image of coalesced film after transfer onto SiN grids and the square in the middle of **b** is a TEM grid window (The window was slightly broken when we did the SEM scan after the TEM analysis). (c) False-color dark-field TEM recorded at the grain boundary at position ii labeled in **b**. (d) SEM image of nearly coalesced h-BN film. (e)-(g) SAED patterns recorded around the grain boundary at position ii labeled in **b**. (h) SAED pattern and intensity profile of bilayer h-BN. (i) SAED pattern and intensity profile of monolayer h-BN.

Lastly, we present interesting results regarding the role of the Cu orientation when it comes to the equilibrium shape of the hBN nuclei. During our many growth experiments we encountered several different hBN morphologies were possible (See Fig. 50a). In order to investigate what may be influencing the morphology we did a combination of SEM and EBSD analysis to see if the Cu orientation played any rol. Figure 50b-c shows SEM images where different hBN morphologies are present in different Cu grains. Figure 50e shows the results of EBSD mapping of the Cu area in 50(c) and 50d shows a superposition of the SEM and EBSD images. It can be clearly seen that truncated nuclei appear in (111) and (101) like directions while triangular nuclei appear in (100) like directions. This suggests that despite the weak coupling with the substrate, the Cu seems to play a critical role in the initial nuclei morphology [29, 30]. Subsequent analysis would require a

complete description of the thermodynamics using a Wulff construct argument appropriate for thin films [31].

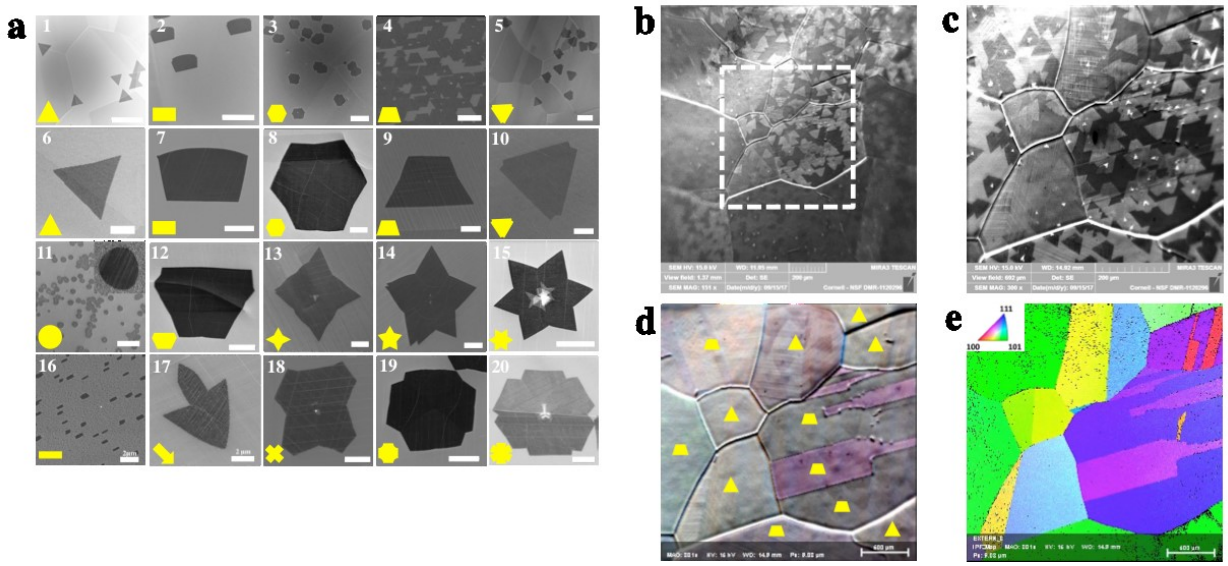

Figure 50

: (a) Varied h-BN domain shapes. The scale bars are 20 μm. (b) Low-magnification SEM image of h-BN growth on Cu. The white box indicates the region in b-e. (c) SEM image showing the variation of h-BN domain shape on different Cu grains. (d) False color image of the same region labeled the h-BN domain shape on each Cu grain. (e) EBSD map of the same region.

References

[1] S. Gorantla and a. et, "A universal transfer route for graphene," *Nanoscale,* vol. 6, p. 889, 2013.

[2] X. Wang and a. et, "Direc delamination of graphane for high performance plastic electronics," *Small,* vol. 10, p. 694, 2014.

[3] H. Wang, Y. Zhao, Y. Xie, X. Ma and X. Zhang, "Recent progress in synthesis of two dimensional hexagonal boron nitride," *Journal of semiconductors,* vol. 38, pp. 031003-1, 2016.

[4] L. Jiao and a. et, "Creation of nanostructures with poly(methyl methacrylate) mediated nanotransfer printing," *Journal of the American Chemical Society,* vol. 130, p. 12612, 2008.

[5] A. Reina and a. et, "Transferrinf and identification of single and few layer graphene on arbitrary substrates," *Journal of Physical Chemistry C,* vol. 112, p. 17741, 2008.

[6] A. G. F. Garcia and a. et, "Effecive cleaning of hexagonal boron nitride for graphene devices," *Nanoletters,* vol. 12, p. 4449, 2012.

[7] A. C. Ferrari, S. Reich, A. Loiseau, R. Arenal, I. Bello and J. Robertson, "Resonant raman scaterring in cubic and hexagnoal boron nitride," *Physical Review B,* vol. 71, p. 205201, 2005.

[8] R. V. Gorbachev and a. et, "Hunting for monolayer boron nitride: optical and raman signatures," *Small,* vol. 7, p. 465, 2011.

[9] S. Nakao and a. et, "Effects of nitrgen gas ratio on composition and microstructure of BCN films prepared by RF magnetron sputtering," *Vacuum,* vol. 84, p. 642, 2010.

[10] M. A. Mannan and a. et, "Orientation of BCN hybrid dilms deposited on Ni(111) and polycrystalline Ti subsrtates explored by x-ray absorption spectroscopy," *Thin solid films,* vol. 519, p. 1780, 2010.

[11] E. Bengu and a. et, "Theoretical and spectroscopic investigations on the structure and bonding in BCN thin films," *Thin Solid Films,* vol. 518, p. 1459, 2009.

[12] S. Satoru and a. et, "Growth ot atomically thin hexagonal boron nitride films by diffusion through a metal film and precipitation," *Journal of Physics D,* vol. 45, p. 385304, 2012.

[13] L. H. Li, J. Cervenka, K. Watanabe, T. Taniguchi and Y. Chen, "Strong oxidation resistance of atomically thin boron nitride nanosheets," *ACS Nano,* vol. 8, p. 1457, 2014.

[14] A. C. Ferrari and a. et, "Raman spectrum of graphene and graphene layers," *Physical Review Letters,* vol. 97, p. 187401, 2006.

[15] Y. Y. Wang and a. et, "Raman studies of monolayer graphene: The subsrtate effect," *Journal of Physical Chemistry C,* vol. 112, p. 10637, 2008.

[16] I. Calizo and a. et, "The effect of subsrtates on the Raman spectrum of graphene: Graphene on Sapphire and Graphene on Glass," *Applied Physics Letters,* vol. 91, p. 201904, 2007.

[17] K. H. Lee and a. et, "Large scale synthesis of high quality hexagonal boron nitride nanosheets for large area graphene electronics," *Nano Letters,* vol. 12, p. 714, 2012.

[18] K. K. Kim and a. et , "Synthesis of monolayer hexagona boron nitride on Cu foil using chemical vapor deposition," *Nano Letters,* vol. 12, p. 161, 2012.

[19] L. Song and a. et, "Large scale growth and characterization of atomic hexagonal boron nitride," *Nanoletters,* vol. 10, p. 3209, 2010.

[20] J. Tauc, R. Grigorovici and A. Vancu, "Optical properties and electornic structure of amorphous germanium," *Physica Status Solidi,* vol. 15, p. 627, 1996.

[21] P. R. Kidambi and a. et, "In situe observatoins during chemical vapor deposition of hexagonal boron nitride," *Chemistry of Materials,* vol. 26, p. 6380, 2014.

[22] C. Lee and a. et, "Frictional characteristics of atomically thin sheets," *Science,* vol. 328, p. 76, 2010.

[23] P. Nemes-Incze and a. et, "Anomalies in thickness measurements of graphene and few layer crystals by tapping mode atomic force microscopy," *Carbon,* vol. 46, p. 1435, 2008.

[24] J. Kautz and a. et, "Low energy electron potentiometry: Contactless imaging of charge transport on the nanoscale," *Scientific Reports,* vol. 5, p. 13604, 2015.

[25] G. E. Wood and a. et, "van der Waals epitaxy of monolayer hexagonal boron nitride on copper foil: growth, crystallography and electronic band structure," *2D materials,* vol. 2, p. 025003, 2015.

[26] N. R. Wilson and a. et, "Weak mismatch epitaxy and structural feedback in graphene growth on copper foil," *Nano Research,* vol. 6, p. 99, 2013.

[27] P. Sutter and a. et, "Chemical Vapor deposition and etching of high-quality monlayer hexagonal boron nitride," *ACS Nano,* vol. 9, p. 7303, 2011.

[28] C. J. Kim and a. et, "Stacking order dependant second harmonic generation and topological defects in hBN bilayers," *NanoLetters,* vol. 13, p. 5660, 2013.

[29] J. Yin and a. et, "Large single crystal hexagonal boron nitride monolayer domains with controlled morphology and straight merging boundaries," *Small,* vol. 11, p. 4497, 2015.

[30] Y. Zhang and a. et, "Vapor trapping growth of single crystalline graphene flowers: synthesis, morphology and electronic properties," *NanoLetters,* vol. 12, p. 2810, 2012.

[31] I. Markov, Crystal growth for beginners, 2003: World Scientific, New York.

V. hBN Electronics

1 Historical Overview: Transport in Insulating Crystals

Historically, insulators were simply defined as materials which would carry little to no current, at least up to electrical breakdown. Insulators were also seen to be poor conductors of heat,

a detail that was made explicit in 1853 by the Wiedmann-Franz law:

$$\frac{\kappa}{\sigma} = LT \tag{8}$$

This law states that the electrical conductivity (σ) is proportional to the thermal conductivity (κ) at a given temperature (T) by a proportionality constant called the Lorenz number (L). This definition, and similar ones, are also used in the high school classroom today when initially studying the classification of materials with regards to conductivity. However, soon after the appearance of Quantum Mechanics and its applications to solids [1] Mott and Gurney established that similar to the process of injecting electrons into vacuum, electrons (or holes) could also be injected into insulating crystals [2]. This was possible due to the newly developed energy band picture of solids furnished by Bloch [1]. This lead to the Mott-Gurney law for current injection in solids, which was in essence the solid-state analogue of Childs Law for Injection into Vacuum. Mott-Gurney' law reads:

$$J = (9/8)\epsilon\mu(V^2/L^3) \tag{9}$$

Where "ϵ" is the dielectric constant of the solid, "μ" the mobility, "L" the length along which the voltage "V" is dropped. Due to its dependence on the square of the applied voltage as well as the fact that its derived under the assumptions of a perfect crystal (i.e. the role of defects is negligible or not taken into account) it is sometimes also called the "trap free square law". The role of defects in injection currents into solids was only passingly mentioned by Mott and Gurney, it was not until Albert Rose came along and gave a detailed theoretical (and experimental) framework on the role of defects in injection currents [3, 4].

With the framework of band theory and the work done by Mott, Gurney, and Rose space

charge transport in crystals matured greatly and many experimental and theoretical studies were done on this topic in the 50's [5, 6, 4, 3]. The historical development of this field is actually quite interesting is mostly attributed to the work done in RCA labs on the observed dark currents on photoconductive films used for a prototype "TV camera" (i.e. a CRT television). The observance of these currents in the absence of illumination was not expected and was initially attributed to breakdown in the films [5], however, it was Rose et al. who set the record straight and found that the dark currents were due to space charge injection into the films [4]. An entire book could be written on the historical developments of transport in insulating crystals, however, this is not the intent of this manuscript, the reader is referred to some great reviews that have been written on the topic [7, 8].

In recent years, space charge limited (SCL) transport has been heavily studied in the conduction of organic semiconductors [8], however, only recently has it been shown to be applicable to 2D materials as well. Its relevance in the 2D world and the progress in conduction of hBN thin films will be presented next.

2 Previous results on hBN transport

As a wide bandgap semiconductor, hBN has mostly been used for its insulating properties and as a substrate or sacrificial layer for other 2D material systems as was discussed in the introduction of Chapter 1. In its 3D form hBN has been shown to be a good p-type conductor where Mg doped hBN has shown to have a resistivity 6-7 orders of magnitude smaller than Mg doped AlN or GaN [9]. This decreased resistivity is mainly due to the exponential dependence on free carriers (holes in the case of Mg) with activation energy $p \sim \exp(-E_A kT)$ where it was shown that Mg doped hBN has hole activation energies of ~31meV in comparison to 170meV and 510meV for GaN and AlN respectively. The hBN used in the study Dahal et al. [9] was grown by

MOCVD via TEB and NH_3 at ~1300°C on a sapphire substrate. The p-type doping of hBN has proven to be a crucial factor for applications in solid state lighting where it's been used a p-type contact to AlGaN p-n junctions to facilitate hole injection into the recombination region and increase the efficiency of the diode [10]. N-type doping of hBN continues to prove difficult today where Si has been used as a dopant but the Si doped hBN films only exhibited good conduction at high temperatures (T>800K) [11].

With regards to the 2D form of hBN there have been many recent advances which have been slowly pointing at the possibility that CVD grown 2D hBN may be p-type doped due to B vacancies [12]. Other studies suggest that Carbon impurities which substitute N sites act as acceptors in high temperature high pressure produced single crystal hBN [13]. In this study it was found that acceptors more readily change their charge state when induced by an STM tip, thus, it was concluded that they must be very close to the valence band edge. Thus, even in as grown hBN it can be concluded that under appropriate it may exhibit p-type conductivity due to intrinsic defects that form during the growth process.

With regards to electrical measurements of BN nanostructures, one of the first papers detailing the conductive properties of these nanostructures was done by Radosavljevic et al. [14] where they contacted a BNNT via two Ni electrodes (as shown in the inset of the I-V plot in Fig. 51a) and used a doped Si wafer as a back gate. They showed that the conduction was p-type by gate modulation and mentioned that they obtained very poor capacitive coupling through the oxide layer since they were only able to see gate modulation for oxides thinner than 10nm. Their temperature dependent I-V response is shown in Fig. 51a. Following this result in 2010 Zeng et al. [15] demonstrated that Boron Nitride Nanoribbons (BNNR) obtained via unwrapped BNNT's also exhibit p-type conduction where their contacts were in this case Au and W as shown in Fig.51b.

They saw ~3 orders of magnitude increased conductivity in the BNNR with respect to the parent BNNT. They attributed their conduction to be partly due to vacancies in the BNNR and the enhancement due to edge mediated currents along the BNNR zigzag edges. Currently, they hold the record for the largest mobility in a BN nanostructure with a value of $58cm^2/Vs$. Song et al. [16] also attempted to observe electrical conduction in their CVD grown hBN films by fabricating a Hall measurement structure made from Au contacts as shown in Fig.51c. They were unsuccessful and reported that their CVD grown hBN is insulating. It was not until 2015 when Mahvash et al. [17] demonstrated that CVD grown hBN monolayers exhibited signs of SCL transport as shown in Fig.51 d. Their measurements showed mobilities of $\sim 1x10^{-2}cm^2/Vs$ and they reported very low yields of only 18 working devices. They argued that their devices were p-type conductive due to the band alignment of their Ni contacts with the hBN, however they did not support this argument with Hall or Seebeck results. Finally, in 2017 Laleyan et al. [18] demonstrated that CVD grown hBN films can be used as effective p-type contacts to AlN/GaN DUV emitters (See Fig.51e). Their hBN was not intentionally doped with Mg as in prior studies and they argued that their p-type conductivity came from intrinsic B vacancies in the as grown hBN. They supported their argument with DUV PL measurements, shown in Fig. 51e, of hBN grown on SiO_2 where they attributed the observed peak at ~260nm to defects in the hBN. They again did not show and Hall or Seebeck measurements.

From this brief overview, it can be seen that a story has been developing for the past ~3yrs. where researchers are finding more and more evidence that CVD hBN can exhibit decent p-type conductivity due to natural defects that form during the growth. Until now no one has shown definitive evidence of the conduction to be either p-type, via Hall or Seebeck test, or of the type of defects that induce this conductivity. This trend inspired us to pursue these theories with our own

CVD grown hBN and see if we would obtain the same electrical characteristics and perhaps shed a light on the nature of its conduction. The results of these studies will be presented in the following sections.

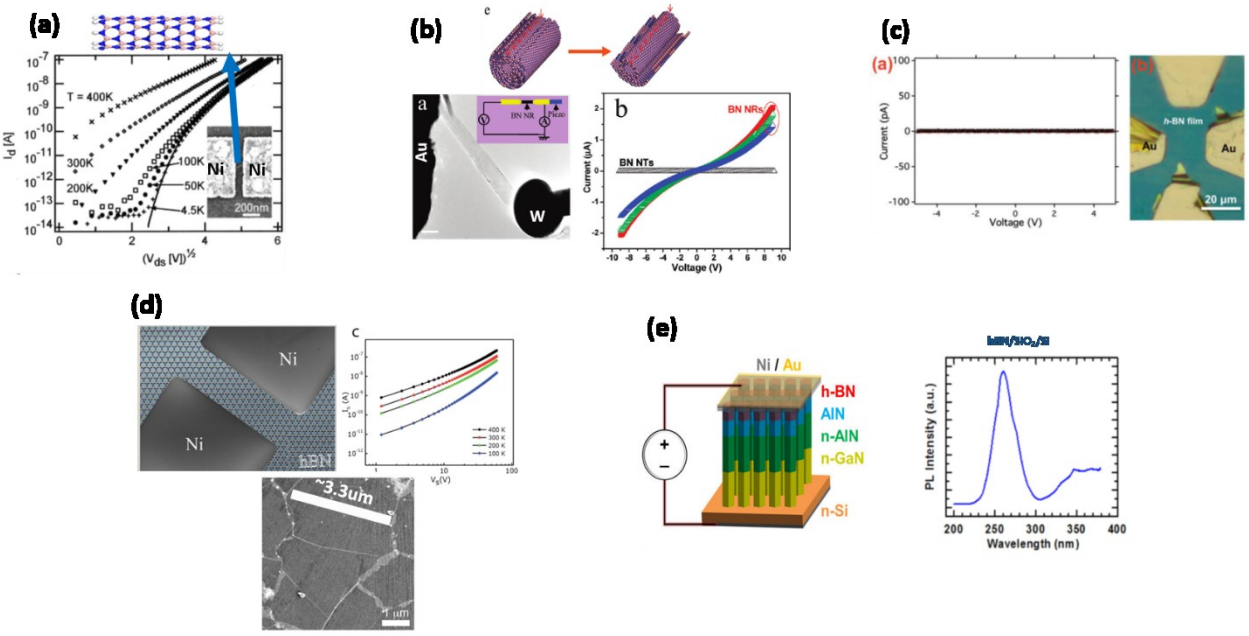

Figure 51 : (a) Temperature dependent I-V plot of a BNNT contacted by Ni electrodes from ref. [14]. (b) (top) Depiction of the unwrapping of a BNNT to a BNNR. (bottom left) SEM of a BNNR contacted by Au and W electrode. (bottom right) Room temperature I-V curves for the BNNR shown in the SEM [15]. (c) (Left) Room temperature I-V plot for CVD grown hBN done by ref. [16]. (Right) Optical image of device used for the measurements shown in the I-V plot on the left. (d) (top left) Depiction of a device made from CVD hBN using Ni contacts [17]. (top right) I-V curves obtained from the device shown on the left. (bottom) SEM image of the monolayer CVD hBN used for this study. (e) (left) depiction of device architecture used in ref. [18] showing CVD deposited hBN as the top p-contact to the AlN layer. (right) DUV PL of CVD grown hBN on SiO_2/Si showing a peak ~260nm which was attributed to defects in the hBN lattice.

3 Space Charge Injection

To study the electrical properties of our hBN films we transferred them to a SiO_2/Si substrate. The transfer process from Fig. 38 is reproduced in Fig. 52b for convenience. The oxide was a wet oxide 2um thick on a p-type Si substrate. Metal contacts (Au) were defined and deposited

using standard photolithography processes. The resulting device structures with contacts are shown in Fig.52 a and c. To facilitate the discussion of our results we've divided our devices into three different generations (gen-I, gen-II and gen-III). The design of the contact pads for gen-I are shown in Fig. 52a where 4 probe structures were made in order to facilitate the extraction of hBN's sheet resistance. The inset of Fig. 52a shows a typical channel region for this generation where the width and length are 10um and the metal used is Au. The contact pads were re-designed for gen-II and gen-III were Au square pads of 100um on a side were deposited, as shown in Fig. 52c. The channels lengths were varied from 3, 5, 7, and 10um, a typical 10um device is shown in the inset of Fig. 52c. We note that using Ti/Au contacts were found to be inferior to Au contacts as has been reported in previous studies [14, 19]. In Fig. 52d we also present the flat band diagram accompanied by the equilibrium band diagram in Fig. 52f. The equilibrium band diagram was obtained using a 1D poisson solver [20] with the parameters shown in Fig. 52d and a Fermi level location of 150meV above the valence band. The location of the fermi level was determined by tight binding where the carrier density corresponding to this location was extracted from the I-V curves of our measured devices. P-type carriers are assumed due to the alignment of the Au-hBN flat band diagram which provides a smaller barrier than it would for electrons. A further discussion of the nature of the carriers will be provided shortly. Full details regarding the tight binding model are available in Appendix B. We also present a Raman map of a 10um channel device from gen-III in Fig. 52e where the map was generated by finding the integrated area under the curve from 1360-1380cm^{-1}. In Fig. 52g we present a characteristic Raman spectrum obtained from Fig. 52e where a peak at ~1368cm^{-1} is present due to the hBN in the channel. We note that the spectrum presented in Fig. 52g shows a low signal to noise ratio for the hBN Raman signal due to the monolayer thickness of the film in the channel [21].

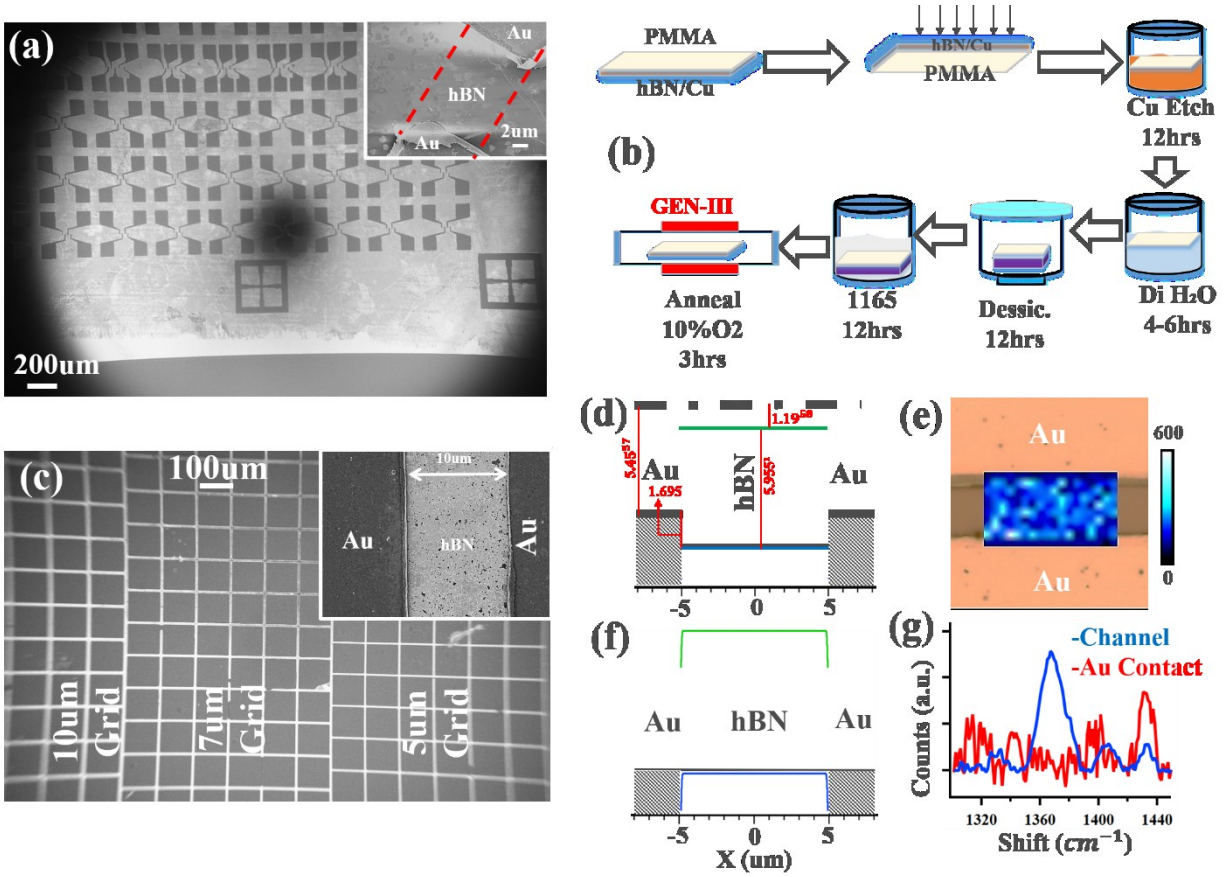

Figure 52 : (a) SEM micrograph of various devices in gen-I. The inset shows a magnified view of a 10um channel in gen-I. (b) Depiction of transfer process used to deposit hBN onto SiO_2 prior to contact deposition. The last step (Anneal) corresponds only to gen-III devices. (c) SEM micrograph of various devices representative of the contact geometry in gen-II and gen-III. The inset shows a magnified view of a typical 10um wide device. (d) Flat-band diagram for the Au-hBN-Au device geometry used in this study. (e) Raman map if a channel in a 10um wide gen-III device where the map intensity is acquired by integrating the area from 1360-1380cm^{-1}. (f) Equilibrium band diagram for the structure in (d) using a 1D poisson solver[23]. (g) Raman spectrum taken from the map in (e) at the Au contact and the hBN channel. A weak hBN peak is clearly visible ~1368cm^{-1}.

The I-V curves of our gen-I, II and III devices are presented in Figs. 53b, d and f respectively. All measurements were taken in ambient conditions. Two terminal measurements were performed using a Cascade Sumit-11000 system where the back gate remained grounded. Three terminal measurements were also performed with gate voltages as high as 40V, no modulation of the source current by the gate voltage was observed which is mainly due to the poor

capacitive coupling of the hBN/SiO_2 configuration. More details on back gate modulation will be given in the following section. Control samples using Au contacts fabricated on bare SiO_2(2um)/Si(p-type) substrates following the same fabrication procedures were also measured (See Appendix C). Measured control samples have current levels that are ~7 orders of magnitude smaller than our gen-III devices with h-BN channels. For our gen-I devices small current levels on the order of ~pA's were obtained and a very low yield of 3/100 working devices was found. For this generation the small grain hBN using the wrapping growth method described previously was used were the grain size was ~10-20um. When imaging these devices (See section on Grain Boundaries) it was noticed that the devices which worked showed an absence of grain boundaries within the conducting channel. To test this theory the pad geometry for gen-II was modified to accommodate a wider channel (100um) with varying lengths of 3, 5, 7 and 10um as shown in Fig. 52c. The wider channels would facilitate the availability of a region within the channel free of grain boundaries since our grain size was ~10um while the channel length was 100um. As can be seen in Fig. 53d the current levels in gen-II show a wide variation from pA's to uA's in our best devices. The yield is once again low showing only 6/100 tested devices working. The non-uniformity in the current levels in this generation can be attributed to the lack of a good metal contact due to the presence of residue after transferring 2D films using PMMA [22, 23, 24, 25]. To tackle the residue problem and thus to improve uniformity in our results, we incorporated a high temperature anneal step in our transfer process for our gen-III devices. The anneal took place at 800°C in a 10% O_2 in Ar environment at positive pressures, these parameters have been shown to remove organic residues from hBN [22]. This anneal was done immediately after the 12hr. dip in 1165 solvent as shown in Fig. 52b. Another important difference for gen-III is that the size of our hBN nuclei was increased by an order of magnitude to ~100um by using the pocket growth

method described earlier. These two differences for our gen-III devices increased our yield to ~20/100 working devices and increased our current magnitudes to >100uA's. The I-V curves for our gen-III devices are shown in Fig. 53f where the signal is less noisy and the current magnitudes are more uniform.

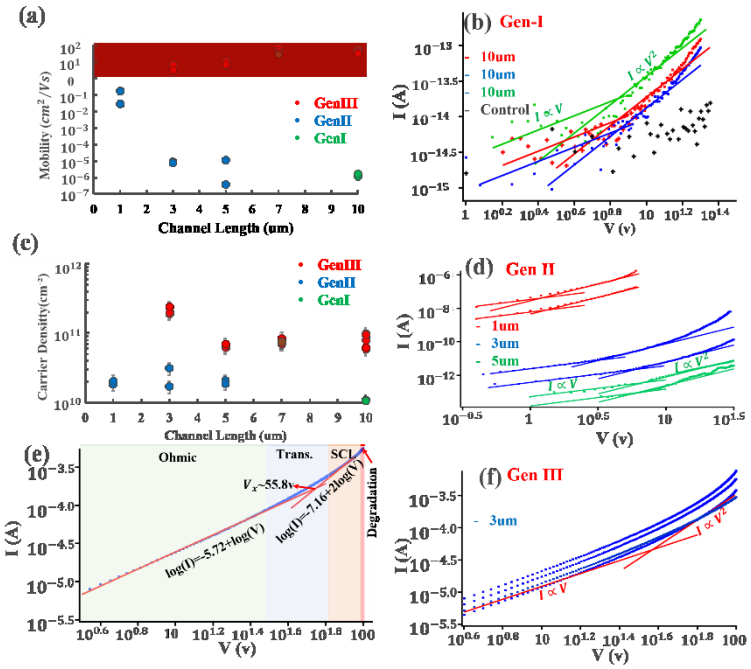

Figure 53 : (a) Calculated mobilities for the three different device generations as a function of channel length. The gen-III devices are well constrained within a narrow range showing the expected independence with regards to channel length. (b) I-V (log-log) plots of gen-I devices with channel geometry of 10um X 10um (L x W). A control sample I-V is also shown (black). (c) Calculated carrier densities for all three device generations as a function of channel length. Gen-III devices show the largest values. (d) I-V (log-log) plots of working gen-II devices for channel lengths of 3, 5 and 7um with widths of 100um. (e) A representative I-V (log-log) plot of a 10um long 100um wide gen-III device. The plot shows the representative regions corresponding to SCL transport as well as the fitted lines to the ohmic and quadratic regions. (f) I-V (log-log) plots of gen-III devices with channel geometry of 3um X 100um (L x W).

Four-point measurements taken in a gen-III device after several weeks in air (degraded) are shown in Fig. 54b. These measurements indicate a relatively low sheet resistance of ~2.6 $G\ \Omega/\square$ consistent with prior reports [19]. Prior to degradation we estimate a sheet resistance

of $\sim 5.3\ M\ \Omega/\square$ extracted from the ohmic region. Test devices were also fabricated by transfer of h-BN on top of existing Au metal contacts placed on SiO_2(2um)/Si(p-type) substrates. Electron micrographs of the devices are shown in Figs. 54c, e. These devices were measured before and after placement of the h-BN sheet (Fig. 54d). After placement of the h-BN current increases dramatically and has a clear non-linear trend. Current levels achieved with these test devices are lower than those achieved when the h-BN is properly processed beneath the contacts.

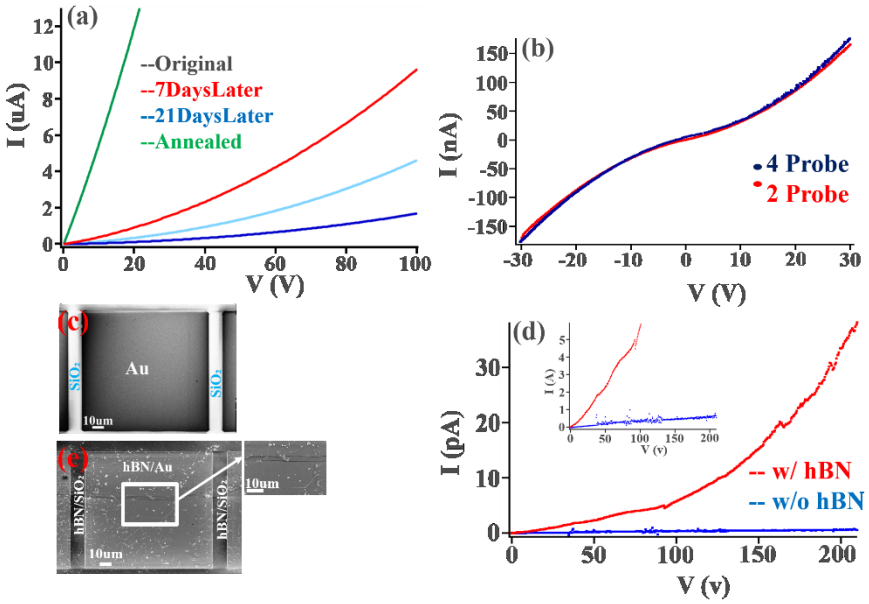

Figure 54 :(a) I-V curves (linear) of a gen-III device tracked over a period of 3 weeks and immediately after annealing. The plot shows the room temp. degradation of this device as well the ability to recover after annealing. (b) 4-probe and 2-probe linear I-V curves of a gen-III device taken after several weeks in air (degraded). The plot shows good agreement between the two measurements indicating that the contact resistance is negligible. (c) SEM micrograph of Au pads prior to transferring hBN on top of them. (d) I-V curves (linear) of a device measured before (blue) and after (red) an hBN monolayer was transferred on top of it. (e) SEM micrograph of Au contact pads after hBN has been transferred on top of them. The inset shows a magnified view of the top of the contact pad where hBN wrinkles and residue is evident.

4 Space Charge analysis

In order to analyze the transport within our devices a typical gen-III device I-V curve is presented in Fig. 53e. In this log-log plot we can observe an ohmic regime at low voltages

accompanied by a transition region at intermediate voltages and a quadratic region at high voltages. This trend has been observed throughout all device generations as shown by the solid lines in Fig. 53b, d, e and is a classic result of space charge limited transport [26]. As the device contacts are relatively low resistance (see Fig. 54b and discussion below) we believe the nonlinearity in the quadratic region is due to space charge limited injection (SCL) of holes into our hBN monolayers**.** We also note that a supra-quadratic region is observed at very high values (V>90v), devices failed shortly after entering this region. The I-V curves are analyzed with a modified form of Mott-Gurney's law appropriate for 2D insulating channels contacted by a strip contact geometry [27]:

$$I = \zeta \epsilon \epsilon_o \mu W \frac{V^2}{L^2} \tag{10}$$

where $\epsilon_o = 8.85X10^{-12}\ (F/m)$, ζ=0.7 for our geometry and ϵ is taken as the average effective dielectric constant of air ($\epsilon_{air} = 1$), SiO2 ($\epsilon_{siO2} = 3.9$) and hBN ($\epsilon_{hBN} = 3 - 4$ [28]). In order to extract mobility values for our devices we fitted appropriate curves in a log-log plot where the current was seen to vary as the square of the voltage and the value of $\frac{I}{V^2}$ was used in conjunction with equation 1 to determine "μ". The carrier density estimation is done by noting the voltage at which the ohmic regime ($I \propto V$) and the quadratic regime ($I \propto V^2$) intersect (labeled "V_x" in Fig. 53e). In the "ohmic region" we take the current to vary as $I = qp_o\mu\frac{W}{L}V$ where p_0 is the equilbrium carrier densitiy in units of cm^{-2}.

The voltage at which this transition occurs determines the onset of SCL behaviour and can be used to estimate the carrier density in the film [26] as given by:

$$p_o = \frac{V_x}{\mathrm{qL}} \epsilon \epsilon_o \xi \tag{11}$$

Using the outlined methods, the mobilities and carrier densities for various devices throughout genI-III were estimated and are presented in Fig. 53a and c. The mobility values for gen-I are ~1x10^{-6} cm^2/Vs while our gen-II devices vary from ~1x10^{-6}~1x10^{-1} cm^2/Vs which is behavior very similar to previously reported values [19]. Our gen-III devices have mobilities that fit well within a window independent of length as shown in Fig. 53a, this behavior is characteristic of long channel devices operating in the non-saturated velocity regime. The mobilities vary from ~5-73 cm^2/Vs. Low mobility values for our 5um devices are attributed to a lower quality film in the region where the devices were fabricated potentially exhibiting tears due to the transfer process or due to the growth as was discussed at the end of Chapter 4. The values obtained in gen-III are more than 3 orders of magnitude larger than those previously reported [19] and our highest performance device exhibits a calculated mobility of 73 cm^2/Vs. To our knowledge this is the highest mobility obtained in any BN monolayer to date [29, 19, 30, 31, 32]. The calculated carrier densities are presented in Fig. 53c where the gen-III values vary from 6*10^{10}-1*$10^{11}$$cm^{-2}$, the largest densities are seen on our 10um devices. The large difference between genI-II and the densities in gen-III can be attributed to the ability to obtain better measurements in gen-III and extrapolate the true doping concentration from the I-V curves.

5 Role of Grain Boundaries in Transport

In the previous section we presented the argument that grain boundaries play a significant role in the conductive properties of hBN. Figure 55 shows SEM imaging accompanied by I-V curves of several working and non-working devices in gen-I and II. It is clear from these images that devices in which a space charge limited I-V curve was measured also present a region in their conductive path free of grain boundaries. Our initial electrode design (gen-I) was modified to the

square pad geometry in order to maximize the probability of obtaining a channel free of grain boundaries. This leads us to conclude that there is a direct correlation between the absence of h-BN grain boundaries in the device current path and achieving high currents which is a phenomenon that has been well documented in III-V semiconductors [33, 34, 35, 36]. Furthermore, Li X. et al. [37] has shown that Gr grain boundaries promote reactions with adsorbates from ambient which can lead to charge trapping in the grain boundary and deteriorate the electrical properties. Kautz et al. [38] has also shown that grain boundaries are major contributors to charge scattering in Gr via Low Energy Electron Microscopy (LEEM) while Koepke et al. [39] came to similar conclusions via STM. First principles quantum transport calculations have also shown that any break in the periodicity of the lattice in a 2D materials can also lead to scattering [39, 40]. The adverse effects of grain boundaries to the electrical properties in 2D materials are well documented and provide a foundation for our theory on these effects on hBN [41, 37, 40, 42].

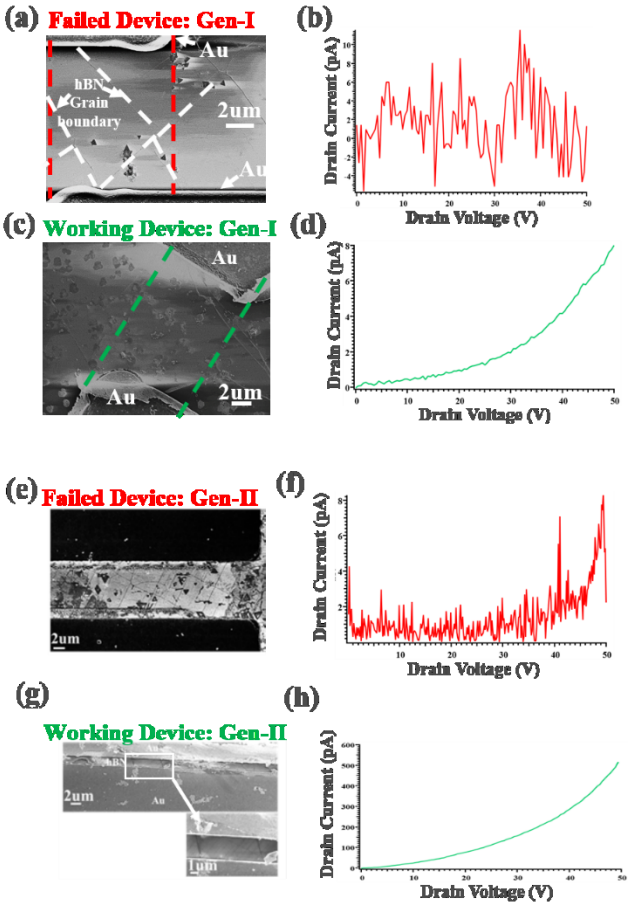

Figure 55 : (a) SEM of conductive path in a non-working device in gen-I. The grain boundaries and channel are outlined and there is no clear path free of grain boundaries in this device. (b) I-V curve of the non-working device presented in S8a. (c) SEM of conductive path in a working device in gen-I. The channel is outlined, and it is evident form the image that no grain boundaries are present in this path. (d) I-V curve of the working device presented in S8c. (e) SEM of conductive path in a non-working device in gen-II. The grain boundaries in the channel are evident and no clear path free of grain boundaries is present in this device. (f) I-V curve of non-working device presented in S8e. (g) SEM of working device in gen-II. The bottom magnified image shows the channel which has an evident region free of grain boundaries. (h) I-V curve of working device presented in S8g.

6 Role of Metal-Semiconductor Interface

We passingly mentioned that Ti/Au contacts were also initially employed but did not work as well as pure Au contact for our two terminal devices. This is in accordance with the devices made using BNNT's by Radosavljevic et al. [30] where they found pure Ni contacts to be superior to Ti/Ni. Looking back at the literature work we have found a possible explanation to this

phenomenon. Titanium (and Ni) is typically used an adhesion layer for most device fabrication including 2D devices. This is because pure Au can many times not be properly patterned with the typical liftoff process used in lithography due to its inferior bonding, thus an intermediate Ti or Ni layer is used. The problem with 2D materials metal contacts is the lack of dangling bonds at the surface which prevents the formation of a strongly bonded metal to the surface of the 2D, thus finding the appropriate metal that can properly bond to a 2D material is quite difficult [43]. A metal-semiconductor (MS) interface for a 2D material typically has a van der Waals (vdW) gap sandwiched in between which not only provides an additional tunneling barrier but also prevents proper contacting. Improper bonding due to the M-vdW-S interface leads to an increased contacts resistance and bad device performance, thus, choosing the appropriate metal contact is critical. Hybridization between atoms of the metal and the 2D surface' out of plane orbitals can lead to strong covalent bonding at the interface and eliminate the vdW gap. This has been shown to occur for Ni on Gr [44], Ti on MoS_2 [45, 46], Pd on WSe_2 [46], and possibly Ni for hBN [47, 48]. As was discussed in Section 2.4.2, Ni has been shown exhibit strong orbital hybridization with hBN (i.e. covalent bonding) [48, 49, 50] which made it a poor catalytic substrate for hBN growth, but, can possibly make it a great choice as a metal contact. According to the work done by Preobrajenski et al. [48, 49] the conditions for strong orbital hybridization between a metal and hBN are:

(i) Good lattice matching to avoid incommensurate states

(i) Unfilled d-orbitals to hybridize with the pi bonds

(i) Good work function alignment to the Valence band

The last condition was imposed by the fact that we have a p-type material and would like to minimize the barrier to injection from the valence band at the MS interface. Figure 56a shows a

small chart outlining what metals meet these conditions and its deduced that Ni and possible Au are good contacts to hBN. We also show in Fig. 56b and c the flat band diagram for a Ni-hBN and Au-hBN interface respectively. Finally, we note that the topic of strong hybridization between Ni and hBN is still debated today with theory contradicting experiments [51] as well experiments themselves contradicting the conclusion of strong bonding [50]. Thus, there is still much work to do regarding the specific surface interaction between a metal and an hBN sheet, however, we can use the conclusions of Fig. 51a from literature to justify that both Ni and Au are suitable contacts for our hBN devices.

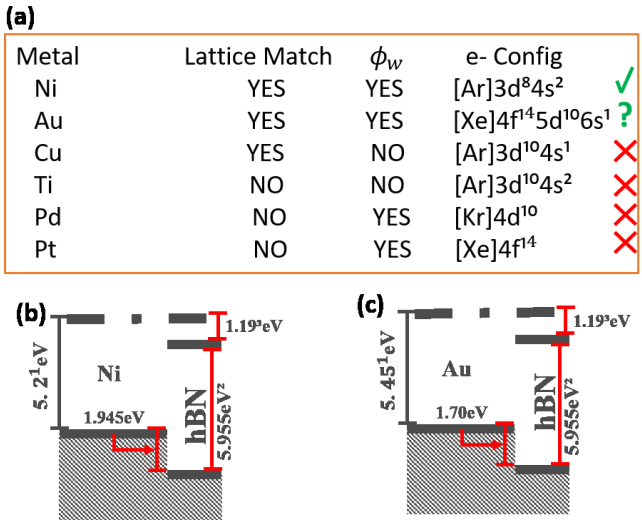

Figure 56 : (a) Table summarizing the metals that meet the conditions for good contacts to 2D hBN. Flat band diagram of (b) Ni-hBN and (c) Au-hBN.

7 Atmospheric Effects on Conduction

Gen-III devices were also tested for their robustness over time where a survey of several devices' I-V curves were tracked over a period of three weeks as shown in Fig. 57. Within this study devices were measured after 1 week in air, after 3 weeks, and just after it was annealed in vacuum. After a few days in air the conductivity of the h-BN dramatically drops (~3 orders of magnitude as mentioned previously). Annealing at 320°C in vacuum (~3uTorr) recovers the

conductivity to values close to the values measured after fabrication. These measurements demonstrate the sensitivity of h-BN devices to ambient conditions, a commonly observed feature in many 2D materials [52, 53, 54]. Sensitivity to ambient has been interpreted in terms of surface transfer doping of the 2D semiconductors by gaseous species [53].

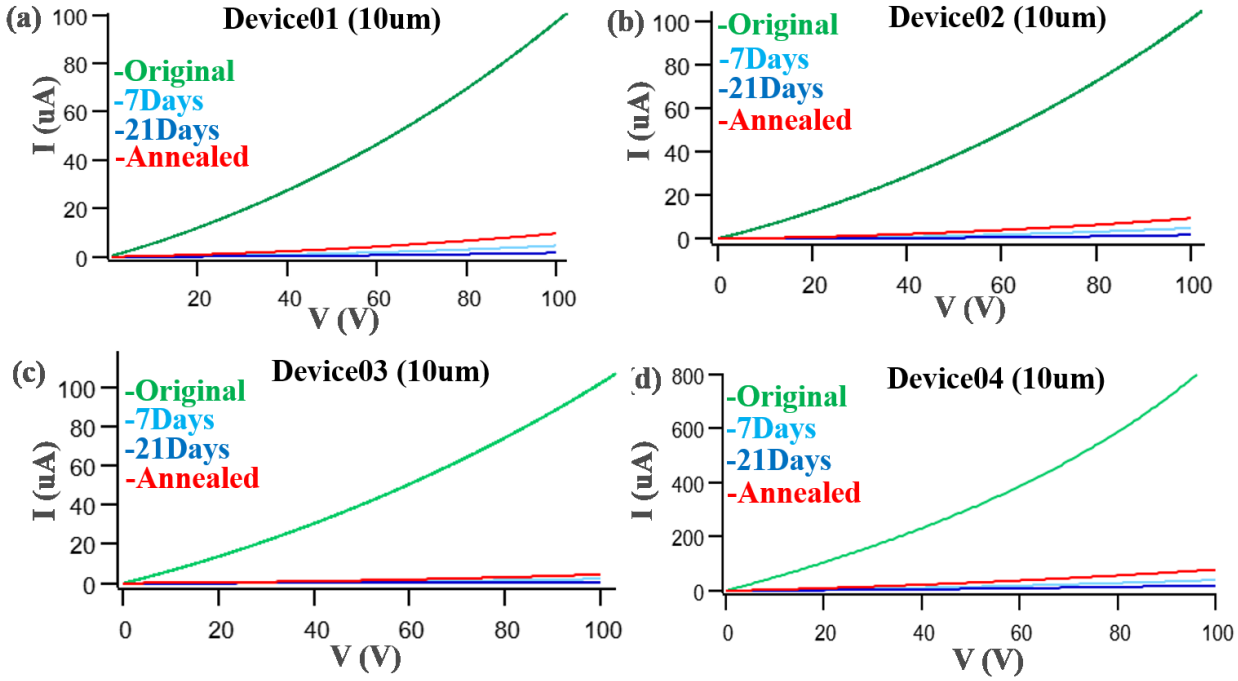

Figure 57 :(a) Linear I-V curves of a 10um channel length devices taken after 7days(light blue), 21days (blue) and after annealing in vacuum at 300°C (red). (b) Linear I-V curves of a 10um channel length devices taken after 7days(light blue), 21days (blue) and after annealing in vacuum at 300°C (red). (c) Linear I-V curves of a 10um channel length devices taken after 7days(light blue), 21days (blue) and after annealing in vacuum at 300°C (red). (d) Linear I-V curves of a 10um channel length devices taken after 7days(light blue), 21days (blue) and after annealing in vacuum at 300°C (red).

8 FET Attempts

Gate voltages up to 40v were applied to the doped Si substrate in order to study the effect of gate biases. No modulation has been observed as can be seen in Figure 58. Figure 58b shows the leakage current through the oxide which is quite low in comparison to the channel current. We note that the devices measured in this experiment were gen-III devices after significant air

degradation (~1month in air) which is why such low current levels were obtained (~nA in Fig. 58a). One of the main reasons this configuration is unlikely to present significant gate modulation is due to the extremely small capacitive coupling present which is mainly due to hBN's large quantum capacitance. Equation 12 can be used to define the quantum capacitance of hBN [55] where the density of states "$D_{hBN}(E)$" has been derived in Appendix B. From this equation we see that its hBN's large effective mass which gives it such a large Quantum Capacitance, this in turn is due to its large bandgap of ~6eV [56] which itself is due to the strong bonding between the Boron and Nitrogen atoms in this 2D material [57, 58]. The capacitance of our oxide used as the gate dielectric (SiO_2) is ~4 orders of magnitude smaller with a value of ~$1.73x10^{-9}(^{F}/_{cm^2})$ as shown in Eq. 13. We assumed an oxide thickness of 2um for this calculation since this is the thickness used in our gen-III devices. Given the capacitive configuration shown in Fig. 59 we expect the smaller capacitance to have a larger voltage dropped across it. Thus, the effective gate voltage dropped across the hBN is actually ~5 orders of magnitude smaller than the applied gate voltage, as shown in Eq. 14, making modulation of the carriers in the channel very difficult unless extremely high voltages are applied which would likely breakdown the oxide. This conclusion informs the next generation of devices where an oxide with a higher permittivity (high-k) should be used in order to obtain modulation. Other methods such as ionic top gating can also be employed to study the field effect in this material [59].

$$C_{hBN}^{q} = q^2 * D_{hBN}(E) = \frac{q^2 g_v m^*}{\pi\hbar^2} \sim 7.8x10^{-5}(^{F}/_{cm^2}) \tag{12}$$

$$C_{SiO_2} = \frac{\epsilon_{SiO_2}\epsilon_o}{t_{SiO_2}} = \frac{(3.9)(8.85x10^{-14})}{2x10^{-4}} \sim 1.73x10^{-9}(^{F}/_{cm^2}) \tag{13}$$

$$V_{hBN} = V_G\left(\frac{C_{SiO_2}}{C_{SiO_2}+C_{hBN}}\right) \sim 2.21x10^{-5} * V_G \tag{14}$$

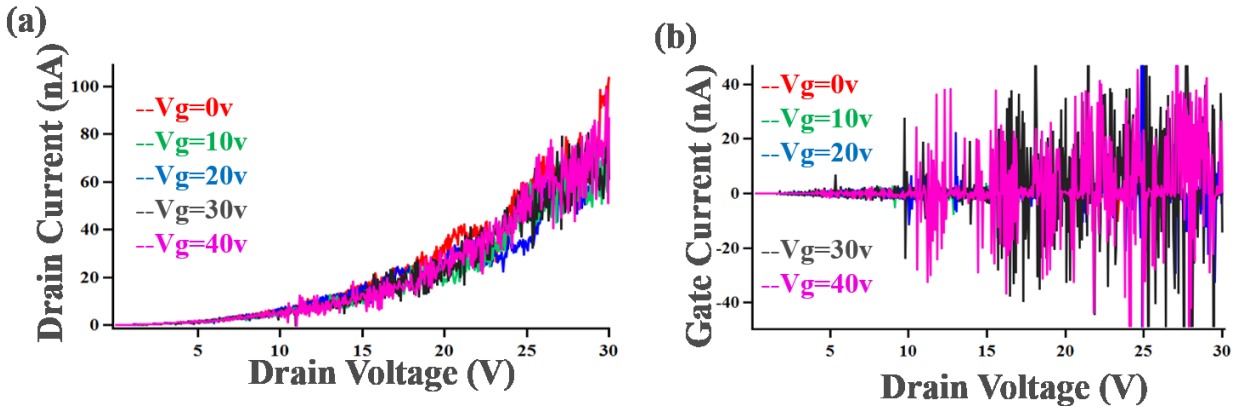

Figure 58 :(a) Drain current as a function of drain voltage for different gate biases up to 40v. (b) Gate (leakage) current as a function of drain voltage for the same measurement done in (a). No gate modulation is evident form these experiments and low gate leakage is found.

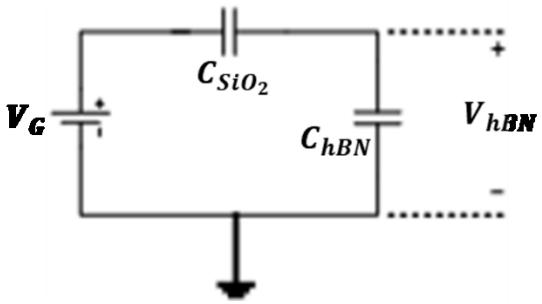

Figure 59 : Capacitive voltage divider formed by the gate oxide (SiO_2) and hBN channel

9 Future Work

With the demonstration a high mobility hBN device that has electrical properties comparable to other mainstream 2D materials many applications are now possible. Our

demonstration of the sensitivity to air exposure opens the possibility of producing hBN based gas sensors. Kahn et al. [60] recently demonstrated that electrodes with surfaces covered by hBN flakes can serve as chemical detectors of dopamine, our devices based solely on hBN monolayers may prove to be efficient in this regard as well. Recent results [61, 62] have demonstrated the potential of using hBN for DUV and neutron detectors. These results were done on insulating hBN where no dark current was observed, however, our conductive layers may prove to be more efficient and have greater applications due to the nature of the space charge [7].

There are many doors that can be opened by making conductive hBN, as a widebangap 2D material it may open the possibility of 2D based power electronics and if gate modulation is achieved, it may lead to a new class of 2D wideband gap transistors.

References

[1] F. Bloch, "On the quantum mechanics of electrons in crystal lattices," *Z. Phys.,* vol. 52, p. 555, 1928.

[2] N. F. Mott and R. W. Gurney, Electronic processes in ionic crystals, Oxford: Clarendon Press, 1940.

[3] A. Rose, "Space charge limited currents in solids," *Physical Reviews,* vol. 97, p. 1538, 1955.

[4] A. Rose, "Photoconductivity in insulators," *RCA Reviews,* vol. 12, p. 303, 1951.

[5] K. W. Boer and U. Kummel, *Z. Phys. Chem. ,* vol. 200, p. 180, 1952.

[6] K. W. Boer and U. Kummel, *Ann. Phys.,* vol. 20, p. 303, 1957.

[7] M. A. Lampert and P. Mark, Current injection in solids, New York: Academic Press, 1970.

[8] V. Coropceanu and a. et, "Charge transport in Organic Semiconductors," *Chemical Reviews,* vol. 107, p. 926, 2007.

[9] R. Dahal and a. et, "Epitaxially grown semiconducting hexagonal boron nitride as a deep ultraviolet photonic material," *Applied Physics Letters,* vol. 98, pp. 211110-1, 2011.

[10] S. Majety and a. et, "Epitaxial growth and demonstration of hexagonal BN/AlGaN p-n junctions for deep ultraviolet photonics," *Applied Physics Letters,* vol. 100, p. 061121, 2012.

[11] S. Majety and a. et, "Electrical transport peroperties of Si doped hexagonal boron nitride," *American Institute of Physics,* vol. 3, p. 122116, 2013.

[12] C. Attacalite and a. et, "Coupling of excitons and defect states in boron nitride nanostructures," *Physical Review,* vol. 83, p. 144115, 2011.

[13] D. Wong and a. et, "Characterization and manipulatoin of individual defects in insulating hexagonal boron nitride using scanning tunnelling microscopy," *Nature Nanotechnology,* vol. 10, p. 949, 2015.

[14] M. Radosavljevic, J. Appenzeller and a. et, "Electircal properties and transport in boron nitride nanotubes," *Applied Physics Letters,* vol. 82, p. 4131, 2003.

[15] H. Zeng and a. et, "White graphene: boron nitride nanoribbons via boron nitride nanotube unwrapping," *NanoLetters,* vol. 10, p. 5049, 2010.

[16] L. Song and a. et, "Large scale growth and characterization of atomic hexagonal boron nitride," *Nanoletters,* vol. 10, p. 3209, 2010.

[17] F. Mahvash and a. et, "Space charge limited transport in large area monolayer hexagonal boron nitride," *NanoLetters,* vol. 15, p. 2263, 2015.

[18] D. A. Laleyan and et al, "AlN/hBN heterostructure for Mg dopant free ultraviolet photonics," *ACS Nanoletters,* vol. 17, p. 3738, 2017.

[19] F. Mahvash, E. Paradis, D. Drouin, T. Szkopek and M. Siaj, "Space charge limited transport in large area monolayer hexagonal boron nitride," *Nano Letters,* vol. 15, pp. 2263-2268, 2015.

[20] G. L. Snider, "1D Poisson," [Online]. Available: https://www3.nd.edu/~gsnider/.

[21] R. V. Gorbachev and a. et, "Hunting for monolayer boron nitride: optical and raman signatures," *Small,* vol. 7, p. 465, 2011.

[22] A. G. F. Garcia, M. Neumann, F. Amet, J. R. Williams, K. Watanabe, T. Taniguchi and D. Goldhaber-Gordon, "Effective cleaning of hexagonal boron nitride for graphene devices," *Nano Letters,* vol. 12, pp. 4449-4454, 2012.

[23] Y. Chen, X.-L. Gong and J.-G. Gai, "Progress and challenges in transfer of large area graphene films," *Advanced Science,* vol. 3, p. 1500343, 2016.

[24] Y.-C. Lin, C.-C. Lu, C.-H. Yeh, C. Jin, K. Suenaga and P.-W. Ciuh, "Graphene annealing: how clean can it be?," *Nano letters,* vol. 12, p. 414, 2012.

[25] W. Choi, S. Arslan, S. Park and Y. Seo, "Influence of removing PMMA residues on surface of CVD graphene using a contact mode AFM," *RSC Advances,* vol. 7, p. 6943, 2017.

[26] M. A. Lampert and P. Mark, Current injection in solids, Princeton: Academic Press, 1970.

[27] A. A. Grinberg, S. Luryi, M. R. Pinto and N. L. Schryer, "Space charge limited current in a film," *IEEE transactions,* vol. 36, pp. 1162-1170, 1989.

[28] C. R. Dean, A. F. Young, I. Meric, C. Lee, L. Wang, S. Sorgenfrei, K. Watanabe, T. Taniguchi, P. Kim, K. L. Shepard and J. Hone, "Boron nitride substrates for high-quality graphene electronics," *Nature Nanotechnology,* vol. 5, pp. 722-726, 2010.

[29] G.-H. Lee, Y.-J. Yu, C. Lee, C. Dean, K. L. Shepard, P. Kim and J. Hone, "Electron tunneling through atomically flat and ultrathin hexagonal boron nitride," *Applied Physics Letters,* vol. 99, p. 243114, 2011.

[30] M. Radosavljevic, J. Appenzeller, V. Derycke, R. Martel, P. Avouris, A. Loiseau, J.-L. Cochon and D. Pigache, "Electrical properties and transport in boron nitride nanotubes," *Applied physics letters,* vol. 82, p. 4131, 2003.

[31] H. Zeng, C. Zhi, Z. Zhang, X. Wei, X. Wang, W. Guo, Y. Bando and D. Goldberg, "White Graphene: Boron nitride nanoribbons via boron nitride nanotrube unwrapping," *Nano Letters,* vol. 10, pp. 5049-5055, 2010.

[32] D. A. Laleyan, S. Zhao, S. Y. Woo, H. N. Tran, B. H. Le, T. Szkopek, H. Guo, G. A. Botton and Z. Mi, "AlN/hBN heterostructures for Mg dopant free depp ultraviolet photonics," *NanoLetters,* vol. 17, p. 3738, 2017.

[33] C. Grovenor, "Grain boundaries in semiconductors," *Journal of Physics C,* vol. 18, no. 21, p. 4079, 1985.

[34] G. Blatter and F. Greuter, "Carrier transport through grain boundaries in semiconductors," *Physical Review B,* vol. 33, no. 6, p. 3952, 1985.

[35] M. Spencer, W. J. Schaff and D. K. Wagner, "Electrical characterization of grain boundaries in GaAs," *Journal of Applied Physics,* vol. 54, p. 1429, 1983.

[36] M. Spencer, R. Stall, L. F. Eastman and C. E. Wood, "Characterization of grain boundaries using deep level transient spectroscopy," *Journal of Applied Physics,* vol. 50, p. 8006, 1979.

[37] X. Li and a. et, "Graphene films with alrge domain size by a two step chemical vapor deposition process," *NanoLetters,* vol. 10, p. 4328, 2010.

[38] J. Kautz and a. et, "Low energy electron potentiometry: Contactless imaging of charge transport on the nanoscale," *Scientific Reports,* vol. 5, p. 13604, 2015.

[39] P. Y. Huang and a. et, "grains and grain boundaries in single layer graphene atomic patchwork quilts," *Nature,* vol. 469, p. 389, 2011.

[40] O. Yazyev and a. et, "Electronic transport in polycrystalline graphene," *Nature Materials,* vol. 9, p. 806, 2010.

[41] Q. Yu and a. et, "Characterization of individual grains and grain boundaries in graphene grown by chemical vapor deposition," *Nature Materials,* vol. 10, p. 443, 2011.

[42] A. W. Tsen and a. et, "Tailoring electrical transport across grain boundaries in polycrystalline graphene," *Science,* vol. 336, p. 1143, 2012.

[43] A. Allain, J. Kang, K. Banerjee and A. Kis, "Electrical contacts to two dimensional materials," *Nature Materials,* vol. 14, p. 1195, 2015.

[44] K. Stokbro and a. et, "Atomic scale model for the contact resistance of the nickel graphene interface," *Physical Review B,* vol. 85, p. 165442, 2012.

[45] J. Kang and a. et, "A computational study of metal contacts fo beyond graphene 2D semiconductor materials," in *IEEE International Electron Devices Meeting*, Pennsylvania, 2012.

[46] I. Popov and a. et, "Designing electrical contacts to MoS2 monolayers: a computational study," *Physical Review Letters,* vol. 108, p. 156802, 2012.

[47] J. G. Diaz and a. et, "Hexagonal boron nitride on transition metal surfaces," *Theoretical Chemistry Accounts,* vol. 132, p. 1350, 2013.

[48] A. B. Preobrajenski and a. et, "Monolayer of hBN chemisorbed on Cu(111) and Ni(111): The role of the transition metal 3d states," *Elselvier,* vol. 582, p. 21, 2005.

[49] A. B. Preobrajenski and a. et, "Ni 3d-BN pi hybridization at the hBN-Ni (111) interface observed with core level spetroscopies," *Physical Review B,* vol. 70, p. 165404, 2004.

[50] A. Nagashima and a. et, "Electronic structure of monolayer hexagonal boron nitride physisorbed on metal surfaces," *Physical Review Letters,* vol. 75, p. 3918, 1995.

[51] G. B. Grad and a. et, "Density functional theory investigation of the geometric and spintronic structure of hBN-Ni(111) in view of photoemission and STM experiments," *Physical Review B,* vol. 68, p. 085404, 2003.

[52] F. Schedin, A. K. Geim, S. V. Morozov, E. W. Hill, P. Blake, M. I. Katsnelson and K. S. Novoselov, "Detection of individual gas molecules adsorbed on graphene," *Nature Materials,* vol. 6, pp. 652-655, 2007.

[53] V. Panchal, C. E. Giusca, A. Lartsev, N. A. Martin, N. Cassidy, R. L. Myers-Ward, D. K. Gaskill and O. Kazakova, "Atmospheric doping effects in epitaxial graphene: correlation of local and global electrical studies," *2D Materials,* vol. 3, no. 1, p. 015006, 2016.

[54] G. Mirabelli, C. McGeoug, M. Schmidt, E. K. McCarthy, S. Monaghan, I. M. Povey, M. Melissa, F. Gity, R. Nagle, G. Hughes, A. Cafolla, P. K. Hurley and R. Duffy, "Air sensitivity of MoS2, MoSe2, MoTe2, HfSe and HfSe2," *Journal of Applied Physics,* vol. 120, p. 125102, 2016.

[55] S. Datta, Quantum Transport, New York: Cambridge University Press, 2005.

[56] G. Cassabois, P. Valvin and B. Gil, "Hexagonal boron nitride is an indirect bandgap semiconductor," *Nature Physics,* vol. 10, p. 262, 2015.

[57] J. Robertson, "Electronic stucture and core exciton of hexagonal boron nitride," *Physical Review B,* vol. 29, no. 4, p. 2131, 1984.

[58] R. M. Ribeiro and N. M. Peres, "Satbility of boron nitride bilayers," *Physical Review B,* vol. 83, p. 235312, 2011.

[59] F. Chen, . Q. Quang, J. Xia, J. Li and N. Tao, "Electrochemical gate controlled charge transport in graphene in ionic liquid and aqueous solution," *Journal of the American Chemical Society,* vol. 29, p. 131, 2009.

[60] A. F. Khan and a. et, "2D hexagonal boron nitride explored for the electrochemical sensing of dopamine," *Analytical chemistry,* vol. 88, p. 9729, 2016.

[61] K. Ahmed and a. et, "Growth of hexagonal boron nitride on (111) Si for deep UV photonics and thermal neutron detection," *Applied Physics Letters,* vol. 109, p. 113501, 2016.

[62] T. C. Doan and a. et, "Growth and decices processing of hexagonal boron nitride epilayers for thermal neutron and deep ultraviolet detectors," *American Institute of Physics,* vol. 6, p. 075213, 2016.

VI. Conclusions

In this manuscript we have shown how proper engineering and analysis can lead to the optimized growth of single crystal hBN sheet on the mm scale. The achievement of this feat for hBN is extremely important since it opens the doors to the production and applications of technology relevant devices where the role of grain boundaries and defects is minimized. As an example, is the fabrication of a BisFET proposed by Banerjee et al. [1] which takes advantage of the formation of Bosons between two closely spaced Gr layers separated by a few layers of hBN. This theoretical device can be easily switched on and off with very low applied voltages and can form the basis for CMOS logic based on 2D materials. The formation of Bosons in this device takes place when the carrier densities of the top and bottom Gr layer are very close to each other. It has been show that grain boundaries or other defects in hBN can lead to unintended doping of Gr which would prevent Boson formation, thus, the production of high quality defect free hBN layers may prove crucial in demonstrating a 2D based logic circuits.

With regards to our results on the electrical conduction of our hBN sheets there is a concern that CVD grown hBN may not be useful as an insulating layer for 2D devices. Furthermore, many researchers may ask whether or not exfoliated hBN may suffer from these p-type doping effects leading to leakage currents. With regards to the second point, we note that exfoliated hBN is typically isolated from samples produced at very high temperatures and pressures [2]. Since this exfoliated material has been used extensively in the field with no reports of its conduction we believe that the defects (B vacancies) which enable p-type conduction are likely unstable at these conditions and do not form in the HPHT hBN. The situation is more complicated for CVD hBN. Our experimental results have shown very low yields with regards to tested devices where only ~10-20/100 devices worked. We've argued that both tearing, and grain boundaries play a role in

this yield. Thus, if experimenters would like to ensure the production of insulating hBN, small grains (large density of grain boundaries) are preferred. Furthermore, even in our large single crystal based devices we still had trouble getting conductive channels from one growth to another. This means that the formation of these defects is likely restricted to a small processing window and most CVD hBN is insulating. The complete study of the formation of these defects and their implications in the optical and electronic properties of hBN is an ongoing field of study as mentioned in the Introduction of Chapter 1.

Finally, hBN has recently proven to be a very interesting 2D material with applications in single photon emission, thermal transport and UV detection amongst other. The applicability and study of this material in these fields will greatly benefit from the facile production of large single crystal monolayers similar to what happened when Gr reached mm sized grains. We hope that our work will enable deeper fundamental studies on the defect structures in hBN which will lead to a better understanding of the overall physics and engineering of this material.

References

[1] S. K. Banerjee and a. et, "bilayer pseudospin field effect transistor (BiSFET): A proposed new logic device," *IEEE electron device letters,* vol. 30, p. 158, 2009.

[2] K. Wantanabe, T. Taniguchi and H. Kanda, "Direct bandgap properties and evidence for ultraviolet lasing of hexagonal boron nitride single crystal," *Nature Materials,* vol. 3, p. 404, 2004.

Appendix A. : Zero Dimensional Analysis of CVD System

Although we mentioned at the beginning of chapter 3 that modeling of our hBN growth was futile since we couldn't measure the precise concentrations of our precursor, there are several other

parameters which we do have that can be useful in analysis. In our analysis there are various simplifications and assumptions that will be made in order to gain the most amount of insight at the least mathematical expense, these are:

(i) T=1000°C

(ii) P=1 torr ; when possible comparisons to 760torr will be made.

(iii)An input flow of 100sccm is assumed.

(iv)Gases are H_2 and Borazine only.

(v) The surface rate constants for Cu and Ni are assumed to be within 0<Ks<490.

(vi)A differential reactor will be assumed at low pressures.

(vii) A constant surface area for reaction of S=2x6cm² will be used. This is the maximum amount of Cu foil that can be inserted into the chamber to remain within the flat zone.

Point v needs to be addressed in order to understand why the upper limit is set on ks. The surface reaction rate of a catalyst defines the rate at which species will be consumed at the surface and catalyzed into a crystal. This values essentially describes how good of a catalyst a particular metal is. It also defines the consumption time of the gaseous species being catalyzed, borazine in our case. The equations defining residence time and consumption time are shown below:

$$t_{res} = \frac{V(cm^3)}{F_{in}(cm^3/s)} \quad \text{(A)}$$

$$t_{con} = \frac{V(cm^3)}{K_s(cm^2/s)S(cm^2)} \quad \text{(B)}$$

The volume of the tube is calculated from Fig. 13 to be V~5.174*$10^3 cm^3$. The input flow of 100sccm needs to be adjusted for changes in temperature and volume, this can be easily done

using the ideal gas law:

$$Fin(1000°C, 760torr) = \left(\frac{100}{60}\right) * \left(\frac{1273}{273}\right)(cm^3/s) = 7.79(cm^3/s) \quad \text{(C)}$$

$$Fin(1000°C, 1torr) = \left(\frac{100}{60}\right) * \left(\frac{760}{1}\right) * \left(\frac{1273}{273}\right)\left(\frac{cm^3}{s}\right) = 5.92 * 10^3(cm^3/s) \quad \text{(D)}$$

As can be seen the pressure is what makes the largest difference with regards to volumetric flow. Now that we have all the variables needed to find the residence and consumption times we plot their ratios in Fig. A1a-b. As we can see in Fig A1a, at 760torr and 1000°C the consumption time is essentially always equal to or greater than the residence time, thus APCVD is always non-differential and our zero dimensional analysis doesn't apply. Fig. A1b shows the same ratio only at 1000°C and 1torr (LPCVD), at these pressures the consumption time is comparable to the residence time at ks~492, thus, for all other values of ks<492 our zero dimensional model applies and we can assume that very little reactive gases are consumed during growth so that effectively Fin~Fout. This is also justified in that our growth times are quite large (>30min) which are typical of a low ks catalyst. Since no one has actually reported values of ks for either Cu or Ni for hBN growth, our upper limit of 492 will have to be enough to proceed with the analysis.

A small digression is necessary here to establish the way in which ks could be extracted for a particular growth system. Since ks is exponential with temperature, then at low temperatures we would expect it to be very small and thus tcon>>tres, this would put us in the surface limited regime and the growth rate is exponential with temperature. As we increase the temperature ks increases rapidly and tcon starts to approach tres until eventually tcon>tres, at this point we are in the transport limited regime and the growth rate is now independent of temperature. Thus, a plot of the growth rate as a function of temperature, or rather, inverse temperature would give us an estimate of ks. This is well known technique in chemistry and materials science and the plot is called an "Arrenhius" plot (after the fellow that came up with it). Unfortunately, plotting the

growth rate requires knowledge of the precursor concentration which we don't have. This is why using gaseous sources for growth is so valuable, with enough work all the parameters can be well established and the growth can be controlled and reproducible to even the monolayer limit, alas, until non-toxic boron sources are found, this is but a pipedream for hBN CVD.

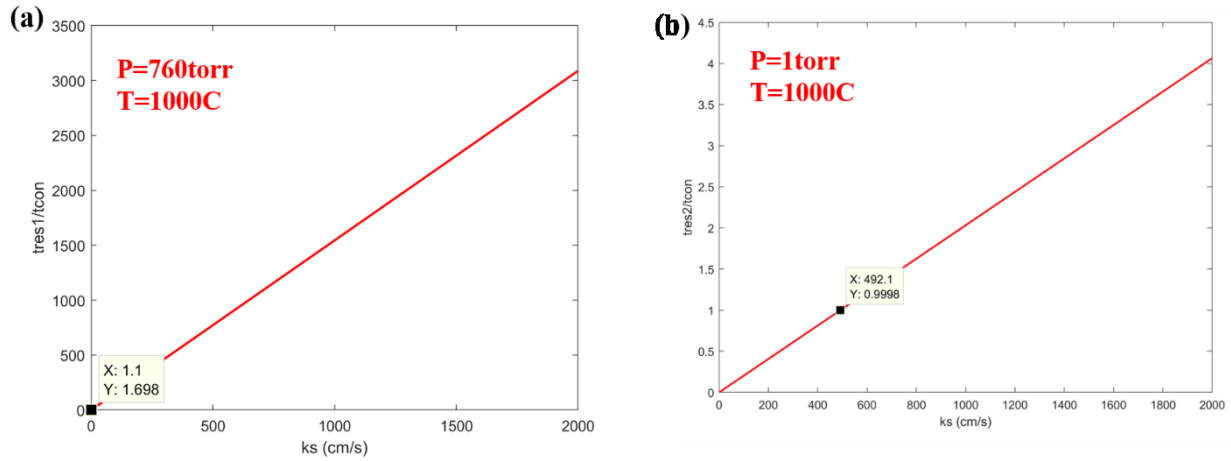

Figure A 1 : (a) Ratio of residence time and consumption time at 760torr and 1000°C as a function of the surface rate constant ks. The point where the ratio is unity is depicted in the plot and occurs for a value of ks=1.1. (b) Ratio of residence time and consumption time at 1torr and 1000°C as a function of the surface rate constant ks. The point where the ratio is unity is depicted in the plot and occurs for a value of ks=492.

Now that we've established the parameters under which our zero-dimensional model will apply we can continue to further study the growth within LPCVD. The binary diffusion coefficient (D_{BD}) of our constituent gases need to be determined in order to find the diffusion length of the mixture. Historically binary diffusion coefficients are quite complex since estimates of scattering cross section and molecular potentials amongst other variables are non-trivial. Many simplified approaches have been deduced over the years and one of the most commonly used approaches to approximating D_{BD} is the one proposed by Fuller et al. [1]:

$$D_{BD} = \frac{1.08 * T^{1.75}}{P M_{eff}^{1/2} [\Sigma_{BZ}^{1/3} + \Sigma_{H2}^{1/3}]^2} \quad \text{(E)}$$

$$M_{eff} = \frac{2}{{}^{1}/_{M_{BZ}} + {}^{1}/_{M_{H2}}} \quad \text{(F)}$$

Where P is the pressure in torr, T is the temperature in Kelvin, Meff is the average mass of the constituent gases given by (F and Σ is the effective volume in cm3 of the gas molecules. All of these values except for the effective volumes are readily available and tabulated in various sources [2, 3, 1]. Fuller gives the effective volume of a hydrogen molecules as $\Sigma_{H2} = 6.1$ cm^3, however in order to find the effective volume for borazine we may use an approximate method since its effective volume is not listed. For borazine we first look up the density of its liquid form in g/cm^3 and then divide by the molecular weight in g/mol, this value will give the molar volume in cm^3/mol as shown below:

$$V_{BZ} = \left(\frac{\rho_{BZ}^{l}}{M_{BZ}}\right)^{-1} = \left(\frac{0.81\frac{g}{cm^3}}{80.5\frac{g}{mol}}\right)^{-1} \sim 99.4\ (cm^3/mol) \quad \text{(G)}$$

Now we use an approximation to the gaseous effective volume given by Ref. [3]:

$$\Sigma_{BZ} = -12.7 + 1.14 * V_{BZ} \quad \text{(H)}$$

For borazine we have $\Sigma_{BZ} = 100.6$ cm³/mol. Armed with these parameters we may estimate the binary diffusivity of our gaseous mixture of borazine and H_2 as shown in Fig. A2 below. The temperature was taken to be 1000°C. Fig. A2 shows that the pressure greatly affects the diffusivity by at least three orders of magnitude! This in turn will increase our diffusion length defined by:

$$L_D = \sqrt{4 D_{BD} t_{res}} \quad \text{(I)}$$

Error! Reference source not found.Error! Reference source not found.Error! Reference sou rce not found.

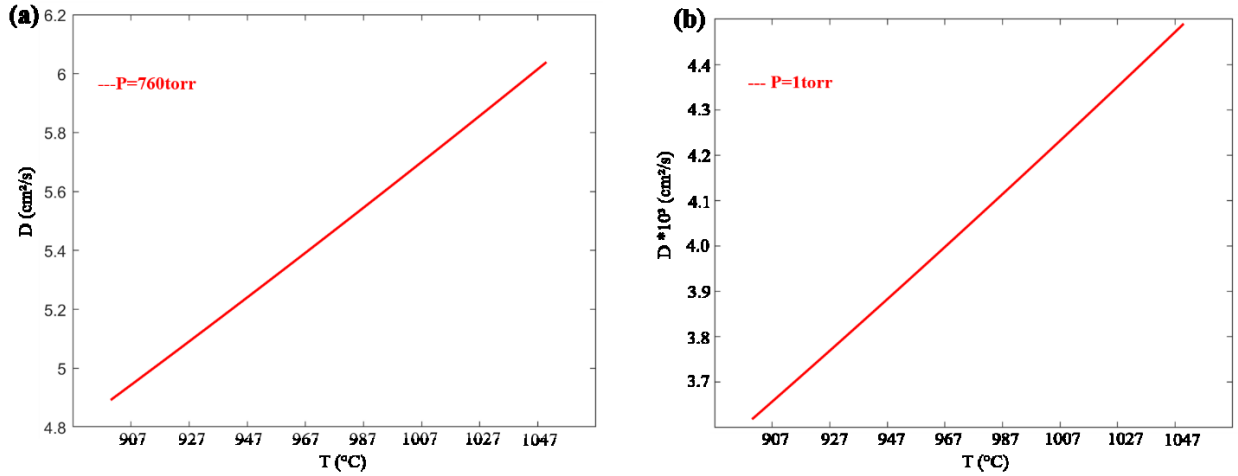

Figure A 2 : (a) Binary diffusion coefficient of borazine H_2 mixture as a function of temperature at 760torr. (b) Binary diffusion coefficient of borazine H_2 mixture as a function of temperature at 1torr.

For our purposes we will take tres~0.874s which is estimated using F(1000°C, 1torr) and the volume of our CVD tube (V~5e3cm³). Finding the corresponding $D_{BD}(1000°C, 1torr)$~4080 (cm²/s) gives L_D~120 cm. This length is comparable to the length of our tube (180cm) but much large than its radius (3cm). Thus, growth in the radial direction is not strongly affected by the diffusion of the species within the tube and is dominated by the kinetics at the surface (i.e. mass transport limited). Along the length of the tube diffusion is significant, but in order to verify if its dominant we can calculate the Peclet number along the length of the tube defined by:

$$P_e = \left(\frac{L}{L_D}\right)^2 \quad \text{(J)}$$

We find Pe~2.3, this is not a large number and along the length we're essentially in diffusive equilibrium, meaning that large gradients in concentration are unlikely. For the case of diffusive equilibrium the Peclet number can also be defined as the ratio of advective diffusion to

simple diffusion (i.e. diffusion promoted by concentration gradients). Thus, along the tube length advective diffusion is dominant.

Lastly, we can ask a more involved question regarding our system, this is, what will happen to the growth at the surface of the Cu foil within the hot zone? Before delving into this problem, we must ask if laminar flow is prevalent or if turbulent flow is dominant. To this end we can calculate the Reynolds number which is a measure of the turbulence of fluid flow and given by:

$$R_e = \frac{U*L}{\upsilon} \qquad \text{(K)}$$

Where U=L/tres is the average velocity of the gases in the system, L is the system length (~813cm) and υ is the kinematic viscosity of the gaseous mixture. For our system we have U~183/0.874~209 (cm/s). Since during growth the gaseous mixture is mostly H2 we need only determine the kinematic viscosity of H2 at our operating point. Using a tabulated value we find $\upsilon = 1824$ (cm^2/s) [2]. Thus, plugging numbers into Eqtn. (K we find Re~21. This is a low Re and given our pressures and flow velocities its safe to say that our flow is quite laminar.

As a reference, its generally accepted that Re's in the hundreds lead to circulation currents and Re's in the thousands lead to full turbulence [4]. However in some texts one also encounters the argument that any Re's on the order of 10's (our case) will give rise to stable re-circulations [3]. The argument of what the ranges of Re correspond to and what value or Re actually lead to the onset of turbulence is as old as Reynolds himself [5]. It was believed that turbulence arises from an increase in temporal complexity (the evolution as a function of time of something, this view is ascribed to Landau, Ruelle and Takens) and would eventually become stable at sufficiently long time scales [4]. However, it wasn't until recently that Avila et al. [6] demonstrated that it was instead the notion of spatial coupling that determines the onset of turbulence. The showed that

at Re<2040 (+/-10) circulation (if they exist in the fluid) are unstable and decay leaving the flow laminar, above this Re circulation currents spread and duplicate (much like the concept of zener breakdown actually) leading to turbulent flow being dominant. Thus, for our Re~20 even if circulation currents exist, they rapidly decay and its safe to assume that laminarity is dominant in our system.

Lastly, we must ask whether our gas behaves as a continuous media or independent molecules. In other words we must ask whether the gas is dense enough at our low pressures that collisions are more frequent between the gas molecules than with the chamber walls. The ratio of the mean free path to the chamber diameter (D) will tell us in what regime we are in and is called the Knudson number:

$$K_n = \frac{\lambda_{mfp}}{\square} \tag{L}$$

$$\lambda_{mfp} = \frac{RT}{\sqrt{2}\pi d^2 N_A P} \tag{M}$$

Where λ_{mfp} is the mean free path and N_A is Avogadro's number. For our assumption of mostly H2 at 1torr we find λ_{mfp}~3.56*10^{-2}cm and given our tube diameter of D=6cm we have Kn~0.006. This puts well within the viscous flow regime (Kn<0.01) and all our assumptions are valid.

Our simplified model that we'll be using is shown in Fig. A3 where we have advective laminar viscous flow in the x direction promoted by adjective diffusion and simple diffusion in the y direction. This is a more difficult problem since we've allowed both adjective and simple diffusion to occur within the system in two different directions (Jx and Jy), but have simplified it by estimating which component of diffusion is dominant in either direction.

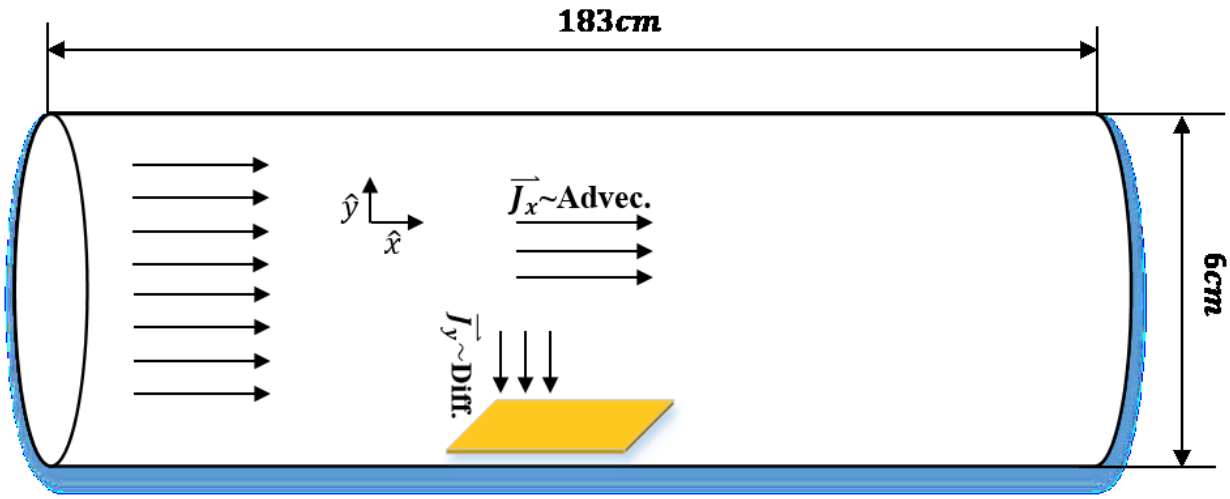

Figure A 3 : CVD system model for a Borazine H2 mixture using the simple zero dimensional plug flow model.

The model presented in Fig. A3 is called a zero dimensional plug flow model and is frequently used at larger scales to model 1st order behaviors in CVD systems. Armed with this model we may now ask the important question: "will the diffusion of reactants be surface limited or mass transport limited at the Cu surface?". The answer to this is the Damkohler number which measures the rate at which species are consumed at a catalyst surface within adjective diffusion. Its given by:

$$D_k = \frac{k_s D}{D_{BD}} \qquad \text{(N)}$$

Where ks is the surface reactivity of Cu, D is the tube diameter and Dbd is the binary diffusion coefficient for our gas mixture which we've already calculated. The Damkohler number as a function of ks and temperature is plotted in Fig. A4 for several temperatures. The green shaded are in the lower left is the area within which our growth is surface limited and is valid for roughly ks<490 which is our upper limit for the Cu reaction rate! If it turns out Cu has a large reaction rate constant then our growth is mass transport limited and non-uniform along the x direction.

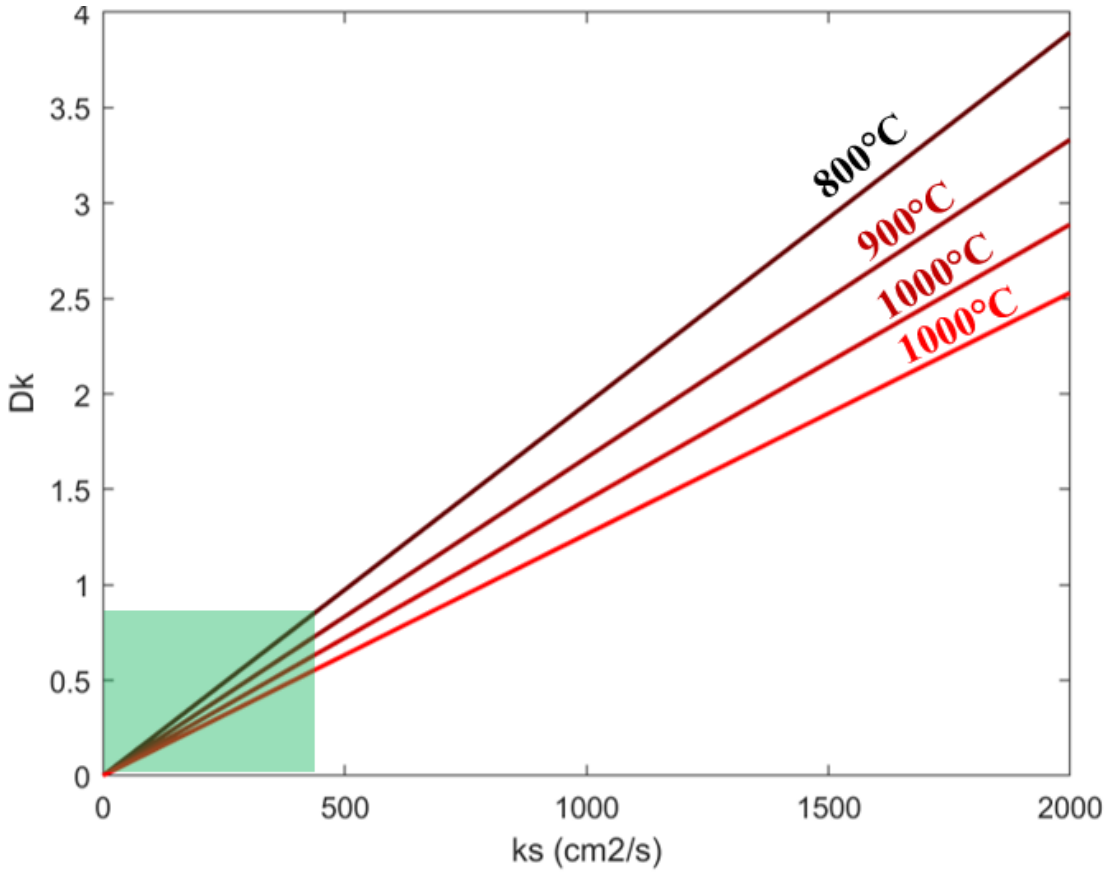

Figure A 4 : Plot of the Damkohler number for various temperature ranges as a function of the catalyst surface reaction rate constant.

With these simple approximations we have made some very powerful conclusions, most importantly we've established that within certain parameters we can obtain a surface limited growth which will give us uniform growth along the length of the system. This is what CVD growth aims for and its why LPCVD is superior to APCVD, uniform growths at atmospheric pressures are unlikely and more difficult optimizations and models are necessary.

References

[1] B. E. Poling, J. M. Prauznitz and J. P. O'Connel, The properties of gases and liquids, New York: McGraw Hill, 2001.

[2] J. A. Dean, Lange's Handbook of Chemistry, New York: McGraw-Hill, 1999.

[3] D. M. Dobkin, Principles of Chemical Vapor Deposition, San Jose: WJ communications, 2006.

[4] L. D. Landau and E. M. Lifshitz, Fluid Mechanics, New York: Peramon Press, 1959.

[5] O. Reynolds, "An experimental investigation of the circumstances which determine whether the motion of water shall be direct or sinous and the law of resistance in parallel channels," *Philosophical Transactions of the Royal Society of London,* vol. 174, p. 935, 1883.

[6] K. Avila and a. et , "The onset of turbulence in pipe flow," *Science,* vol. 333, p. 192, 2011.

Appendix B. : Tight Binding Model for hBN

In order to determine the Fermi level position as a function of our dopant concentration in our gen-III devices the electronic band structure and density of states (D(E)) was calculated using tight binding. Our procedure closely follows the methodology given in Chp. 5 of [1]. A sublattice formed of rectangular unit cells composed of two atoms (Boron and Nitrogen) was used since the original hexagonal lattice is not periodic. This lattice is shown in green rectangles in Fig. A5.

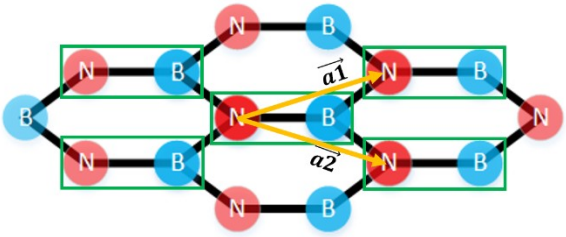

Figure A 5 : A depiction of an hBN hexagonal lattice showing the sublattice (green rectangles) used for the band structure calculations as well as the primitive vectors (orange arrows).

The primitive vectors are defined as $\overrightarrow{a1} = 1.5a_o\hat{x} + \frac{\sqrt{3}}{2a_o}\hat{y} = a\hat{x} + b\hat{y}$; $\overrightarrow{a2} = 1.5a_o\hat{x} - \frac{\sqrt{3}}{2a_o\hat{y}} = a\hat{x} - b\hat{y}$ where $a = 3a_o/2$ & $b = \sqrt{3}a_o/2$.

We've used a_o=0.144nm as the interatomic distance between the boron and nitrogen atoms [2]. For the tight binding calculation only the $2p_z$ orbitals were taken into account since the 2s, $2p_x$ and $2p_y$ orbitals do not contribute to the electronic properties [1]. Using these orbitals as the

basis per unit cell the tight binding Hamiltonian may be written as:

$$\left[H(\vec{k})\right] = \begin{bmatrix} \epsilon_B & h_o(\vec{k}) \\ h_o(\vec{k})^* & \epsilon_N \end{bmatrix} \quad (O)$$

Where we've defined $h_o(\vec{k}) = t[1 + e^{i\vec{k}.\vec{a_1}} + e^{i\vec{k}.\vec{a_2}}]$ and used the tight binding parameters:

t=2.92 ; Overlap integral value of the $2p_z$ Boron and Nitrogen atoms [3].

$\epsilon_B = 4.78eV$; $2p_z$ orbital energy of the Boron atom [3].

$\epsilon_N = -1.12eV$; $2p_z$ orbital energy of the Nitrogen atom [3].

The dispersion relation is obtained by diagonalizing Eq. A where we've simplified the final result by taking small values of $|\vec{k}|$ near the band minima at the K and K' valleys by means of a Taylor expansion:

$$E(k_x, k_y) = (A \pm B) \pm a^2t^2/B\,[k_x^2 + (k_y \mp 2\pi/3b)^2] \quad (P)$$

Where $A = (\epsilon_B + \epsilon_N)/2$ & $B = (\epsilon_B - \epsilon_N)/2$.

Using the result of Eq. B one can obtain an expression for the effective mass of electrons and holes as well as the density of states within the bands:

$m^* = \hbar^2\left[\partial^2 E/\partial k_x \partial k_y\right]^{-1}$ Effective mass for a 2D structure [1] (Q)

$D(E) = \frac{g_v g_s m^*}{2\pi\hbar^2}$; Density of states for a 2D structure [1] where g_s & g_v are the spin and valley degeneracies respectively. (R)

From Eq. C we find that $m^* = 0.5m_o$ for hBN where m_o is the free electron mass. The 2D electron and hole densities can be calculated from:

$$n(E) = \int_{E_c}^{\infty} D(E)f(E)dE = (g_v m^* kT/\pi\hbar^2)\left[ln\left(1 + exp\left(\frac{Ec-Ef}{kT}\right)\right) - \frac{Ec-Ef}{kT}\right] \quad (S)$$

$$p(E) = \int_{-\infty}^{e_v} D(E)(1 - f(E))dE = (g_v m^* kT/\pi\hbar^2)\left[ln\left(1 + exp\left(\frac{Ev-Ef}{kT}\right)\right) - \frac{Ev-Ef}{kT}\right] \quad (T)$$

Where we've made use of the fermi function in the form:

$$f(E) = \frac{1}{1+e^{(E-E_F)/kT}} \quad (U)$$

The resulting electron and hole densities as a function of the fermi level are plotted in Fig. A 6 where we've included the range of energies (shown in the green band) where the Fermi level must lie in our gen-III devices in order to obtain the calculated hole doping densities of ~[0.5-1]x$10^{11}cm^{-2}$, namely this is ~120-150meV above the valence band edge.

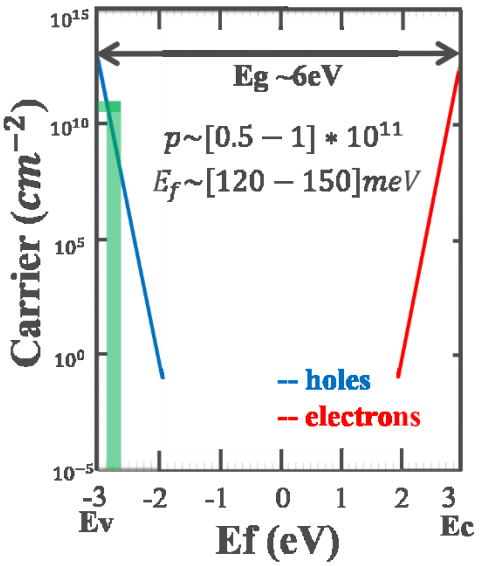

Figure A 6 : A plot of the carrier density as a function of the Fermi level for hBN using Eqtns. 15,16. The range of energies where the Fermi level must lie to obtain dopant densities of [05-1]x$10^{11}cm^{-2}$ is shown as a green band and is estimated to be E_f~$[120-150]meV$ above the valence band.

References

[1] S. Datta, Quantum Transport, New York: Cambridge University Press, 2005.

[2] K. Wantanabe, T. Taniguchi and H. Kanda, "Direct bandgap properties and evidence for ultraviolet lasing of hexagonal boron nitride single crystal," *Nature Materials,* vol. 3, p. 404, 2004.

[3] J. Robertson, "Electronic stucture and core exciton of hexagonal boron nitride," *Physical Review B,* vol. 29, no. 4, p. 2131, 1984.

Appendix C. : Measurement of Control Devices

Control samples were fabricated using identical processing as the hBN devices (see main text) in gen-III. Various other oxide substrates were used in order to verify that no significant current was obtained in any oxide substrate used throughout the experiments. Figure A7a shows the results of devices fabricated on wet oxide substrates and Figure A7b shows the results of devices fabricated on dry oxide substrates. The highest current levels obtained on any substrate was ~12pA which is well below (~7orders of magnitude) the measured currents on our hBN devices. This rules out possible surface currents measured in the oxide substrates.

We also fabricated our gen-III structures on a PMMA layer which was transferred onto an oxidized silicon substrate. The PMMA layer was transferred onto the substrate by spin coating a bare Cu foil (i.e. without any hBN) and then following the procedure outline in the main text (Fig. 52b). The results of the I-V measurements on these samples are shown in Fig. S5d where no significant currents are measured. This rules out the possibility of graphitizing the PMMA residues during the anneal at 800°C in 10%O_2.

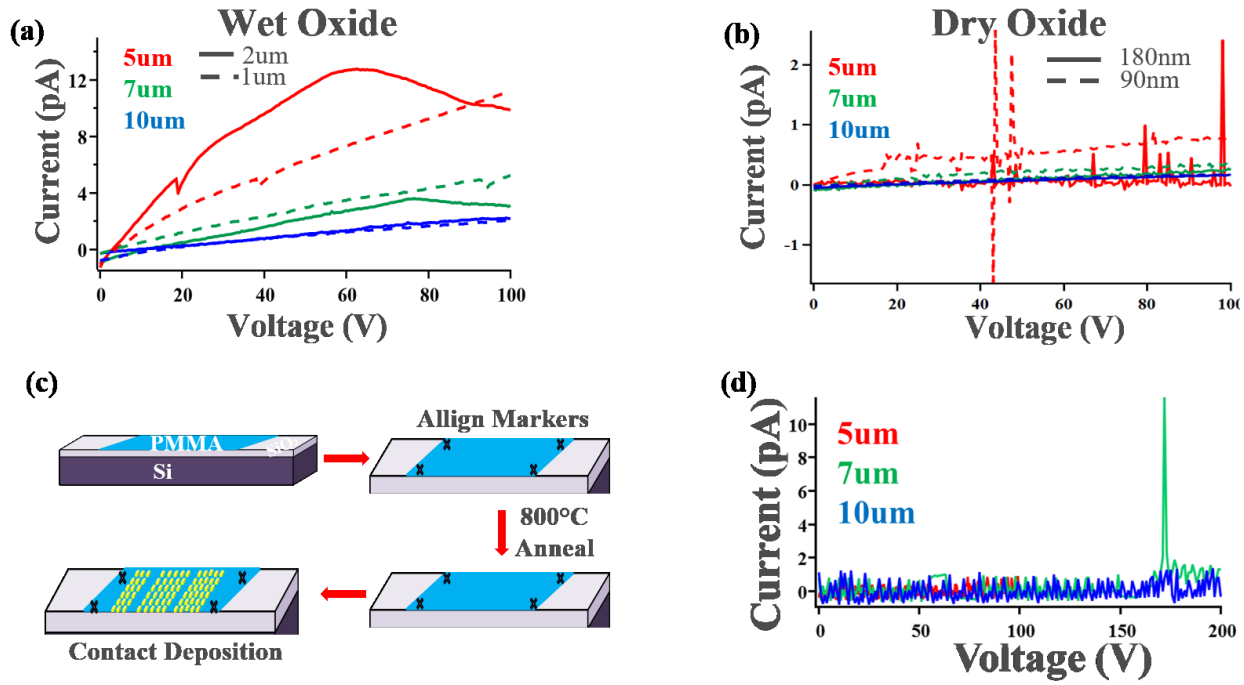

Figure A 7 :(a) I-V curves of devices fabricated on wet oxide substrates of 2um and 1um thick SiO_2. Data is shown for channel lengths of 5, 7, and 10um. (b) I-V curves of devices fabricated on dry oxide substrates of 180 and 90nm thick SiO_2. Data is shown for channel lengths of 5, 7, and 10um. (c) Fabrication steps for PMMA control device. (d) I-V curves measured on PMMA control devices for various channel lengths.